# A MODELING FRAMEWORK FOR SPATIAL TRANSMISSION OF COVID-19 IN LOCAL COMMUNITIES

A DISSERTATION IN
Mathematics
and
Physics

Presented to the Faculty of the University
of Missouri-Kansas City in partial fulfillment of
the requirements for the degree

DOCTOR OF PHILOSOPHY

by
HADEEL HASSAN ALQADI

M.S., University of Missouri-Kansas City, USA, 2014
B.S., King Abdulaziz University, Saudi Arabia, 2009

Kansas City, Missouri
2022

A MODELING FRAMEWORK FOR SPATIAL TRANSMISSION OF COVID-19 IN LOCAL COMMUNITIES

Hadeel Hassan AlQadi, Candidate for the Doctor of Philosophy Degree

University of Missouri-Kansas City, 2022

## ABSTRACT

COVID-19 is the recent infectious disease caused by the severe acute respiratory syndrome novel coronavirus (SARS-CoV-2). Because the transmissibility of the virus is relatively high and the outbreaks remained undetected for several days, COVID-19 turned into a global pandemic. Almost all countries in the world have been exposed to the virus. Just in the United States, the COVID-19 cases are over 75 million, with more than 886K deaths as of February 2022.

The pandemic duration and the enormous impacts on societies, economies, and public health have substantially affected the importance of conducting mathematical and statistical tools to analyze and predict the spatial transmission dynamics of COVID-19, which could provide invaluable benefits to global public health to reduce the chances of emerging new waves and control the epidemic. The current mathematical and statistical models have proved insufficient due to the lack of human

behavioral and social processes, which have appeared to be vital to understanding the course of the pandemic.

This dissertation proposes incorporating human behavioral, demographical, and beliefs processes to improve the accuracy of the current mathematical and statistical models. These processes include structural characteristics associated with race, ethnicity, and gender, as well as the mobility of individuals within and between local communities and beliefs about accepting or rejecting vaccinations. We focused on two modeling approaches to evaluate their capabilities and usefulness in predicting and analyzing the spatial dynamics of the disease associated with the processes mentioned earlier. The first approach is statistical modeling, implemented with SaTScan. It enabled us to identify periodic spatial-temporal COVID-19 clusters and the location of their probability of occurrences, and asses the spatial clusters with respect to demographic factors of gender, race, and ethnicity. The second approach is mathematical modeling with Ordinary Differential Equations (ODE). We developed a mathematical model to describe the spatial spread of COVID-19 within and between clusters, and investigate the global impacts of population movements from and to the local clusters on the spread of the COVID-19. Moreover, we utilized the method of Hopf bifurcation to test whether the oscillations in the COVID-19 cases are due to the natural characteristics of host-pathogen interactions.

APPROVAL PAGE

The faculty listed below, appointed by the Dean of the School of Graduate Studies, have examined a dissertation titled "A Modeling Framework for Spatial Transmission of COVID-19 in Local Communities", presented by Hadeel Hassan AlQadi, candidate for the Doctor of Philosophy degree, and certify that in their opinion it is worthy of acceptance.

Supervisory Committee

Majid Bani Yaghoub, Ph.D., Committee Chair
Department of Mathematics & Statistics

Liana Sega, Ph.D.
Department of Mathematics & Statistics

Elizabeth Stoddard, Ph.D.
Department of Physics & Astronomy

Steve Simon, Ph.D.
Department of Biomedical & Health Informatics

Wajeb Gharibi, Ph.D.
Department of Computer Science & Electrical Engineering

CONTENTS

ILLUSTRATIONS

TABLES

# ACKNOWLEDGMENTS

I am very thankful to my advisor, Dr. Majid Bani-Yaghoub, for his guidance and support throughout my doctoral research. He provided me with encouragement, valuable feedback, and the expertise I needed during my dissertation. This dissertation could not have been completed without his guidance and invaluable support. Dr. Elizabeth Stoddard, Dr. Liana Sega, Dr. Steve Simon, and Dr. Wajeb Gharibi, thank you for your time and effort in being on my Ph.D. committee. I appreciate all of your help and support. My appreciation extends to Dr. Noah Rhee for his support.

I am grateful to my lovely family for being the source of my strength during my entire academic life. I want to thank my parents, Hassan AlQadi and Jamela Matter, for their love, prayers, and continuing support throughout my life. My sincere thanks are also extended to my eldest brother, Khalid AlQadi, for his continued support and encouragement, and to my sister, Duha AlQadi, for her endless love and support. A special thanks to my husband, Ahmed Aleissa, who encouraged me to achieve my dreams and helped me during this journey. Without his love, encouragement, and support, I would not be who I am today. My deepest thanks and gratitude extend to my beautiful daughter, Wateen, for being in my life. She has been my constant source of inspiration and motivation.

I am also appreciative of my friends for their unconditional support. Finally, I am indebted to Jazan University for their scholarship and to my country, Saudi Arabia, for funding my education.

# CHAPTER 1

# INTRODUCTION

## 1.1 COVID-19 Overview

Coronaviruses are members of the Nidovirales order's Coronaviridae family. Corona refers to the crown-like spikes on the virus's outer surface (See Figure 1), thus, it was named the coronavirus [3]. The coronavirus family is divided into four subgroups: alpha, beta, gamma, and delta coronaviruses [5]. These viruses were considered to solely infect animals until 2003 when a virus caused severe acute respiratory syndrome (SARS) for individuals in Guangdong province in China. SARS-CoV was named after the virus, which was found to be a member of the Beta-coronavirus subgroup [3]. A decade later, in 2012, some individuals from Saudi Arabia were diagnosed with another coronavirus. The virus discovered was identified as a member of the Beta-coronavirus subgroup and named the Middle East Respiratory Syndrome Coronavirus (MERS-CoV) [3, 5, 10].

COVID-19 is the recent infectious disease caused by the severe acute respiratory syndrome novel coronavirus (SARS-CoV-2). Almost all countries in the world have been exposed to this virus. Since January 2020, more than 378 million individuals have become infected with COVID-19. The infection has resulted in more than 5 million deaths as of February 2022 [53]. In the United States, the COVID-19 cases are over 75 million and more than 886,000 deaths as of February 2022 [24]. In order to reduce the spread of COVID-19, businesses, communities, and governments have

implemented different control measures such as mandatory lockdowns, social distancing, avoiding crowded events, and the use of face masks in public [26]. Nevertheless, control of COVID-19 remains a significant issue in several parts of the world [65].

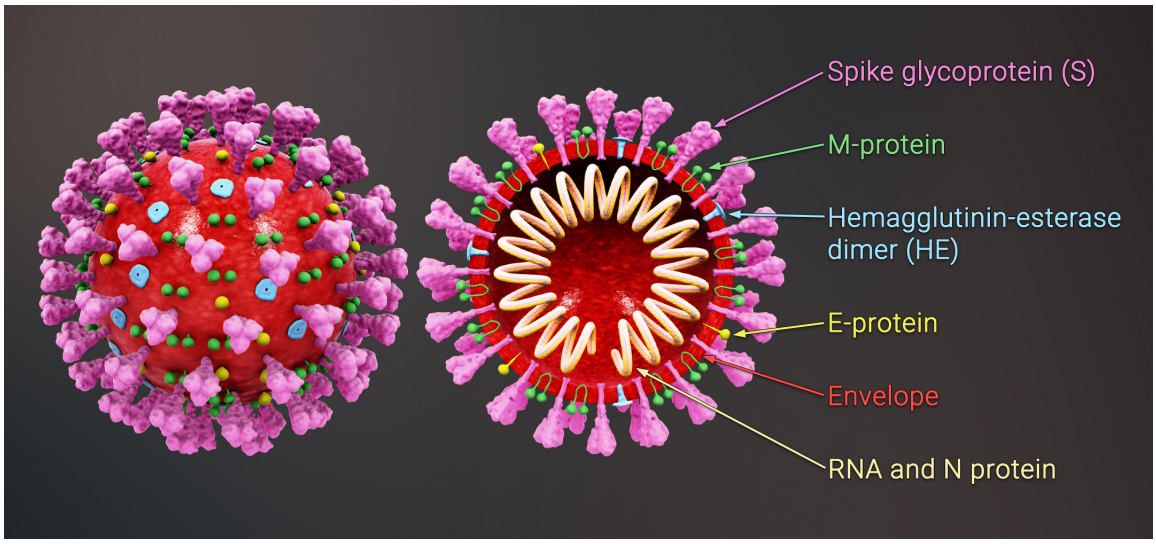


Figure 1: 3D medical animation showing the structure of a coronavirus.
Adapted from: `https://www.scientificanimations.com/wiki-images/`

## 1.2 Transmission

COVID-19 became a worldwide pandemic because the virus's transmissibility is relatively high, and outbreaks were undiscovered for several days. SARS-CoV-2 can be transmitted by direct contacts, such as droplet and human-to-human transmission, as well as indirect contacts, such as infected items, airborne contagion, and personal protective equipment (PPE) [4]. Person-to-person transmission of SARS-CoV-2 is thought to occur mainly through respiratory droplets produced when a

patient coughs, sneezes, or even speaks or sings. Droplets can only travel six feet (almost two meters) and stay in the air for a short period of time [1]. SARS-CoV-2, on the other hand, stays infectious in droplets (less than five microns in diameter) that may float in the air for up to three hours [1, 4]. As a result, airborne isolation, room ventilation, and adequate disinfectant treatment (particularly in toilets) may limit the virus's aerosol dissemination.

### 1.3 Symptoms and Infected Individual

During the early outbreak of COVID-19, the median basic reproduction number for the United States was 1.66 (IQR: 1.35–2.11), and the case fatality rate is estimated to range between 2% and 5% [2]. However, because this virus's transmissibility is relatively high and the epidemics remain undetected for several days, the exact number of infected people is unknown due to inadequate testing and inaccurate data reported in many countries [2, 6].

COVID-19 has an incubation period of 2 to 14 days, and around 44 % of cases spread before a person notices signs and symptoms [5, 87, 88]. Infected individuals have reported a wide range of moderate to severe symptoms. These symptoms are divided into three categories: the most common (fever, dry cough, and tiredness), the less common (aches and pains, conjunctivitis, sore throat, diarrhea, headache, loss of taste or smell, skin rash, nausea or vomiting, and discoloration of fingers and toes), and the severe symptoms (i.e., difficulty during breathing or shortness of breath, chest pain or pressure, and loss of speech or movement) [3, 86, 126].

Furthermore, older adults and those with various comorbidities such as cancer, cardiovascular disease, diabetes, and immunosuppressive diseases are at a higher risk

of acquiring the infection and developing difficulties [7, 8]. On the other hand, children with COVID-19 have milder symptoms and better clinical outcomes [4]. Although early studies showed that children with COVID-19 were less likely to develop severe symptoms than other age groups, one new study has shown that children are as likely to develop COVID-19 as adults [4, 9]. Therefore, prevention and finding appropriate treatment for children is as essential as adults.

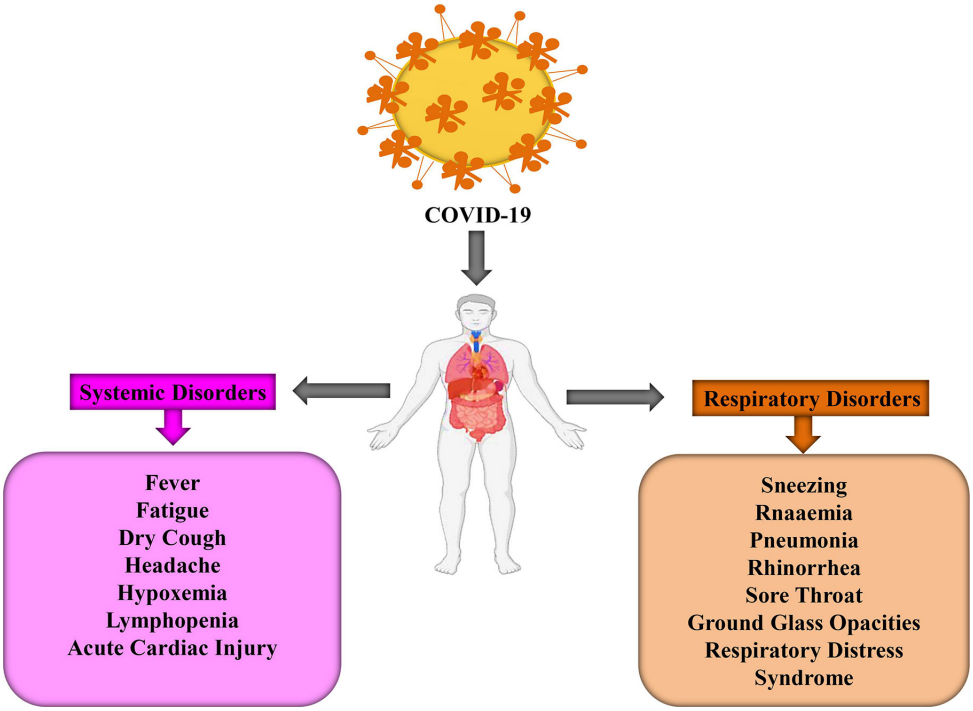


Figure 2: COVID-19 mild and severe symptoms.
Adapted from: `https://www.frontiersin.org/articles/10.3389/fphar.2020.563478/full`

## 1.4 Prevention

To combat the threat of COVID-19, the WHO and CDC has issued guidance for implementing COVID-19 prevention strategies (See Figure 3). These guidelines include staying at home (home quarantine) and avoiding direct contact with any healthy (possibly asymptomatic) or infected individual. Also, people have to avoid unnecessary travel and keep at least two meters of distance from other people, especially if they cough or sneeze. Avoid shaking hands when greeting others and wearing masks, hand washing for at least 20 seconds with soap and water or hand sanitizer with at least 60% alcohol, especially after touching common surface areas, or using public restrooms [4].

In terms of vaccines, three vaccines have been authorized by the FDA: Pfizer-BioNTech, Moderna, and Johnson and Johnson. Pfizer and Moderna are both mRNA vaccines that deliver the genetic code from SARS-CoV-2 to cells in the host's body, producing copies of spike proteins that result in an immune response that creates antibodies [91]. By contrast, Johnson and Johnson is a carrier vaccine that orders the host to make SARS CoV-2 spike proteins, resulting in antibody production to prevent future infection [91]. Overall, Pfizer is 95% effective, Moderna is 94.1% effective, and Johnson and Johnson is 72% effective in preventing COVID-19 [91].

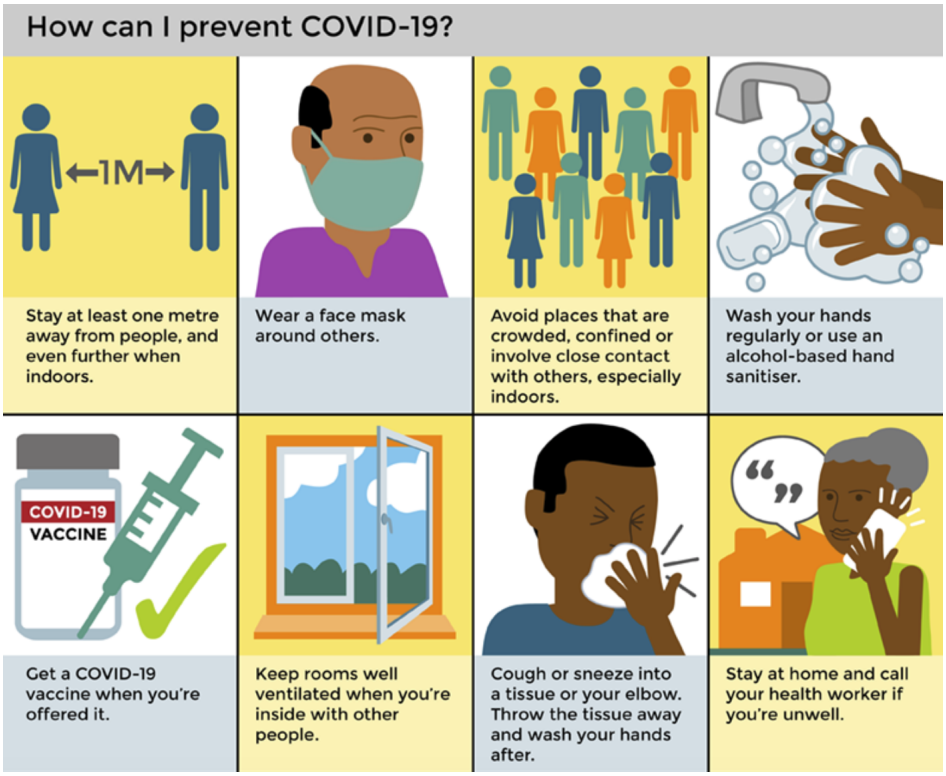


Figure 3: COVID-19 prevention strategies.
Adapted from: `https://www.avert.org/infographics`

## 1.5 Statement of the Problem

The COVID-19 pandemic revealed two crucial facts about mathematical and statistical modeling:

- Mathematical and statistical models are invaluable and essential tools in controlling the pandemic.
- Current models are less helpful than possible for coping with the current pandemic.

Current models have proved insufficient due to human behavioral, social, and demographical processes that are lacking from the models. These processes include structural characteristics associated with race, ethnicity, and gender, as well as the mobility of individuals within and between local and global communities and beliefs about accepting or rejecting vaccinations. Therefore, our goal is to include the above-mentioned factors in our modeling efforts.

In this dissertation, we explored mathematical and statistical techniques to model the spread of infectious diseases in local communities by using COVID-19 cases in Kansas City, MO, as a case study. A more detailed statistical analysis is required to identify the time series trend of COVID-19 cases and the location of occurrences. This will be accomplished utilizing of SaTScan. SaTScan can identify periodic space-time significant clusters of COVID-19 and significant spatial clusters with respect to demographic factors of gender, race and ethnicity. Using cluster analysis, we were able to identify the hotspot areas of Kansas City, MO, that are likely to be the locations of COVID-19 outbreaks.

In addition, we need to pair this analysis with mathematical models using

ordinary differential equations. We proposed the n-cluster model to study the transmission of COVID-19 within and between the spatial clusters. Also, we investigated the global impacts of population movements from and to local communities on the spread of the COVID-19. Incorporating the global dynamics of COVID-19 into the current SIR model allowed us to observe the global impacts of the infection spread in the local communities. The extended SIR model is capable of fitting well to infectious disease data by focusing on the COVID-19 data in six local communities in the United States. When the required data are not available, the mathematical modeling becomes more complex, yet we can still provide results that mimic reality. Thus, we proposed a mathematical model, SEIHR, to test the hypothesis of the presence of COVID-19 oscillations due to its intrinsic nature by applying the mathematical theory of Hopf bifurcation.

## 1.6 Flow of Chapters

**Chapter 1** includes overview of COVID-19 aspects and problem of the statement of this dissertation. **Chapter 2** contains background about the mathematical and statistical methods that we utilized in this dissertation. **Chapter 3** contains the prospective analysis of COVID-19 within Kansas City, MO, to identify periodic spatial-temporal clusters of COVID-19. **Chapter 4** contains the assessment of the retrospective analysis of COVID-19 within Kansas City, MO, to identify spatial clusters with respect to demographic factors. **Chapter 5** presents the proposed COVID-19 spatial transmission model that utilized ordinary differential equations for cluster environment. **Chapter 6** contains the proposed extended SIR model incorporates the global dynamic. In the proposed model, we apply new techniques using MATLAB

to estimate the parameters of the model where the local and global parameters are estimated in a sequential manner. **Chapter 7** presents the SEIHR model to study the periodic and oscillatory behaviors of COVID-19, analyze and validate the model mathematically. Finally, **Chapter 8** concludes the dissertation, discuss the major limitations of the work to this point and suggest some ideas and topics for future study.

# CHAPTER 2

# SPATIAL METHODS IN EPIDEMIOLOGY

## 2.1 Overview

Infectious diseases continue to pose a significant public health threat despite the tremendous progress in their prevention and control over the last three decades. Detecting and responding to outbreaks of infectious diseases is a crucial role of front-line public health organizations [11]. The primary reason for investigating an outbreak is to prevent other cases through control measures, while other motivations include addressing public or political concerns, evaluating health programs, and advancing understanding of the disease [11, 108].

One of the essential properties of infectious diseases is their spatial spread. *Spatial spread* is defined as "a feature that is mostly determined by the epidemic process, human mobility, and control measures" [14]. Therefore, using Geographical Information Systems (GIS) and spatial statistics can mitigate the epidemic through scientific information, find spatial correlations with other variables, and identify disease transmission dynamics [108, 116].

The GIS provides dynamic maps to understand the spatial distribution of diseases for analysis on the frequency of cases, disease mapping, a spatial cluster of diseases, and disease association with environmental and demographic factors. The mapping of infectious diseases for the benefit of public health using geospatial and information technologies is not a novel method of tracking diseases. The first map for

visualizing the relationship between the disease and location was done in 1694 during the Italian plague pandemic [108].

During the 1854 cholera outbreak, physician John Snow made a significant contribution to public health and epidemiology history by employing cartographic applications and spatial visualization to understand and track cholera spreading (See Figure 4). The maps were recognized after 225 years as a communication tool in identifying and monitoring infectious illnesses such as the 1918 influenza pandemic, yellow fever, and cholera [108].

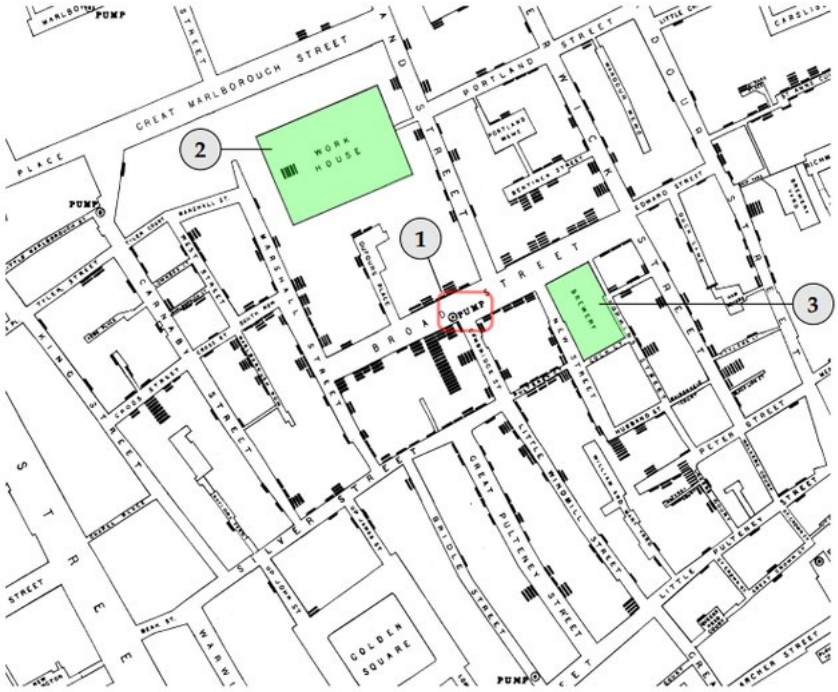


Figure 4: Dr.John Snow's map during the 1854 cholera outbreak. Each point represents a death attributed to the cholera. Adapted from: `http://www.warse.org/IJATCSE/static/pdf/file/ijatcse02842019.pdf`

In the current era, multiple outbreaks of emerging or re-emerging pandemics have abruptly swept globally in the last three decades, resulting in millions of fatalities. As a result, around two thousand studies focused on health GIS and spatial analysis literature revealed that 248 research publications out of 865 were focused on infectious disease mapping [15].

## 2.2 Spatial Methods in the Study of COVID-19

The COVID-19 pandemic spread has been extensively studied, and the methodologies and tools used to investigate the spatial and temporal variations in COVID-19 transmission have been diverse and have evolved quickly to adapt to the data available and knowledge of the disease [98]. The pandemic's duration and its impact on communities, economics, politics, and public health have significantly influenced the role of spatial analysis in understanding COVID-19 [108].

The spatial tools and techniques to understand COVID-19 have been implemented and widely used to track the spread of the disease, identify high-risk patients and hotspot areas, and have real-time communication with healthcare experts and decision-makers [16, 98]. Although studies implementing GIS methods were initially focused on visualizing or tracing contacts, such as the dashboard created by Johns Hopkins University, they later moved on to spatial analysis incorporating social, economic, environmental, and more sophisticated analytical tools as more data became available [105].

Several epidemiological and statistical methods with geographical features are required in examining epidemics. It is preferable to start with local communities for such spatial analysis tasks. The reason for focusing on the local areas for investigation

is because the epidemics generally begin in small areas and then spread globally if they are not controlled [116].

Several studies identified the spatial methods that had been used to analyze the pandemic's distribution patterns in the first and second halves of 2020 [105, 110, 116]. These methodologies were classified into six thematic groups: spatial models, including spatial clustering and mathematical models; multicriteria analysis; remote detection and uncrewed aerial vehicles; data mining and networks; web maps; and volunteered geographic information (VGI) and public participatory GIS (PPGIS) [110, 116].

This dissertation focuses on two spatial models: statistical spatial clustering and mathematical modeling.

### Spatial Clustering

Spatial clustering is the study of spatial patterns in the transmission of infectious diseases and the discovery of other disease-related factors associated with the uneven geographic distribution that may clarify the disease's dissemination mechanism [17]. The analysis of space-time patterns is a type of disease surveillance that entails early detection of epidemic clusters of active cases, monitoring infectious agent localization and isolation, and assessing the relative risks of affected areas [98].

Studying the spatial-temporal clustering of infectious diseases helps formulate strategies that dynamically update the emergence source of disease outbreaks to help epidemiologists, decision-makers, and public health departments identify spread and risk areas [12, 89].

Among the spatial clustering analysis tools that are popular and powerful

techniques to perform geographical surveillance of disease is space-time scan statistics [92, 93, 95, 100]. Space-time scan statistics can identify clusters of the hardest-hit areas and detect when and where transmission of the disease occurs. Utilizing such a tool is crucial to reducing the chances of another wave, avoiding the rise of small local outbreaks, and ultimately controlling the epidemic [89, 102]. In addition, the spatial-temporal analysis will lead to implementing more control measures and establishing testing and vaccination sites in the most affected areas.

There are two forms of the space-time scan statistic: prospective and retrospective [111]. To periodically monitor outbreaks, the prospective space-time scan statistic is used to detect active or emerging clusters of the disease, which can be used for surveillance during an ongoing epidemic [97]. The statistics can detect significant clusters that are active at the end of the study period and ignore historical clusters that may have existed prior to the most current time period of analysis with no health threat [89]. As more confirmed cases are updated, the prospective statistics track the active clusters in space and time, update relative risks (RRs) for each location affected by a disease, and detect emerging clusters.

Cluster detection and analysis are becoming more critical in the COVID-19 pandemic because they detect active and emerging clusters of COVID-19 and notify epidemiologists, decision-makers, and public health officials, which can aid in the eradication of infections from affected sites and improve intervention and prevention measures [108].

**Summary of Contributions**

Of particular interest, the City of Kansas City, the western part of the U.S. state of Missouri became one of the U.S.'s COVID-19 hot spots due to a substantial increase in the rate of positive COVID-19 test results in 2020. It also became one of 10 cities across the U.S. that received the attention of the White House coronavirus task force in 2020 [131]. Despite efforts to reduce the prevalence of infection, 125,000 confirmed cases and 1432 deaths had been reported in Kansas City as of February 2022 [99]. Despite the rise in vaccinations, cases have continued to increase, highlighting the need for a better understanding of how COVID-19 is spreading across the city.

As of 21 October 2021, the World Health Organization (WHO) database shows that out of 310,548 papers related to COVID-19, there are only 37 papers focusing on Kansas City. Most of those papers are associated with medical aspects of COVID-19 in Kansas City, MO [118, 119, 124, 125, 127]. The other papers relate to factors such as mask mandates [129, 130], vaccine aspects and patient hospitalization [129]. One of these papers involved a retrospective study on COVID-19 data examining gender and race [119]. However, the study focused on the therapeutic factors that influenced COVID-19 patients' ICU admissions with respect to gender and race. Another study analyzed data from both St.Louis and Kansas City, MO, to compare COVID-19 testing rates per diagnosed cases between races [132]. By studying COVID-19 testing data over time, this study concluded that black populations observed lower COVID-19 testing rates than white populations. Another paper focused on COVID-19 cases in relation to income level by studying specific zip codes in Kansas City, MO [134]. One main finding was that an increase in median income level was associated with a

decrease in the health risk gap.

The above-mentioned papers contribute to the existing Kansas City COVID-19 literature. However, they largely ignore how the spatial analysis can aid in identifying the patterns of the COVID-19 transmission and the discovery of other COVID-19-related factors associated with the disproportionate distribution that may assist in clarifying the disease's dissemination mechanism.

In Chapter 3, we conducted a prospective space-time scan statistic. At the zip code level, we detected emerging clusters of COVID-19 across Kansas City, MO, in four temporal periods of three months between March 2020 and February 2021. When examining these periods, we computed the evolution of the relative risk (RR) of the clusters in Kansas City, MO, and track the cluster characteristics thru time (cluster size, RR, observed, and expected cases).

In Chapter 4, we implemented a retrospective spatial analysis of COVID-19 in Kansas City, MO, at the zip code level for the period March–November 2020 with respect to demographic factors. We were able to analyze COVID-19 clusters in Kansas City with respect to gender, race, and ethnicity.

## Mathematical Models

Epidemiology deals with the study of the pattern and occurrence of diseases in space and time associated with other factors such as environmental and demographical factors [13]. The translation of epidemiology into mathematical equations to describe the spread of infectious diseases is known as mathematical modeling [37].

Mathematical modeling of infectious diseases has increasingly become an essential tool for prevention, prediction, and control of infectious diseases [37, 39, 51].

Since 1760, when Daniel Bernoulli developed the first disease model of smallpox, numerous mathematical models have been utilized to study, predict, assess, and control the transmission dynamics of infectious diseases [21, 47, 57, 61]. The substance of mathematical modeling lies in formulating a set of mathematical equations that mimic reality [54]. Mathematical models have been evolved from small sets of ordinary differential equations to sophisticated compartmental models with several equations (see [31, 36, 58] for a review). The first basic model, known as Susceptible-Infectious-Recovered (SIR) model, was proposed by Kermack and McKendrick in a series of three papers [40, 41, 42] to describe the transmission of epidemic diseases from individual to individual. The SIR model is a set of nonlinear ordinary differential equations, which is mathematically defined as follows:

$$\begin{aligned} \frac{dS}{dt}(t) &= -\beta S(t)I(t) \\ \frac{dI}{dt}(t) &= \beta S(t)I(t) - \gamma I(t) \\ \frac{dR}{dt}(t) &= \gamma I(t) \end{aligned} \tag{2.1}$$

where the derivatives $\frac{dS}{dt}$, $\frac{dI}{dt}$, and $\frac{dR}{dt}$ measure the rates of change of the quantities $S(t)$, $I(t)$, and $R(t)$. The transmission parameter $\beta$ is the average number of individuals that one infected individual will infect per time unit, assuming that all contacts that this individual makes are susceptible. Thus, a more highly infectious disease has a higher $\beta$. The parameter $\gamma$ is the recovery rate. So, $\frac{1}{\gamma}$ is the average time period of an infected individual remaining infectious. The product $\beta S(t)I(t)$ is the total infection rate which is the fraction of the population infected per unit time

at time $t$. Figure 5 represents the dynamic of the basic SIR model.

The ratio $\frac{\beta}{\gamma}$ is known as the basic reproductive number $R_0$, which is an essential index for quantifying the transmission of the disease. $R_0$ is the expected number of secondary cases in a susceptible group caused by one infected individual. If $R_0 < 1$, an infected individual creates less than one new infected individual on average throughout its infectious period, and the disease cannot spread. If $R_0 > 1$, each infected individual makes, on average, more than one new infected individual, which causes the infection to spread across the community [149].

For decades, the standard SIR model has been extended to various forms (See Figure 6 ) by adding different compartments for two reasons; the first one is to suit the biological and social aspects of the disease dynamics. For instance, SIR extend to SIR with birth inflow and death outflow. Also, it extend to SEIR model with exposed compartment (the individual during incubation period which individuals have been infected but are not yet infectious), and extend to SIRS model where the recovered population lose their immunity and return to the susceptible class. The second reason is to study the impact of intervention strategies (quarantine, hospitalized, waring mask) on the disease transmission dynamics in different communities. For instance, SIR model extends to S$S_F$EIQR model where $S_F$ represents the susceptible population who applied prevention measures but accidentally contacted the exposed group, and Q represents the quarantined population who get infected, and they isolated them self until they fully recovered [19, 20, 30, 32, 33, 34, 43, 67].

Over the last two years, the researchers developed simple and modified SIR models to study and predict the dynamics of COVID-19 in the community. For

instance, a discrete-time SIR model has been utilized to estimate the fatality and recovery rate of the Wuhan population [75]. Another SIR model has been developed to study the effects of different lockdown strategies in Italy that are adjusted to the severity of the disease [76]. Moreover, SEIR has been used to predict the impact of decision-makers measures on individual behaviors in spreading COVID-19 in China [77]. It should be mentioned that the modified SIR models need complex data for development. Due to little information and a lack of reliable data regarding the newly emerged disease, many researchers have chosen the simple SIR model [69]

However, the capability of SIR models in the case of the COVID-19 pandemic is a matter of debate, despite the simplicity and efficacy of SIR models in forecasting a variety of other infectious diseases [69]. The failure of the standard SIR models to forecast the COVID-19 pandemic can be explained for various reasons. These over-simplified models ignore the factors that significantly affect the course of the disease. For instance, these mathematical models ignore the effects of global dynamics of infection on local communities. The presence of COVID-19 can largely influence infection dynamics in a local community. Most communities are well-connected, so the assumption that the disease exists only within the community is invalid. Because of that, the SIR models are highly accurate for local and isolated communities such as boarding schools and retirement houses, but they are highly inaccurate when dealing with global pandemics like COVID-19.

Furthermore, the absence of global impacts limits the disease dynamic. Namely, the solution curves of SIR models always represent the same qualitative dynamics: an epidemic wave of the infectious population, an inverted S shape for susceptible popu-

lation, and S shape for the recovered population. Regardless of parameter values and initial conditions, such qualitative behaviors will always remain the same. Another explanation for the failure of SIR models to predict the COVID-19 epidemics is the lack of spatial transmission of infection. Previous studies showed a close relationship between spreading disease in the community and human mobility [78, 79, 80] Another reason for SIR limitation is that the recovered individuals are assumed to be immunized, which means they are no longer susceptible. This assumption differs with new findings suggesting there is a possibility of the reactivation of the virus or reinfection of previously infected individuals [69, 81]. Recent studies found that the virus antibodies in infected people only last about 50–60 days [69, 82].

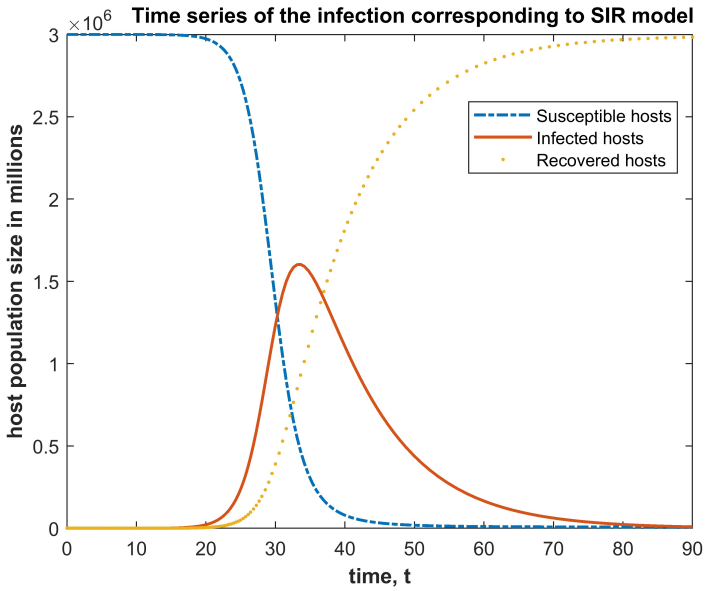


Figure 5: Dynamic of the basic SIR model. The Blue inverted S shape represents the number of susceptible individuals, the red wave represented the infected individuals, and the yellow S shape represents the recovered individuals.

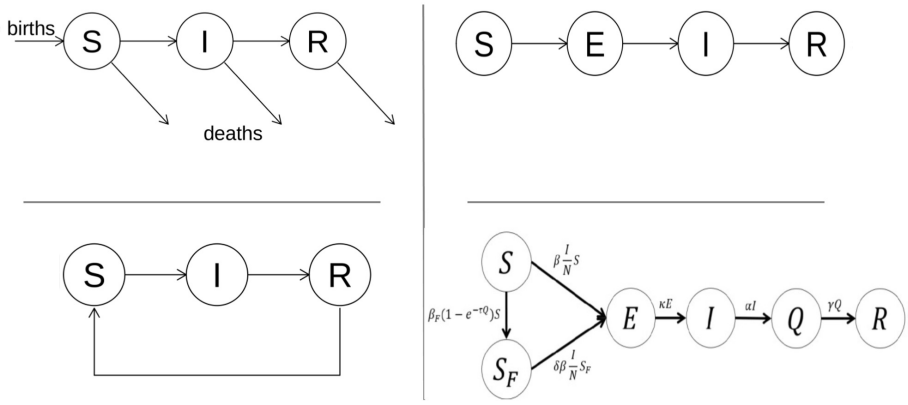


Figure 6: Extended forms of SIR model: Top models from left to right: SIR model with births and deaths, SEIR model. Bottom models from left to right: SIRS model, and S$S_F$EIQR model.

**Summary of Contributions**

In Chapter 5, we presented our approach of resolving the absence of human mobility and assuming of immunized the recovered individuals by extending the SIR model to the n-cluster model. In this model, we analyzed the model mathematically for 1 cluster, 2-cluster, and n-cluster. Also, we provided numerical simulations to study the impact of human behaviors and beliefs on the spread of the disease in the communities.

In Chapter 6, we presented our approach of resolving the absence of global impacts by extending the SIR model by adding time-varying global effects. There are three possibilities to include the estimated the global impacts on spreading the disease

in the community; susceptible individuals from a local community can travel in and out of their community without any exposure to COVID-19, they can be exposed to COVID-19 while traveling and develop symptoms after they return to their community, or they can be diagnosed with COVID-19 during their traveling and return to their community after recovery. To examine the predictive accuracy of the extended SIR model, we studied the prevalence of the COVID-19 infection in six randomly selected cities and states influenced by the COVID-19 global pandemic: Kansas City, Saint Louis, San Francisco, Missouri, Illinois, and Arizona. The extended SIR model significantly outperformed the standard SIR model and revealed oscillatory behaviors with an increasing trend of infected individuals.

In Chapter 7, we expanded the SIR model to SEIHR, which can represent the COVID-19 transmission dynamics in the community. We performed a mathematical analysis of the model by examining the local stability of the disease-free and endemic equilibriums. We also used the Next Generation Matrix (NGM) approach to calculate the basic reproduction number, $R_0$. Furthermore, we examined if the model fits the Hopf bifurcation requirements to comprehend the dynamics of the disease during the emergence of a second wave and the type of control measures required to mitigate it. We showed that the oscillations of COVID-19 can happen due to the intrinsic nature of the disease by using Hopf bifurcation and numerical simulations.

## 2.3 Description of the Study Area

The study area in dissertation is Kansas City, the western part of the U.S. state of Missouri. Kansas City lies within Jackson County, with some portions spilling into Clay, Cass, and Platte counties between latitude $39°05'59''$ N and longitude $94°34'42''$ W (See Figure 7 ). Based on the U.S. Census Bureau American Community Survey, Kansas City, MO had an estimated population of 508,090 in 2020. Approximately 51.5% of the population was female, 60.9% was White, and 23.1% of the total population was under 18 years old [138].

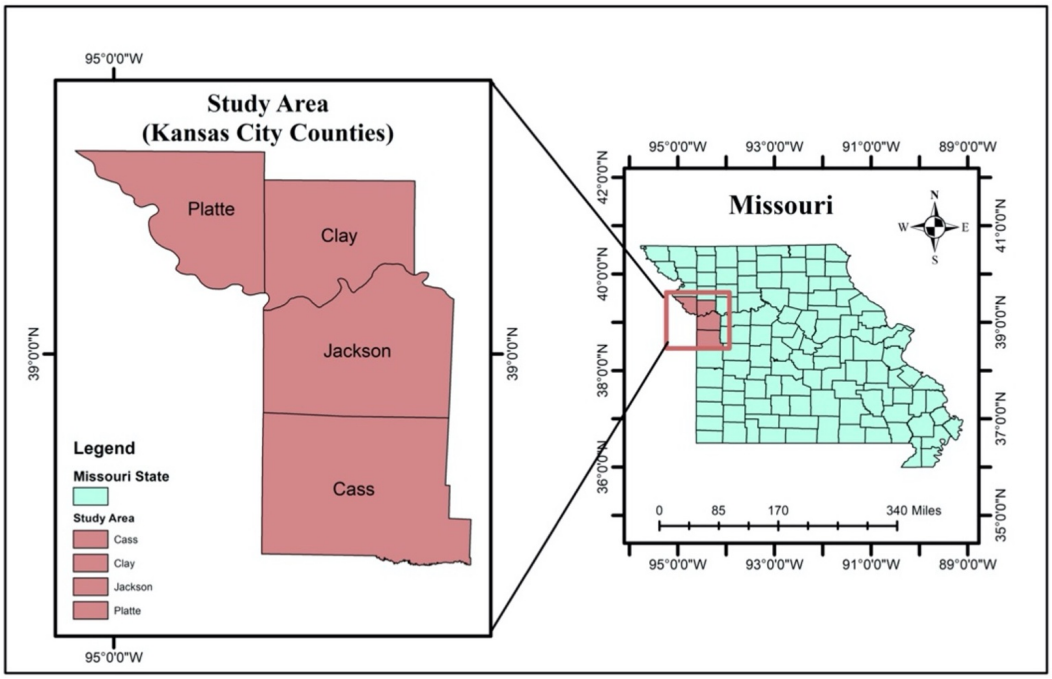


Figure 7: Missouri State map (right), Kansas City counties map (left).

# CHAPTER 3

# PROSPECTIVE SPATIAL-TEMPORAL CLUSTERS OF COVID-19

## 3.1 Overview

In this chapter, we discussed how we conducted a prospective Poisson spatial-temporal analysis of Kansas City, MO, COVID-19 data at the zip code level by utilizing SaTScan (version 9.6). The analysis focused on daily infected cases in four equal periods of three months. We detected temporal patterns of emerging and reemerging space-time clusters between March 2020 and February 2021. The spatial-temporal clusters are mainly concentrated in Kansas City's downtown and further extend the infection along the State Line Road. With the availability of updated data, the capabilities of prospective analysis allowed us to evaluate current strategies for controlling the spread of COVID-19 variants and offer a basis on which to anticipate the future development of the hardest-hit areas.

This chapter has been published in the Epidemiology and Infection Journal [84].

## 3.2 Introduction

Space-time scan statistics is one of the spatial clustering analysis methods that are popular and powerful strategies for disease surveillance [92, 93, 95, 100]. Space-time scan statistics can identify clusters of the hardest-hit areas and detect when and where transmission of COVID-19 occurs. Utilizing such a tool is crucial to reducing the chances of another wave, avoiding the rise of small local outbreaks, and

ultimately controlling the epidemic. In addition, the spatial-temporal analysis will lead to implementing more control measures and establishing testing and vaccination sites in the most affected areas [89, 102, 114]. The prospective analysis is one of space-time scan statistics that used to periodically monitor the outbreaks. The statistics can detect significant active clusters at the end of the study period and ignore historical clusters that may have existed prior to the most current time period of analysis with no health threat [92, 97]. As more confirmed cases are updated, the prospective statistics track the active clusters in space and time, update relative risks (RRs) for each location affected by a disease, and detect emerging clusters.

Consequently, significant studies on space-time scan statistics in the spread of COVID-19 have been demonstrated globally at the country level including USA [89, 102], India [107], Brazil [112], Italy [103], South Korea [115], French Alps [109], Germany [113], Sergipe [106], and locally at the city level , for example, Sao Paulo in Brazil [114], Punjab in Pakistan [101], East Java in Indonesia [104], etc.

Of particular interest, Kansas City, Missouri has become one of the major hot spots for COVID-19 in the United States due to an increase in the rate of positive COVID-19 test results. To combat the threat, Kansas City's mayor, Quinton Lucas, issued a state of emergency proclamation on March 12, 2020, which mandated masks and restricted gatherings and congregations of individuals [90]. Kansas City also encourages individuals to stay at least six feet away from others, avoid crowds and poorly ventilated spaces, maintain proper hygiene by washing hands thoroughly, and get vaccinated [90]. Regardless of the efficacy of COVID-19 vaccines, many individuals still have concerns about getting vaccinated. For instance, Missouri's vaccination

efforts currently rank $43^{rd}$ in the country, and only 54.4% of Missourians are reportedly fully vaccinated [96]. Kansas City, MO, reported that only 57.4% of its population is fully vaccinated as of February 2022 [99]. With all efforts to control the pandemic, Kansas City, MO, has observed more than 125,000 confirmed cases and 1432 deaths as of February 2022. [99].

In this chapter, our objective is to detect periodic significant space-time clusters of confirmed cases of COVID-19 at the zip code level in Kansas City, MO. The analysis focused on daily COVID-19 cases in four equal periods of three months between March 2020 and February 2021. The prospective space-time statistic is useful because it detects active and emerging significant clusters of COVID-19 during the four periods, which can be informative for decision-makers to track cluster characteristics through time (cluster size, RR, observed, and expected cases). As more data become available, spatial clustering can be used as a COVID-19 surveillance tool.

## 3.3 Material and Method

### COVID-19 Data

We collaborated with the Kansas City (KCMO) Health Department to obtain the necessary data for the study. KCMO Health Department provided the daily confirmed cases of COVID-19 between March 2020 and February 2021. The data contains the following variables: date of case receipt, Epidemiological (Epi) week, Epi year, EpiTrax CMR# [135], age, gender, race, zip code, specimen collection date, vital status, and outbreak associated.

For the spatial- temporal prospective study, we need three data files; the first file is the case data which contains the zip code, the cases in each zip code, and the

time of each case. The second data file is the population data which contains the background of the population (zip code, and population in each zip code), and the last data file is the coordinated data that contains the latitude and the longitude for each zip code [139].

Table 1 provides the basic descriptive statistics of Kansas City, MO, weekly COVID-19 data from March 2020 to February 2021.

Table 1: Descriptive statistics of Kansas City, MO weekly COVID-19 data from March 2020 to February 2021.

| Statistic measure | # of affected zip codes | Confirmed cases | Mortality |
|---|---|---|---|
| Minimum | 10 (0, 3, 7) | 13 (0, 6, 7) | 0 (0, 0, 0) |
| Maximum | 45 (5, 10, 31) | 1899 (216, 617, 1021) | 24 (10, 10, 17) |
| Mean | 36.9 (3.8, 8.2, 25.0) | 712.9 (71.3, 201.4, 415.2) | 9.1 (1.2, 2.3, 5.3) |
| Median | 39 (4, 8, 26.5) | 616 (59, 136.5, 383) | 6 (0, 1, 3.5) |
| St.Dev | 7.1 (1.0, 1.5, 5.1) | 555.9 (65.6, 184.7, 294.6) | 7.4 (1.9, 2.6, 5.0) |
| Range | 35 (5, 7, 24) | 1886 (216, 611, 1014) | 24 (10, 10, 17) |

* The numbers inside the parentheses correspond to Platte, Clay, and Jackson counties, respectively. Of 48 zip codes in Kansas City, MO, there are 5, 11 and 32 zip codes in Platte, Clay, and Jackson counties, respectively.

### Prospective Space-Time Method

To detect active or emerging space-time clusters, we utilized the prospective space-time scan statistic of the discrete Poisson model implemented in SaTScan soft-

ware developed by Kulldorf and his colleagues [94]. Namely, we detected space-time COVID-19 clusters in Kansas City that were active and emerging at the end of the study period and ignored the non-statistically significant clusters that may have existed previously but are no longer a public health threat. We utilized the Poisson model because we were interested in the geographical distribution of COVID-19 cases in Kansas City between March 2020 and February 2021, adjusting for the population at risk. The prospective statistic used a cylinder window with a space base and height corresponding to the time. The center of the cylinder was defined as the centroid of each zip code in Kansas City, MO. The cylinder window is moved in two dimensions: space and time. Hence, we obtained an infinite number of overlapping circles covering the entire study region, and each circle reflected a possible cluster of COVID-19 in the Kansas City area. The circle's radius varies continuously from zero to a specified maximum size. The maximum size specified the percentage of the maximum total population at risk within the scanning window. To avoid extremely large clusters, we set the upper maximum spatial scanning window size to 10% of the population at risk and the upper maximum temporal bound scanning window size to 50% of the study period. Each cylinder was expanded until the maximum spatial or temporal upper bound is reached. A likelihood ratio test was used to identify the space-time clusters of COVID-19 cases [92]. The likelihood ratio is defined as follows:

$$\frac{L(c)}{L_0} = \frac{(\frac{n_c}{\mu(c)})^{n_c}(\frac{N-n_c}{N-\mu(c)})^{N-n_c}}{(\frac{N}{\mu(t)})^{N}} \tag{3.1}$$

The likelihood ratio was calculated based on the observed and expected number of cases inside and outside that circle, where $L(c)$ is the maximum likelihood function for

cylinder C, $L_0$ is the likelihood function under the null hypothesis, $n_c$ is the number of COVID-19 cases in a cylinder, $\mu(c)$ is the number of expected cases in cylinder c, $N$ is the total number of all observed cases in Kansas City over time, and $\mu(t)$ is the total number of expected cases in Kansas City over time. The likelihood was calculated for each cylinder to determine whether the observed number of cases exceeded the expected number of cases (i.e., the likelihood ratio is greater than 1). The window with the maximum likelihood ratio statistic constitutes the likeliest cluster (primary cluster). Secondary clusters were also reported if they are statistically significant at the p-value $< \alpha = .05$. The p-values for space-time clusters were estimated using Monte Carlo simulations by repeating $n = 999$ random iterations of the dataset to test the significance.

## 3.4 Results

### Time Series of COVID-19 Cases

We used the time series of COVID-19 cases between March 2020 and February 2021. A total of 1,256 cases were eliminated from the data. These cases consisted of 1,215 cases from zip codes that did not belong to Kansas City, MO, and 41 cases that were labeled "unknown" in the data (for more details, such as the population of each county based on the zip codes, see Table A2, Table A3, and Table A4 in Appendix A). Figure 8a shows the weekly COVID-19 new cases and mortalities in Kansas City, MO. The total number of cases between March 2020 and February 2021 was 35,647, where 648 cases occurred before reopening (May 5, 2020), and the rest (17,273) after reopening. After the new COVID-19 restrictions, new weekly cases were stable at first before decreasing continuously. The time series of the cases (shown with a red

curve) had multiple M-shaped (double-top) curves. There was a small "double top" from the $12^{th}$ week to the $20^{th}$ week with the maximum values in $15^{th}$ and $18^{th}$ week, and the minimum in $16^{th}$ week. There were also several "double tops" with larger magnitudes. One from the $27^{th}$ week to the $37^{th}$ week, another from the $37^{th}$ week to the $43^{rd}$ week, a third from the $43^{rd}$ week to the $48^{th}$ week, and a fourth from the $48^{th}$ week to the $55^{th}$ week. Figure 8b shows the weekly cases per thousand for Clay County, Platte County, and Jackson County. Before the $16^{th}$ week, all counties had similar trends of cases per thousand, but Jackson County had more cases per thousand than Clay County and Platte County. Between the $22^{nd}$ and $37^{th}$ weeks, Jackson County had more cases per thousand. Between the $39^{th}$ and $40^{th}$ weeks, Platte County had more cases per thousand. From the $41^{st}$ week to the $47^{th}$ week, all counties had the same trend of cases per thousand, but Platte County had fewer cases per thousand than Clay County and Jackson County. From the $47^{th}$ week to the $49^{th}$ week and from the $51^{st}$ week to the $54^{th}$ week, Clay County had more cases per thousand. After the $54^{th}$ week, cases per thousand of all counties decreased continuously.

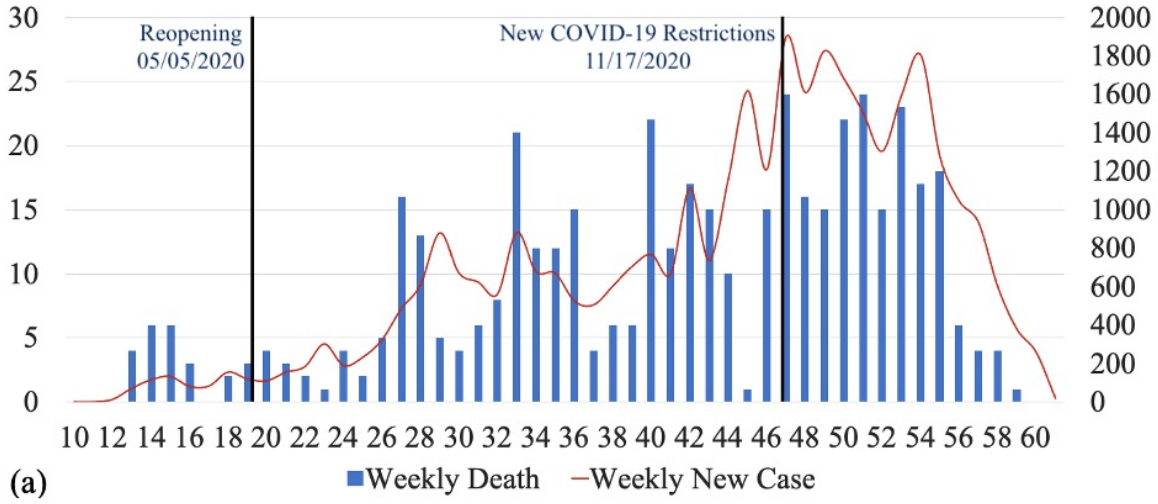


(a) Number of new weekly cases and mortality

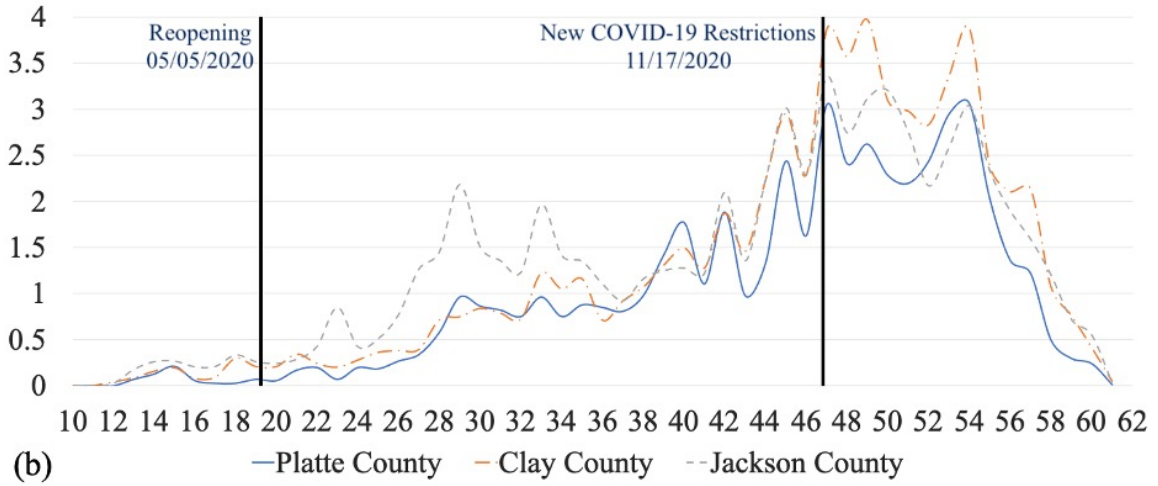


(b) Number of new weekly cases per thousand by county

Figure 8: Time series of COVID-19 cases in Kansas City, MO, between March 2020 and February 2021

**Space-time Clusters of COVID-19 During the Four Periods**

Figure 9(a) and Table 2 present the characteristics of the three statistically significant emerging space-time clusters of COVID-19 in Kansas City at the zip code level from March to May 2020. During period 1, three statistically significant clusters emerged, which were mainly concentrated in downtown Kansas City, MO. Cluster 1 was located in northeast Kansas City and includes seven locations in Jackson County, with an RR of 9.21 (expected cases = 37.24; observed cases = 274).Cluster 2 contained two locations in Clay County, where the RR was 5.16, and there were 93 observed cases. Cluster 3 contained locations in downtown Kansas City, MO, with three locations in Jackson County, where the RR was 2.25, and there were 42 observed cases.

Figure 9(b) and Table 3 show the characteristics of the seven statistically significant emerging space-time clusters of COVID-19 in Kansas City at the zip code level from March to August 2020. By adding updated data of COVID-19 in Kansas City, four more clusters have emerged. The likeliest cluster (primary cluster) contained eight locations in Jackson County with RR = 5.09. Cluster 2 was located in downtown Kansas City, MO, with six locations in Jackson County and RR = 3.33. Cluster 3 was found in south Kansas City and includes six locations in Jackson County with RR = 3.24. Cluster 4 contained nine locations in Clay County and two locations in Platte County with RR = 2.76. Cluster 5 contained eight locations in Jackson County with RR = 1.71. Clusters 6 and 7 contained only one location, each with RR = 1.99 and 1.50 in Platte County and Clay County, respectively. We noticed the clusters were spreading over a wider region in downtown and north of

Kansas City. Also, cluster 2 in period 1 disappeared during period 2.

Table 2: Emerging space-time clusters of COVID-19 March–May 2020 (Period 1) at the zip code level.

| Cluster | Duration | RR | Observed | Expected | Counties | #of locations | P-value |
|---|---|---|---|---|---|---|---|
| Cluster 1(Primary) | May | 9.21 | 274 | 37 | Jackson County | 7 | $1 \times 10^{-17}$ |
| Cluster 2 | May | 5.16 | 93 | 19 | Clay County | 2 | $1 \times 10^{-17}$ |
| Cluster 3 | May | 2.25 | 42 | 19 | Jackson County | 3 | $2.4 \times 10^{-4}$ |

Table 3: Emerging space time clusters of COVID-19 March–August 2020 (Period 2) at the zip code level.

| Cluster | Duration | RR | Observed | Expected | Counties | #of locations | P-value |
|---|---|---|---|---|---|---|---|
| Cluster 1 (Primary) | June-Aug | 5.09 | 1717 | 404 | Jackson County | 8 | $1 \times 10^{-17}$ |
| Cluster 2 | July-Aug | 3.33 | 802 | 258 | Jackson County | 6 | $1 \times 10^{-17}$ |
| Cluster 3 | July-Aug | 3.24 | 825 | 274 | Jackson County | 6 | $1 \times 10^{-17}$ |
| Cluster 4 | July-Aug | 2.76 | 694 | 265 | Clay County<br>Platte County | 11 | $1 \times 10^{-17}$ |
| Cluster 5 | July-Aug | 1.71 | 367 | 218 | Jackson County | 8 | $1 \times 10^{-17}$ |
| Cluster 6 | July-Aug | 1.99 | 214 | 109 | Platte County | 1 | $1 \times 10^{-17}$ |
| Cluster 7 | Aug | 1.50 | 135 | 91 | Clay County | 1 | $1.4 \times 10^{-3}$ |

Figure 9(c) and Table 4 show the characteristics and spatial patterns of the third period at the zip code level from March to November 2020. During this period,

there were nine statistically significant emerging space-time clusters of COVID-19 that covered large areas of north and downtown Kansas City. All clusters during period 2 were still active in period 3. Note that cluster 2, which disappeared during period 2, reappeared during period 3 as cluster 5. Also, cluster 4 during period 2 became the primary cluster during period 3. The likeliest cluster (primary cluster) contained nine locations in Clay County and two locations in Platte County with RR = 3.17. Cluster 2 was located in downtown Kansas City, MO, with eight locations in Jackson County and RR = 2.67. Cluster 3 was found in south Kansas City and contained six locations in Jackson County with RR= 2.13. Cluster 4 contained three locations in Jackson with RR = 2.07. Cluster 5 contained four locations in Clay County with RR = 1.51. Cluster 6 and 9 in Jackson County contained one location each with RR = 3.88 and 2.16, respectively. Clusters 7 and 8 contained one location each, with RR = 1.58 and 1.49 in Platte County and Clay County, respectively.

Figure 9(d) and Table 5 show the locations and spatial patterns of 10 emerging space-time clusters of COVID-19 in Kansas City, MO, between March 2020 and February 2021. During period 4, all clusters in period 3 were still active. Ten clusters were present, and most of the active clusters were along the State Line Road. The primary cluster contained nine locations in Clay County and two locations in Platte County with RR = 3.18. Cluster 2 was located in downtown Kansas City, MO, with eight locations in Jackson County and RR = 2.19. Cluster 3 was a new cluster that emerged in this period, containing three locations with RR = 1.95 in Jackson County. Cluster 4 contained four locations in Clay County and one location in Jackson County with RR = 2.23. Cluster 5 contained four locations in Jackson County with RR =

1.93. Cluster 6 contained five locations in Jackson County and one location in Cass County with RR = 1.87. Clusters 7,8 and 9 contained one location each, with RR = 2.34, 4.83, and 1.51 in Platte County, Jackson County, and Clay County, respectively. Cluster 10 contained three locations in Jackson County, with RR = 1.22.

Table 4: Emerging space time clusters of COVID-19 March–November 2020 (Period 3) at the zip code level

| Cluster | Duration | RR | Observed | Expected | Counties | #of locations | P-value |
|---|---|---|---|---|---|---|---|
| Cluster 1 (Primary) | Aug-Nov | 3.17 | 2135 | 735 | Clay County<br>Platte County | 11 | $1 \times 10^{-17}$ |
| Cluster 2 | Aug-Nov | 2.67 | 1808 | 725 | Jackson County | 8 | $1 \times 10^{-17}$ |
| Cluster 3 | Aug-Nov | 2.13 | 1541 | 759 | Jackson County | 6 | $1 \times 10^{-17}$ |
| Cluster 4 | Aug-Nov | 2.07 | 1098 | 549 | Jackson County | 3 | $1 \times 10^{-17}$ |
| Cluster 5 | Aug-Nov | 1.51 | 1053 | 712 | Clay County | 4 | $1 \times 10^{-17}$ |
| Cluster 6 | Aug-Nov | 3.88 | 85 | 22 | Jackson County | 1 | $1 \times 10^{-17}$ |
| Cluster 7 | Aug-Nov | 1.58 | 472 | 301 | Platte County | 1 | $1.3 \times 10^{-15}$ |
| Cluster 8 | Oct-Nov | 1.49 | 371 | 251 | Clay County | 1 | $3.4 \times 10^{-9}$ |
| Cluster 9 | Aug-Nov | 2.16 | 58 | 27 | Jackson County | 1 | $1.4 \times 10^{-4}$ |

Table 5: Emerging space time clusters of COVID-19 March–February 2021 (Period 4) at the zip code level

| Cluster | Duration | RR | Observed | Expected | Counties | #of locations | P-value |
|---|---|---|---|---|---|---|---|
| Cluster 1 (Primary) | Sept 20- Feb 21 | 3.18 | 4258 | 1476 | Clay County<br>Platte County | 11 | $1 \times 10^{-17}$ |
| Cluster 2 | Sept 20-Feb 21 | 2.19 | 3020 | 1454 | Jackson County | 8 | $1 \times 10^{-17}$ |
| Cluster 3 | Oct 20-Feb 21 | 1.95 | 2295 | 1221 | Jackson County | 3 | $1 \times 10^{-17}$ |
| Cluster 4 | Dec 20-Feb 21 | 2.23 | 1551 | 715 | Clay County<br>Jackson County | 5 | $1 \times 10^{-17}$ |
| Cluster 5 | Oct 20-Feb 21 | 1.93 | 2160 | 1156 | Jackson County | 4 | $1 \times 10^{-17}$ |
| Cluster 6 | Oct 20-Feb 21 | 1.87 | 1541 | 845 | Cass County<br>Jackson County | 6 | $1 \times 10^{-17}$ |
| Cluster 7 | Dec 20-Feb 21 | 2.34 | 694 | 301 | Platte County | 1 | $1 \times 10^{-17}$ |
| Cluster 8 | Oct 20-Feb 21 | 4.83 | 177 | 37 | Jackson County | 1 | $1 \times 10^{-17}$ |
| Cluster 9 | Dec 20-Feb 21 | 1.51 | 748 | 501 | Clay County | 1 | $1 \times 10^{-17}$ |
| Cluster 10 | Dec 20-Feb 21 | 1.22 | 929 | 763 | Jackson County | 3 | $1.9 \times 10^{-6}$ |

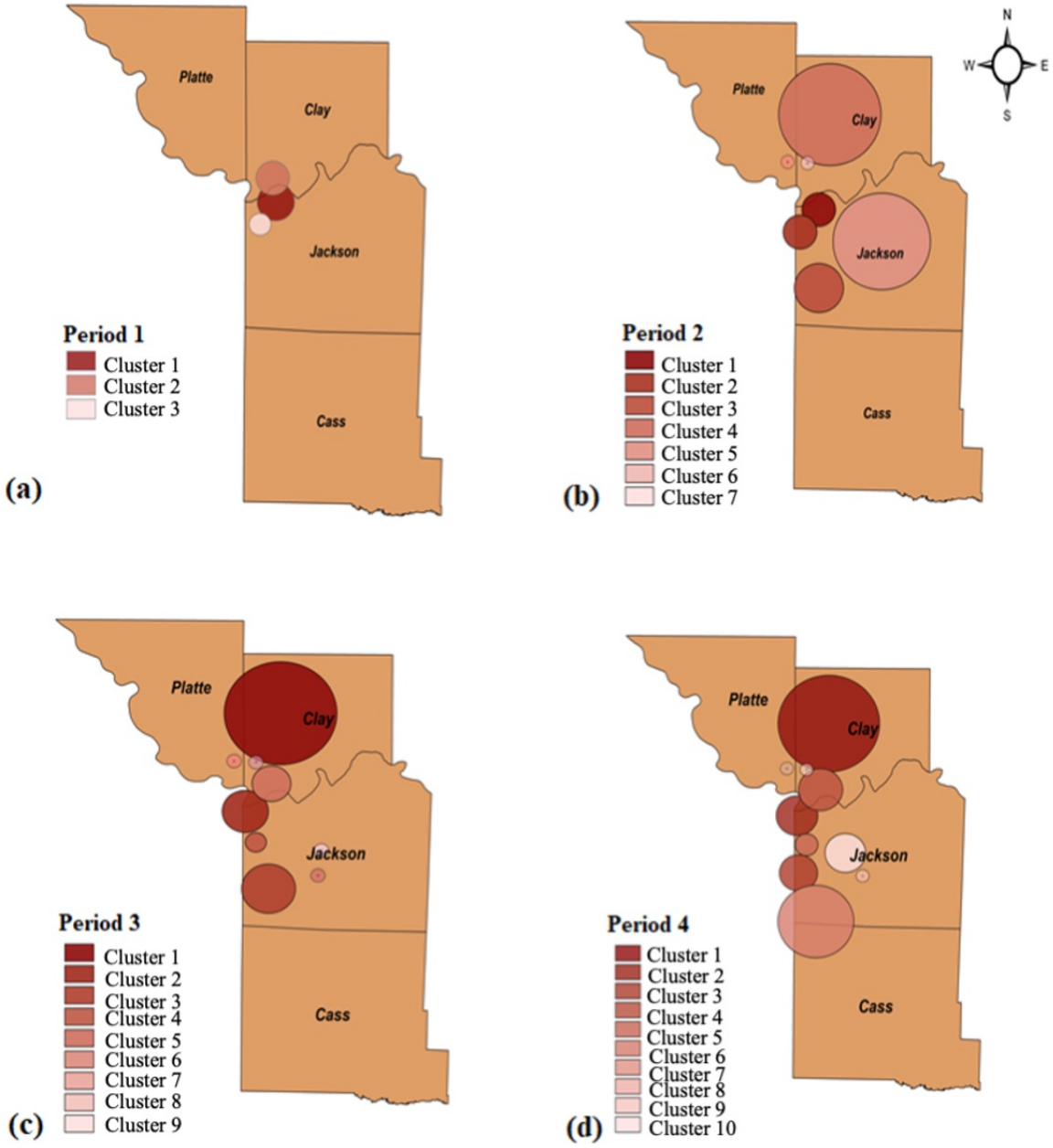


Figure 9: The emergence of COVID-19 clusters in Kansas City during four periods of three months: (a) Period 1: March–May 2020, downtown Kansas City, MO; (b) Period 2: March–August 2020, additional clusters in the north and south; (c) Period 3: March–November 2020, further spread of clusters; and (d) Period 4: March, 2020–February 2021, active clusters along the State Line Road.

## 3.5 Discussion and Conclusions

The main point of the prospective approach is the ability to add updated data to identify other emerging clusters and track the risk of previously detected clusters. In this chapter, we utilized a prospective space-time analysis to detect emerging clusters of COVID-19 in Kansas City, MO, at the zip code level, which provided results at four distinct periods: March-May 2020; March–August 2020; March–November 2020; and March 2020–February 2021. By identifying the statistically significant emerging space-time clusters, we could determine regions with increased risk of occurrence. Also, we could measure growth or decay of clusters. The results of this study were shared with the KCMO Health Department to track outbreaks and take necessary steps in the regions with higher risk of COVID-19 infection.

Rapid detection of clusters can help determine whether current preventive and control policies are effective. The prospective strategy used in this study has helped the KCMO Health Department quickly identify hot spots and allocate more resources to those regions to prevent similar outbreaks in the same regions. These measures may include adding more COVID-19 vaccination clinics or COVID-19 testing sites in high-risk areas to help control the severity and spread of the disease. Encouraging social distancing or enforcing mask mandates in these counties/regions could also prevent the spread of COVID-19. Informing public health decision-makers with surveillance data can help them better address the needs of underserved areas and promote a safer, healthier community.

Prospective space-time analysis detected three statistically significant clusters that emerged during March-May 2020, which were mainly concentrated in downtown

Kansas City. By adding updated data of COVID-19 in Kansas City from March-August 2020, the emerged clusters increased to seven clusters that were spreading across a broader region in downtown and north of Kansas City. The result of adding more data was nine clusters covering large areas of north and downtown Kansas City, and ten clusters were present and further extended the infection along the State Line Road during the two distinct periods: March–November 2020, and March 2020–February 2021, respectively.

We also observed temporal variations in the number of COVID-19 cases between March 2020 and February 2021. The times series of the cases had multiple M-shaped (double-top) curves. Compared to the weekly cases per thousand for Clay County and Platte County, Jackson County had the most significant cases per thousand for the first 34 weeks. However, after the 37th week, the COVID-19 cases turned, and Clay County took the lead.

Despite the strength of completing a prospective study in Kansas City, MO some limitations exist. First, to understand why the pandemic has severely impacted specific locations, it is essential to adjust the study for relevant factors such as demographic factors, socioeconomic status, medical conditions, and healthcare access. These factors may impact the spread of COVID-19 across regions. For instance, Figure 9 (d) shows most of the hot spots of COVID-19 during March 2020- February 2021 occurred near the State Line Road, and Table 6 shows how the emerged cluster characteristics (cluster size and RR) changed over time, starting with three clusters and ending with 10 clusters at the end of February 2021. For instance, the primary cluster during period 1 and RR = 9.21 shrank during period 2 with RR = 5.09, and

then, it grew in its size as cluster 2 during periods 3 and 4 with RR = 2.67 and 2.19, respectively. Also, cluster 2 with RR = 5.16 during period 1 disappeared in period 2 and reappeared with growing magnitude as cluster 5 in period 3 and cluster 4 in period 4 with RR = 1.51 and 2.23, respectively. In addition, cluster 4 during period 2 with RR = 2.76 became the primary cluster during periods 3 and 4 with RR = 3.17 and 3.18, respectively. Lastly, cluster 5 during period 2, with RR = 1.71, was split into clusters 6 and 9 during period 3, with RR = 3.88 and 2.16, respectively. Therefore, it is crucial to study the factors that impact the spread of COVID-19 in the affected areas.

Second, our surveillance focused on the pandemic before vaccine distribution, so trends and emerging clusters may change over time with updated current data. Therefore, completing the space-time analysis over an extended period would provide a more reliable tool for surveillance. Third, our data includes only confirmed COVID-19 cases obtained from the KCMO Health Department, so we could not gather any information on unconfirmed or probable cases. Also, we could not gather any information related to Kansas state COVID-19 data. As a result, a complete perspective on the impact of COVID-19 in Kansas City, MO, is still unattainable.

Table 6: Tracking the number of emerging clusters during the four periods of March-May 2020, with 3 active clusters, March-August 2020 increased to 7 clusters, March-November 2020 with 9 active clusters and the last period March,2020-February 2021 reaching to 10 active clusters. The relative risk (RR) and radius indicate the magnitude of each cluster

| Period 1 | | | Period 2 | | | Period 3 | | | Period 4 | | |
|---|---|---|---|---|---|---|---|---|---|---|---|
| Cluster# | RR | Radius (KM) | Cluster# | RR | Radius (KM) | Cluster# | RR | Radius (KM) | Cluster# | RR | Radius (KM) |
| 1 | 9.2 | 14 | 1 | 5.1 | 13.3 | 2 | 2.7 | 16.6 | 2 | 2.2 | 16.6 |
| 2 | 5.2 | 12.6 | Dissapeared | - | 0 | 5 | 1.5 | 13.9 | 4 | 2.2 | 17.5 |
| 3 | 2.3 | 8.1 | 2 | 3.3 | 13.3 | 4 | 2.1 | 7.5 | 5 | 1.9 | 9.1 |
| - | - | - | 3 | 3.2 | 19.3 | 3 | 2.1 | 19.3 | 6 | 1.9 | 30.2 |
| - | - | - | 4 | 2.8 | 17 | 1 | 3.2 | 40.2 | 1 | 3.2 | 40.2 |
| - | - | - | 5 | 1.7 | 38.3 | 6<br><br><br>9 | 3.9<br><br><br>2.2 | 10.1<br><br><br>10.1 | 8<br><br><br>10 | 4.8<br><br><br>1.2 | 10.1<br><br><br>16.1 |
| - | - | - | 6 | 2 | 15.2 | 7 | 1.6 | 15.2 | 7 | 2.3 | 15.6 |
| - | - | - | 7 | 1.5 | 15.2 | 8 | 1.5 | 15.2 | 9 | 1.5 | 15.2 |
| - | - | - | - | - | - | - | - | - | 3 | 1.9 | 15.2 |

# CHAPTER 4

# ASSESSMENT OF RETROSPECTIVE SPATIAL CLUSTERS OF COVID-19 WITH RESPECT TO DEMOGRAPHIC FACTORS

## 4.1 Overview

In this chapter, we discussed how geographical distribution of the COVID-19 cases associated with demographic factors. We utilized the daily data of COVID-19 cases in Kansas City, Missouri, to observe differences in the COVID-19 clusters with respect to gender, race, and ethnicity. Specifically, we conducted a retrospective Poisson spatial scan statistic with respect to demographic factors to detect daily clusters of COVID-19 in Kansas City at the zip code level from March 2020 to November 2020 by utilizing SaTScan (version 9.6). We detected that certain racial and ethnic minority groups may have been disproportionately impacted by the spread of COVID-19.

The spatial demographic cluster analysis analysis can provide guidance for reducing the social inequalities associated with the COVID-19 pandemic and enable researchers to gain a deeper understanding of disparities in the healthcare system. The results of this study illustrate that certain demographics within Kansas City, MO, are more vulnerable to COVID-19 in terms of spreading the disease and in the resulting health outcomes after illness.

This chapter has been published in the International Journal of Environmental Research and Public Health [83].

## 4.2 Introduction

As COVID-19 spread throughout communities across the United States, it became clear that inequities would arise among different demographics. Several studies suggested that certain racial and ethnic minority groups may have been disproportionately impacted by the spread of COVID-19 [136, 140]. For instance, the African American population comprises 13% of the total U.S. population [138], while according to CDC COVID-19 data, they made up 30% of all COVID-19 positive cases in the U.S. as of April 15, 2020 [121]. In addition, hospitalization rates due to COVID-19 have a disproportionately higher prevalence among the African American population than among any other race [122].

In addition, Hispanics are currently the largest ethnic minority in the U.S., with a population of nearly 60 million people [122]. While Hispanics account for 18% of the total U.S. population, they constitute nearly 28.4% of the total COVID-19 cases nationally [122]. Nevertheless, the proportions vary strongly in different parts of the country. For instance, a statewide study investigating racial disparities followed 3481 COVID-19 cases in Louisiana and found that non-Hispanic African American individuals represented 77% of hospitalizations and 71% of deaths, despite only making up 31% of the total source population [136, 140]. In New York City, COVID-19 mortality rates were 220 and 236 per 100,000 for African American and Latinx patients, respectively, whereas White and Asian Americans had mortalities of 110 and 102 per 100,000, respectively [140].

Like other U.S. cities, social distancing measures were applied throughout Kansas City, MO. Kansas City, MO became one of the U.S.'s COVID-19 hot spots

due to a substantial increase in the rate of positive COVID-19 test results in 2020. It also became one of 10 cities across the U.S. that received the attention of the White House coronavirus task force in 2020 [131]. Despite the rise in vaccinations, cases have continued to increase in Kansas City across the State Line Road as we observed in Chapter 3. To understand why COVID-19 has severely impacted specific locations, it is essential to adjust the study for relevant factors such as demographic factors for a better understanding of how COVID-19 is spreading across the city. It is crucial to establish spatial monitoring during an evolving pandemic that adjusted with demographical factors.

Spatial cluster analysis has been used in a wide variety of epidemiological studies to evaluate spatial patterns of infections [123, 128, 141]. Some examples include identifying birth defects in New York State [137] and studying spatial patterns of malaria and detecting spatial clusters of tuberculosis in China [120, 123]. In fact, spatial clusters can be more valuable in identifying regions with an increased risk of COVID-19 in certain racial and ethnic minority groups if we consider the demographic factors.

Hence, the main purpose of this chapter is providing an unbiased spatial and temporal analysis of COVID-19 data with respect to demographic factors in Kansas City, MO. Using the COVID-19 data, we analyzed the progression of COVID-19 infection in Kansas City with respect to gender, race, and ethnicity. This study implements a retrospective spatial analysis of COVID-19 in Kansas City, MO, at the zip code level for the period March–November 2020.

## 4.3 Material and Method

### COVID-19 Data

KCMO Health Department provided the same daily confirmed cases of COVID-19 as the previous dataset of Chapter 3. However, the data for this study is between March and November 2020. The same as the spatial temporal prospective analysis, the spatial retrospective analysis with respect to demographic factors needs three data files; The case data file, which contains all the zip codes in Kansas City, divides these zip codes by gender, race, and ethnicity, and the cases in each zip code with respect to gender, race and ethnicity; the population data that contained the background of each demographic factor ; and coordinate data that contained latitude and longitude for each zip code. Table 7 summarize the statistics of the number of COVID-positive cases and mortality rates in Kansas City from March to November 2020.

Table 7: Summary statistics of the number of COVID-positive cases and mortality rates in Kansas City from March to November 2020.

| Statistic measure | Minimum | Maximum | Mean | Median | STD | Range |
|---|---|---|---|---|---|---|
| Cases | 13 | 1618 | 504.29 | 524 | 375.74 | 1605 |
| Deaths | 0 | 22 | 7.14 | 5 | 6.06 | 22 |

### Retrospective Spatial Method

We aimed to detect significant spatial COVID-19 clusters at the zip code level in Kansas City with respect to demographics (i.e., gender, race, and ethnicity). The analysis would help us understand how the geographical distribution of COVID-19 cases associated with demographic factors.

To analyze the spatial clusters of COVID-19 with respect to gender, race, and ethnicity, a purely spatial analysis was conducted using the spatial scan statistic of the discrete Poisson model implemented in the SaTScan software [94].

Briefly, we assumed that the COVID-19 cases followed the Poisson model because we were interested in the geographical distribution of the COVID-19 cases associated with demographic factors, adjusting for each population of the demographic factors. The retrospective space analysis used a circular window that moved in one dimension, using the base of the cylindrical window as the space dimension. The maximum cluster size was set to 25% of the population at risk to avoid extremely large clusters. Thus, numerous overlapping windows of different sizes were generated, which together covered the entire study area. Each circular window was considered a possible candidate cluster. Each cylinder was expanded until a maximum cluster size upper bound was reached. A likelihood ratio test was used to identify the spatial clusters of COVID-19 cases [92]. Hence, the null and alternative hypotheses were as follows:

$H_0$: the disease risk remains the same inside and outside the scanning window.

$H_a$: the risk within the window is different from that outside the window.

The remainder of the spatial analysis, such as performing the likelihood ratio test and

determining the p-value using Monte Carlo simulations, is identical to the prospective space-time analysis discussed in Chapter 3.

## 4.4 Results

### Descriptive and Time Series Analysis

We obtained the temporal variations in the number of COVID-19 cases between March and November 2020. Figure 10.a shows the weekly cases per thousand by gender in Kansas City. Males and females populations had similar trends and similar rates of cases. Figure 10.b shows the weekly cases per thousand by race in Kansas City. The three races are White, African American, and Hispanic/Latino. Hispanic/Latino always had the highest rate of cases. Before the $36^{th}$ week, African-American individuals had higher rates than White individuals. After the $36^{th}$ week, African American and White individuals had similar trends and rates of cases. The three races had a close trend and rate of cases from week 44 to week 46.

Also, we completed the descriptive analysis involving gender, race and ethnicity. Figure 10.c shows the prevalence of COVID-19 cases with respect to gender. As we noticed, there was slightly differences between the prevalence with respect to gender. Figure 10.d shows the prevalence of COVID-19 cases with respect to race and ethnicity. Note that Hispanic/Latino individuals has the highest prevalence of COVID-19 cases in Kansas City, MO while White individuals had the lowest prevalence. The prevalence was calculated by dividing the number of cases within a specific demographic group by the total number of individuals belonging to that same demographic group in Kansas City, MO, and multiplying that decimal by 1,000 to obtain the prevalence per 1,000 individuals.

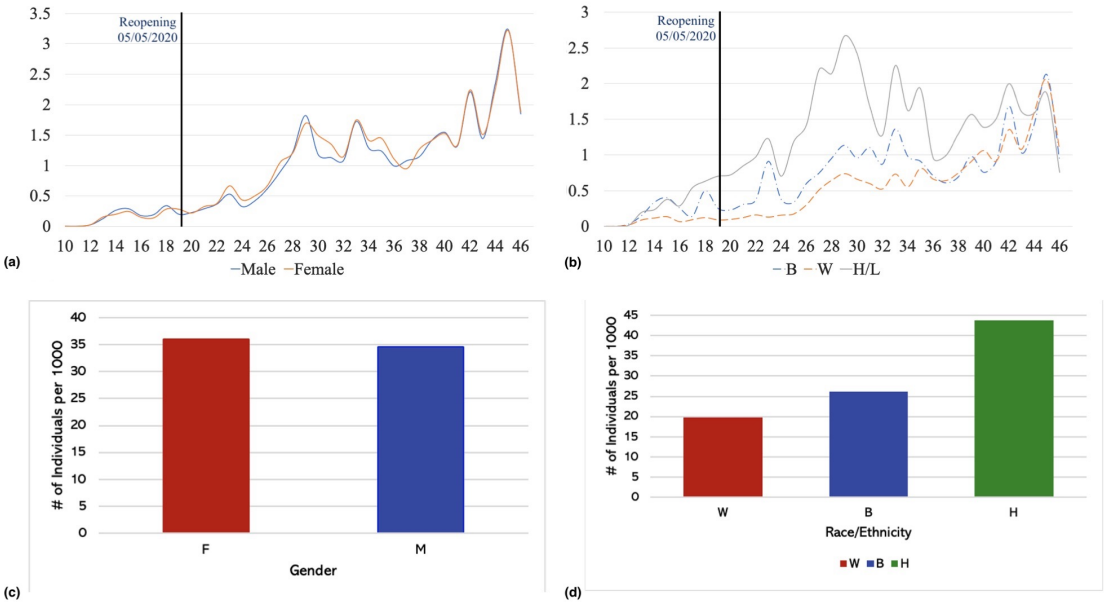


Figure 10: Time series and prevalence of COVID-19 cases in Kansas City, MO during March–November 2020 with respect to gender, race and ethnicity. (a) number of weekly new cases per thousand by gender, (b) number of weekly new cases per thousand by race and ethnicity. (c) Prevalence of COVID-19 cases with respect to gender from March to November 2020, and (d) Prevalence of COVID-19 cases in Kansas City with respect to race and ethnicity from March to November 2020.

## Cluster Analysis Results

The results of the cluster analysis were divided into two parts: spatial clusters of COVID-19 with respect to gender, and spatial clusters of COVID-19 with respect to race and ethnicity.

Figure 11.a and Table 8 provide the characteristics of the spatial clusters of COVID-19 with respect to gender in Kansas City at the zip code level from March

to November 2020. We observed five statistically significant clusters of females and eight clusters of males. The relative risks (RRs) of the primary clusters F1 (female) and M1 (male) are almost the same, and both clusters were in downtown Kansas City, located in Jackson County. As we can see in Figure 11.a, the clusters of the male population were more scattered than those of the female population. Also, we noticed that the male and female populations shared three clusters.

Figure 11.b and Table 9 provide details of the spatial COVID-19 clusters with respect to White and African American populations in Kansas City at the zip code level from March to November 2020. There were five spatial clusters belonging to African American, and three spatial clusters belonging to the White population. Note that the RR for the primary cluster (W1) of the White population is almost twice that of the RR for the primary cluster (B1) of the African American population. However, cluster B5 had a greater RR than that of primary cluster B1. Figure 11.b shows that the clusters of the African American and White populations are mainly shared in Clay County. Note that the secondary cluster B2 of the African American population covered almost the entire county.

Table 8: Spatial clusters of COVID-19 with respect to Female (F) and Male (M) populations at the zip code level.

| Cluster | RR | Observed | Expected | Counties | #of locations | P-value |
|---|---|---|---|---|---|---|
| Cluster F1 | 2.21 | 1907 | 974 | Jackson County | 9 | $1 \times 10^{-17}$ |
| Cluster F2 | 1.41 | 1421 | 1052 | Clay County<br>Platte County | 11 | $1 \times 10^{-17}$ |
| Cluster F3 | 1.52 | 253 | 168 | Jackson County | 1 | $1.2 \times 10^{-7}$ |
| Cluster F4 | 2.1 | 58 | 28 | Jackson County | 1 | $6.4 \times 10^{-5}$ |
| Cluster F5 | 1.11 | 1913 | 1757 | Jackson County | 7 | $4 \times 10^{-3}$ |
| Cluster M1 | 2.28 | 1848 | 927 | Jackson County | 9 | $1 \times 10^{-17}$ |
| Cluster M2 | 2.18 | 1357 | 683 | Jackson County | 7 | $1 \times 10^{-17}$ |
| Cluster M3 | 1.32 | 1195 | 937 | Clay County<br>Platte County | 11 | $2.3 \times 10^{-15}$ |
| Cluster M4 | 1.34 | 858 | 656 | Platte County | 8 | $1.1 \times 10^{-12}$ |
| Cluster M5 | 1.56 | 220 | 143 | Jackson County | 1 | $2.8 \times 10^{-7}$ |
| Cluster M6 | 1.27 | 472 | 377 | Jackson County | 3 | $1.7 \times 10^{-4}$ |
| Cluster M7 | 1.18 | 942 | 811 | Clay County<br>Jackson County | 7 | $2.5 \times 10^{-4}$ |
| Cluster M8 | 1.19 | 625 | 531 | Jackson County | 3 | $3.8 \times 10^{-3}$ |

Table 9: Spatial clusters of COVID-19 with respect to race and ethnicity at the zip code level: White population (W) and African American population (B).

| Cluster | RR | Observed | Expected | Counties | #of locations | P-value |
|---|---|---|---|---|---|---|
| Cluster W1 | 3.78 | 1247 | 388 | Jackson County | 11 | $1 \times 10^{-17}$ |
| Cluster W2 | 1.74 | 12717 | 801 | Clay County<br>Platte County | 11 | $1 \times 10^{-17}$ |
| Cluster W3 | 1.38 | 1708 | 1343 | Jackson County | 13 | $1 \times 10^{-17}$ |
| Cluster B1 | 1.89 | 798 | 474 | Clay County<br>Platte County<br>Jackson County | 18 | $1 \times 10^{-17}$ |
| Cluster B2 | 1.97 | 681 | 383 | Clay County<br>Platte County<br>Jackson County | 23 | $1 \times 10^{-17}$ |
| Cluster B3 | 1.62 | 113 | 71 | Jackson County | 1 | $2.6 \times 10^{-4}$ |
| Cluster B4 | 1.64 | 85 | 53 | Jackson County | 3 | $2.4 \times 10^{-3}$ |
| Cluster B5 | 2.88 | 18 | 6 | Jackson County | 1 | 0.012 |

Figure 11.c and Table 10 show the spatial clusters of COVID-19 with respect to Hispanic population in Kansas City at the zip code level from March to November 2020. There were seven spatial clusters of Hispanic population. These clusters had the highest prevalence compared to those of the African American and White populations, and they were scattered mainly in Jackson County. However, cluster H4 of the Hispanic population had an extremely large RR of 4.77.

Figure 11.d and Table 10 show the clusters that belong to other races, including Asian, American Indian, and Hawaiian and pacific islander populations. The spatial clusters for these races were located in Jackson County, specifically downtown Kansas

City. We noticed that the RRs of the primary clusters H1 and O1 are almost the same. However, cluster H4 of the Hispanic population had an extremely large RR.

Table 10: Spatial clusters of COVID-19 with respect to Hispanic (H) and Other (O) populations (i.e., Asian, American Indian, and Hawaiian and pacific islander).

| Cluster | RR | Observed | Expected | Counties | #of locations | P-value |
|---|---|---|---|---|---|---|
| Cluster H1 | 2.16 | 985 | 583 | Jackson County | 5 | $1 \times 10^{-17}$ |
| Cluster H2 | 2.17 | 516 | 269 | Jackson County | 5 | $1 \times 10^{-17}$ |
| Cluster H3 | 1.76 | 505 | 316 | Jackson County | 3 | $1 \times 10^{-17}$ |
| Cluster H4 | 4.77 | 61 | 13 | Jackson County | 1 | $1 \times 10^{-17}$ |
| Cluster H5 | 1.69 | 467 | 301 | Jackson County | 6 | $1 \times 10^{-17}$ |
| Cluster H6 | 1.90 | 95 | 51 | Jackson County | 1 | $2.4 \times 10^{-6}$ |
| Cluster H7 | 2.39 | 47 | 20 | Platte County | 1 | $1.9 \times 10^{-5}$ |
| Cluster O1 | 2.61 | 116 | 54 | Jackson County | 4 | $1.1 \times 10^{-14}$ |
| Cluster O2 | 2.38 | 57 | 26 | Jackson County | 1 | $1.8 \times 10^{-6}$ |
| Cluster O3 | 2.31 | 59 | 28 | Jackson County | 3 | $2.6 \times 10^{-6}$ |


Figure 11: Emerging spatial clusters of COVID-19 in Kansas City, MO with respect to demographic factors. Spatial clusters with respect to (a) gender: Female and male populations , (b) White and African American populations, (c) Hispanic population, and (d) other races, i.e., Asian, American Indian, and Hawaiian and pacific islander (Red color represents the primary cluster).

## 4.5 Discussion and Conclusions

Spatial cluster analysis is often utilized to identify regions with an increased risk of occurrence of studied phenomena. Studying the cluster patterns of COVID-19 can provide evidence for specific risk factors that influence the spread of the virus, establishing prevention and control measures. Understanding the spatial patterns can also enable public health departments and decision-makers to implement more COVID-19 vaccination clinics in high-risk areas and control the severity and spread of disease. Thus, the results of the study can assist the KCMO Health Department in developing more effective prevention strategies in future.

The main purpose of the present study was to provide an unbiased spatial and temporal analysis of COVID-19 data in Kansas City, MO. We examined significant differences in COVID-19 clusters with respect to demographic factors of gender, race, and ethnicity. Our research is the first study to utilize retrospective spatial statistics adjusted for demographic factors to monitor COVID-19 in Kansas City, MO.

Retrospective spatial analysis was able to identify eight clusters belonging to male populations, five spatial clusters for African American populations, and seven spatial clusters representing Hispanic populations, which had the most scattered clusters and the highest prevalence of COVID-19 cases when compared to those of the African American and White populations. Most of the spatial demographic clusters concentrated in downtown Kansas City, located in Jackson County.

We also monitored the temporal variations in the number of COVID-19 cases between March and November 2020. The time series of the cases had multiple M-shaped (double-top) curves. There were three obvious M-shaped curves that showed

the increase in cases occurring with a type of period. Five weeks after reopening, a continuous increase appeared for four weeks, followed by the appearance of an M-shaped curve. Reopening influenced weekly new COVID-19 cases in the short term. In addition, compared to the time series of weekly cases per thousand for Clay County and Platte County, Jackson County had the greatest number of cases per thousand for the first 24 weeks. However, after the $37^{th}$ week, the COVID-19 outbreak shifted. The trend and number of cases per thousand for the three counties became similar. The time series of Hispanic/Latino cases led the temporal trend until the $44^{th}$ week.

Despite the contributions of our study, there are several limitations and assumptions. First, to understand why certain communities have been severely impacted by the pandemic, it is important to study the health inequities and social determinants of health that contribute to current conditions. Certain factors such as socioeconomic status, income, healthcare access, and barriers, such as language and immigration status, may impact the spread of COVID-19 across regions. For instance, cluster H4 of the Hispanic population had an extremely large RR of 4.77. The region of this cluster covered three blocks east of Highway 71 and north of E. 75th Street. Of 361 Hispanic individuals in this region, 61 (16.8%) tested positive for COVID-19. Therefore, it is important to study the factors that impact the spread of COVID-19 in such areas. Being uninsured is another factor that may prevent individuals from seeking proper COVID-19 testing and treatments. In Kansas City, MO, the age-adjusted death rate for Hispanics is 2.7 times higher than for White residents, and the age-adjusted death rate for African Americans is 1.6 times higher than for White residents [24]. Hence, pre-existing medical conditions and access to

healthcare may have contributed to the disproportionate impact of COVID-19 on the Hispanic community. Moreover, some researchers suggested that COVID-19 cases in Kansas City, MO were related to income level [134]. The health risk gap narrows as the median income rises, and being white and having a higher median income offers a significant advantage compared to racial and ethnic minority groups with lower median incomes [134]. So, income level also contribute to the disproportionate impact of COVID-19 on certain communities. Second, only confirmed cases were included in the KCMO Health Department data, and it is vital to note that unconfirmed and probable cases are not evaluated owing to unavailability and uncertainty. As a result, a full perspective on the impact of COVID-19 in Kansas City, MO on certain communities will be impossible to obtain for some time. Third, our results focus on data from March–November of 2020, which was prior to vaccine distribution. Therefore, trends, number of emerging clusters, and relative risks would likely be different if we updated the current data. Lastly, COVID-19 is more severe in the elderly [117, 133]. Hence, the examine spatial clusters with respect to demographic factors that adjust for age and other abovementioned factors (socioeconomic status, income level, and healthcare access) can improve the full perspective of spreading the disease in Kansas City,MO.

# CHAPTER 5

# MODELING COVID-19 TRANSMISSION WITHIN AND BETWEEN THE SPATIAL CLUSTERS

## 5.1 Overview

Due to the recurring threats posed by the newly emerging and high-profile contagious disease COVID-19, epidemiologists have paid close attention to the spread of infectious diseases [157]. Because long time-series data for diseases is required, it is challenging to identify transmission rules and provide empirical control measures. As a result, it may provide helpful information by developing a mathematical model to describe disease spread between communities. Mathematical epidemiology can estimate the formation of large-scale spatial patterns and disease transmission velocity and guide policy decisions for disease control.

In this chapter, we presented a COVID-19 spatial transmission model that utilized ordinary differential equations for cluster environment. The clusters connected through human mobility, as measured by long-distance travel and short-distance commutes. We assumed that disease transmission is possible during travel. Also, recovered individuals could lose their immunity and be susceptible again. Mathematically, we studied three different cases of spatial transmission of individuals traveling between n-cluster, 2-cluster, and single cluster. The positivity and boundedness of the model solutions were discussed. An expression for the basic reproduction number $R_0$ for single and 2-cluster was derived. Analytically, we showed the existence of the

disease-free and endemic equilibriums. Also, the disease-free equilibrium was proved to be locally and globally asymptotically stable for $R_0 < 1$.

Numerically, we showed that human behaviors and beliefs significantly impact the spread of the disease in local communities. Also, we showed that the inequities in vaccination rates across communities would negatively impact the other communities and contributes to the development of new infected cases in neighboring communities.

## 5.2 Model Formulation of n-Cluster

To create a mathematical model that describes the spatial transmission of the disease in the community, we made certain assumptions based on long-distance travel and short-distance commutes.

- The first assumption is the effects of global factors on the spread of the disease in the community. The global effects have been fully described in Chapter 6 in three different cases: the individuals return to the community without any exposure to the infection, the individuals can be exposed and develop symptoms after returning to the community, or the individuals can be tested positive during the trip and remain quarantined until fully recovered.
- The second assumption is that we assumed the disease transmission is possible during daily commutes after the susceptible individual gets in contact with an infected individual who travels from the endemic cluster.
- The third assumption is that recovered individuals can lose their immunity and be susceptible again.

Given the above-mentioned assumptions, the set of ordinary differential equations representing the model is given by the following set of equations:

$$\begin{aligned}
\frac{dS_i}{dt} &= \Lambda_i - \frac{\beta S_i I_i}{N_i} + \theta \sum_{\substack{j=1 \\ j\neq i}}^{n} m_{ij} S_j - \theta \sum_{\substack{j=1 \\ i\neq j}}^{n} m_{ji} S_i + \alpha R_i - (p_i + d_i)\, S_i + f_i(t). \\
\frac{dI_i}{dt} &= \frac{\beta S_i I_i}{N_i} + \theta \sum_{\substack{j=1 \\ j\neq i}}^{n} m_{ij} I_j - \theta \sum_{\substack{j=1 \\ i\neq j}}^{n} m_{ji} I_i - (\gamma + \mu_i + d_i)\, I_i + g_i(t). \\
\frac{dR_i}{dt} &= \gamma I_i - (\alpha + d_i)\, R_i + p_i S_i + h_i(t).
\end{aligned} \tag{5.1}$$

Where $N_i = S_i(t) + I_i(t) + R_i(t)$.

The model (5.1) represents the spatial transmission of people traveling between n- clusters or locations with incorporate the global effects. A compartmental diagram of the proposed n-cluster model is seen in Figure 12, and a summary of parameters and variables is given in Table 11.

Table 11: Summary of the variables and parameters used in the n-cluster model (5.1).

| Symbol | Description |
|---|---|
| $N_i$,$N_j$ | Total population in cluster i and cluster j, respectively |
| $S_i$,$S_j$ | Susceptible population in cluster i and cluster j, respectively. |
| $I_i$,$I_j$ | Susceptible population in cluster i and cluster j, respectively. |
| $R_i$ | Recovered population in cluster i. |
| $\beta$ | Transmission rate of the disease. |
| $\gamma$ | Recovery rate |
| $m_{ij}$ | Daily number of people traveling from cluster j to cluster i. |
| $m_{ji}$ | Daily number of people returning from cluster i to cluster j. |
| $\theta$ | Multiplicative factor to reflect underreporting of human movement. |
| $\alpha$ | Proportion of people who lose immunity and go back to susceptible population. |
| $\Lambda_i$ | Constant recruitment rate in cluster i. |
| $p_i$ | Vaccination rate in cluster i. |
| $d_i$ | Mortality rate in cluster i (Natural death rate). |
| $\mu_i$ | Death rate in cluster i. |
| $f_i$, $g_i$, and $h_i$ | Global effects in cluster i. |

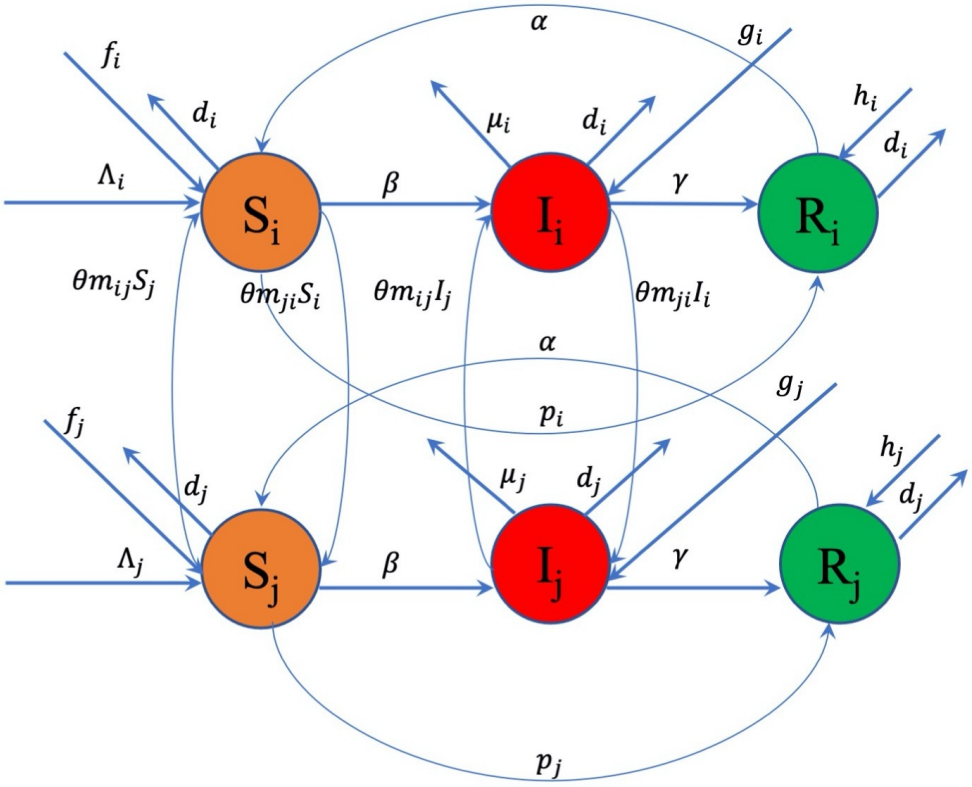


Figure 12: A compartmental diagram of the spatial model (5.1). See Table 11 for a summary of the parameters and variables.

## 5.3 Well-Posedness of n-Cluster Model

In this section, we proved that the model solutions are always non-negative and bounded provided that the initial conditions is non negative.

THEOREM 5.1. If the parameter values and the initial condition of the model (5.1) are non-negative then the solutions of the system (5.1) are non-negative and bounded.

PROOF. For the model (5.1), it can be verified that all solutions with non-negative initial conditions remain non-negative. Letting $N_i = S_1 + I_1 + R_1 + ... + S_i + I_i + R_i$ where $i = 1, ..., n$. Adding the equations of the model (5.1) gives:

$$\frac{dN}{dt} = \sum_{i=1}^{n} \Lambda_i - d_i N_i - \mu_i I_i \leq \sum_{i=1}^{n} \Lambda_i - (d_i + \mu_i) N_i \tag{5.2}$$

Then, $\limsup_{t\to\infty} \mathrm{N(t)} \leq \Lambda_i / (d_i + \mu_i)$. Hence, the feasible region:

$$\Gamma = \left\{ (S_i, I_i, R_i) \in \mathbb{R}^3_+ \mid S_i + I_i + R_i \leq \sum_{i=1}^{n} \Lambda_i / (d_i + \mu_i), i = 1, 2, \ldots, n \right\} \tag{5.3}$$

is positively invariant with respect to model (5.1). □

## 5.4 Analysis of n-Cluster Model

### Existence of Equilibria

In this section, we showed that the spatial model admitted a unique endemic equilibrium for single cluster and n-cluster when the basic reproduction number is greater than 1. Also, we proved the local and global stability of disease-free equilibrium. However, we need first to show how many equilibria the model has when we

have n-clusters.

THEOREM 5.2. The n-cluster model (5.1) has at most $2^n$ equilibrium solutions with non-negative coordinates.

PROOF. Let $S$ is the set of all equilibrium solutions:
$(S_1^*, \cdots, S_n^*, I_1^* \cdots, I_n^*, R_1^*, \cdots, R_n^*)$. The trivial equilibrium solution is the Disease-Free Equilibrium (DFE) where, $I_1^* \cdots, I_n^* = 0$ Also note that at each equilibrium solution we have $R_i^* = N_i^* - (S_i^* + I_i^*)$ as a function of $S_i^*$ and $I_i^*$ So we only need to count the cases that we have none, one, two, $\cdots$, clusters with positive numbers of infected individuals. This leads to the sum of the combinations

$$\begin{pmatrix} n \\ 0 \end{pmatrix} + \begin{pmatrix} n \\ 1 \end{pmatrix} + \begin{pmatrix} n \\ 2 \end{pmatrix} + \begin{pmatrix} n \\ 3 \end{pmatrix} + \ldots \begin{pmatrix} n \\ n \end{pmatrix} = 2^n \tag{5.4}$$

which equals the total number of equilibrium solutions of model (5.1).
Hence, the model has at most $2^{\mathrm{n}}$ equilibrium solutions with non-negative coordinates.

□

It is important to note that we can have $m$ active clusters and $n-m$ inactive clusters. We mean by active cluster that an endemic status has reached in that cluster. Suppose that clusters $k_1, k_2, ..., k_m$ are active clusters. Then, $I_{k_j} > 0$ for $1 \leq j \leq m$ and the corresponding endemic equilibrium is denoted by $E_{k_1,\cdots,k_m}$

THEOREM 5.3. The n-cluster model (5.1) admits a unique endemic equilibrium $E_{k_i}$ if the corresponding basic reproduction number $R_0^{[i]} > 1$.

PROOF. Let us assume that the system (5.1), has a unique equilibrium at EE = $(\mathrm{S}_i^*, \mathrm{I}_i^*, \mathrm{R}_i^*)$ for $i = 1, ..., n$ such that:

$$\mathrm{S}_i^* = \frac{N_i{}^* \left(\gamma + \mu_i + d_i\right)}{\beta} \tag{5.5}$$

and,

$$I_i^* = \frac{\Lambda_i - \frac{N_i^*(\mathrm{p_i}+\mathrm{d_i})(\gamma+\mu_i+d_i)}{\beta} + \frac{N_i^*\alpha \mathrm{p}_i r(\gamma+\mu_i+d_i)}{\beta}}{(\gamma + \mu_i + d_i) - \alpha\gamma r} \tag{5.6}$$

Where $\mathrm{r} = \frac{1}{\alpha+\mathrm{d}_i}$. We need to prove the model has positive endemic equilibrium if $R_0^{[i]} > 1$. Later, we will show that for n=1, the basic reproduction number is given by:

$$R_0^{[i]} = \frac{\beta\Lambda_i}{N_i^*(p_i + d_i - r\alpha p_i)(\gamma + \mu_i + d_i)} \quad \text{where } r = \frac{1}{\alpha + d_i}$$

We can re-write $S_i^*$ and $I_i^*$ in the term of $R_0^{[i]}$ such that:

$$S_i^* = \frac{\Lambda_i}{\left(\mathrm{p}_i + \mathrm{d}_i - \mathrm{r}\alpha\mathrm{p}_i\right) R_0^{[i]}} \tag{5.7}$$

And,

$$I_i^* = \frac{\left(\mathrm{p}_i + \mathrm{d}_i - \mathrm{r}\,\alpha\mathrm{p}_i\right)\left(\gamma + \mu_i + d_i\right)}{\beta\left(\gamma + \mu_i + d_i\right) - \alpha\gamma r}\left(R_0^{[i]} - 1\right) \tag{5.8}$$

The model has no positive endemic equilibrium if $R_0^{[i]} < 1$ since $S_i^*$ and $I_i^*$ would be negative, which indicate unrealistic biological system.

Hence, for a positive endemic equilibrium system, we would require that $R_0^{[i]} > 1$. □

THEOREM 5.4. The n-cluster model admits endemic equilibrium $E^*_{k_1,\cdots,k_m}$ if and only if $R_0^{[j]} > 1$ for all $j = k_1, k_2, ..., k_m$.

PROOF. We proved the theorem in two parts.

Part a) suppose that $\mathrm{R}_0^{[j]} > 1$ for all $\mathrm{j} = k_1, k_2, \ldots, k_m$. Now we need to show that the endemic equilibrium $E^*_{k1,k2,\ldots,km}$ with nonnegative coordinates exist.

Let $\Lambda = \sum_{j=1}^{m} \Lambda_j, d = \sum_{j=1}^{m} \mathrm{d}_j, p = \sum_{j=1}^{m} \mathrm{p}_j, \mu = \sum_{j=1}^{m} \mu_j, N = \sum_{j=1}^{m}, \mathrm{N}_j$ where $\Lambda_j, \mathrm{d}_j, \mathrm{p}_j$, and $\mu_j$ are arbitrary positive constant.

Then, the endemic equilibrium $E_{k1,k2,\ldots,km}$ should satisfying the following m systems for $\mathrm{j} = k_1, k_2, \ldots, k_m$.

$$S'_j = \Lambda_j - \frac{\beta S_j I_j}{N_j} + \alpha r \left(\gamma I_j + p_j S_j\right) - \left(p_j + d_j\right) S_j \tag{5.9}$$

Where $\mathrm{r} = \frac{1}{\alpha + \mathrm{d_j}}$

$$I'_j = \frac{\beta S_j I_j}{N_j} - \left(\gamma + \mu_j + d_j\right) I_j \tag{5.10}$$

So, similar to the proof of Theorem 5.3, we write $S^*_j$ and $I^*_j$ in the term of $R_0^{[j]}$:

$$S^*_j = \frac{\Lambda_\mathrm{j}}{\left(\mathrm{p_j} + \mathrm{d_j} - \mathrm{r}\alpha\mathrm{p_j}\right) R_0^{[j]}} \tag{5.11}$$

And,

$$I^*_j = \frac{\left(\mathrm{p}_j + \mathrm{d_j} - \mathrm{r}\alpha\mathrm{p_j}\right)\left(\gamma + \mu_j + d_j\right)}{\beta\left(\gamma + \mu_j + d_j\right) - \alpha\gamma r} \left(R_0^{[j]} - 1\right) \tag{5.12}$$

Hence, for a positive endemic equilibrium for the system (5.1), we would require that $R_0^{[j]} > 1$.

Therefore, the n-cluster model admitted an endemic equilibrium $E_{k1,k2,\ldots,km}$ if $R_0^{[j]} > 1$.

Part b) Suppose that the endemic equilibrium $E_{k1,k2,\ldots,km}$ with nonnegative

coordinates exists. Now we need to show that $\mathrm{R}_0^{[j]} > 1$ for all $\mathrm{j} = k_1, k_2, \ldots, k_m$.

Since endemic equilibrium $E_{k1,k2,\ldots,km}$ exists, we must have $I_j^* > 0$.
Hence by equation (5.12) we must have $R_0^{[j]} - 1 > 0$. This completes the proof. □

**Local Stability of Disease Free Equilibrium**

In this section, we need to show the local stability of the disease free equilibrium. Local stability means that the solutions with initial values close to the equilibrium remain close to the equilibrium and approach the equilibrium.

THEOREM 5.5. The disease-free equilibrium is unique and locally asymptotically stable if the basic reproduction number $R_0 < 1$.

PROOF. To consider the local stability of the DFE of the model (5.1), let have $u = (I_1, I_2, ..., I_n)^T$ is the vector of infected variable. The DFE is locally asymptotically stable if all eigenvalues of the Jacobian matrix of the model (5.1) have negative real parts, where,

$$J_{DFE} = \begin{bmatrix} F - V & 0 \\ 0 & J_4 \end{bmatrix} \tag{5.13}$$

The eigenvalues of the $J_{DFE}$ are the eigenvalues of $F - V$ and the eigenvalues of $J_4$. To determine, $F$ and $V$, consider the right hand side of the model, and written $F - V$, where,

$$F = \begin{bmatrix} \frac{\beta S_1 I_1}{N_1} \\ \frac{\beta S_2 I_2}{N_2} \\ \vdots \\ \frac{\beta S_n I_n}{N_n} \end{bmatrix} \tag{5.14}$$

And,

$$V = \begin{bmatrix} -\theta \sum_{j=1}^{n} m_{1j} I_j + \theta \sum_{j=1}^{n} m_{j1} I_1 + (\gamma + \mu_1 + d_1) I_1 \\ -\theta \sum_{j=1}^{n} m_{2j} I_j + \theta \sum_{j=1}^{n} m_{j2} I_2 + (\gamma + \mu_2 + d_2) I_2 \\ \vdots \\ -\theta \sum_{j=1}^{n} m_{nj} I_j + \theta \sum_{j=1}^{n} m_{jn} I_n + (\gamma + \mu_n + d_n) I_n \end{bmatrix} \tag{5.15}$$

Here, $F$ matrix is for new infections, and $V$ matrix is for transfer the infections. Linearising, $F - V$ about the DFE gives the matrix $F - V$, where, $F = [\frac{\partial F_i}{\partial u_j}]$, and $V = [\frac{\partial V_i}{\partial u_j}]$. Block matrices $F$ and $V$ are given by:

$$F = \begin{bmatrix} F_{11} & 0 \\ 0 & 0 \end{bmatrix}, V = \begin{bmatrix} V_{11} & 0 \\ 0 & 0 \end{bmatrix}$$

Where,

$$F_{11} = \begin{bmatrix} \frac{\beta S_1^*}{N_1^*} & 0 & \dots & 0 \\ 0 & \frac{\beta S_2^*}{N_2^*} & \dots & 0 \\ \vdots & \dots & & \frac{\beta S_n^*}{N_n^*} \end{bmatrix} \tag{5.16}$$

And,

$$V_{11} = \begin{bmatrix} \theta \sum_{j=1}^{n} m_{j1} + (\gamma + \mu_1 + d_1) & -\theta m_{12} & \dots & -\theta m_{1n} \\ -\theta m_{21} & \theta \sum_{j=1}^{n} m_{j2} + (\gamma + \mu_2 + d_2) & \dots & -\theta m_{2n} \\ \vdots & \ddots & & \\ -\theta m_{n1} & \dots & & \theta \sum_{j=1}^{n} m_{jn} + (\gamma + \mu_n + d_n) \end{bmatrix} \tag{5.17}$$

By Theorem (A1), $V_{11}$ are non-singular M-matrix. Hence, by Theorem (A2), $V_{11}$ has

positive inverse.

Now, For $J_4 = \begin{bmatrix} -C & 0 \\ 0 & -G \end{bmatrix}$, where,

$$G = \begin{bmatrix} \alpha + d_1 & 0 & \dots & 0 \\ 0 & \alpha + d_2 & \dots & 0 \\ \vdots & \ddots & & \\ 0 & & \dots & \alpha + d_n \end{bmatrix} \tag{5.18}$$

And,

$$C = \begin{bmatrix} \theta \sum_{j=1}^{n} m_{j1} + (p_1 + d_1) & -\theta m_{12} & \dots & -\theta m_{1n} \\ -\theta m_{21} & \theta \sum_{j=1}^{n} m_{j2} + (p_2 + d_2) & \dots & -\theta m_{2n} \\ \vdots & \ddots & & \\ -\theta m_{n1} & \dots & & \theta \sum_{j=1}^{n} m_{jn} + (p_n + d_n) \end{bmatrix} \tag{5.19}$$

Where $G$ is the coefficient matrix for $R(t)$ compartments, and $C$ is the coefficient matrix for $S(t)$ compartments. $G$ and $C$ are non-singular M-matrices. Thus, by Theorem (A3), $J_4$ has all eigenvalues with negative real parts. Hence, the local stability of the DFE depends only on the eigenvalues of $F - V$. By Theorem (A4), all eigenvalues of $F - V$ have negative real parts if and only if $s(F - V) < 0$ if and only if $\rho(FV^{-1}) < 1$. Since $V$ has a positive inverse, then, $FV^{-1}$ is a non-negative matrix, Where,

$$FV^{-1} = \begin{bmatrix} F_{11} & 0 \\ 0 & 0 \end{bmatrix} \begin{bmatrix} V_{11}^{-1} & 0 \\ 0 & 0 \end{bmatrix} = \begin{bmatrix} F_{11}V_{11}^{-1} & 0 \\ 0 & 0 \end{bmatrix} \tag{5.20}$$

So, $R_0 = \rho(FV^{-1})$. By Theorem (A4), If $R_0 < 1$, then $s(F - V) < 0$. Therefore, all the eigenvalues lie in the left half plane, and according to the Definition (A5), the n-cluster model (5.1) is local asymptotically stable.

On the other hand, if $\mathcal{R}_0 > 1$ then $s(F - V) > 0$, therefore at least one eigenvalue lies in the right half plane and according to Definition (A5), the system (5.1) is unstable.

□

**Global Stability of the Disease-Free Equilibrium**

In this section, we need to prove the global stability of disease free equilibrium. When the basic reproduction number $R_0 < 1$, all solutions converge to the disease-free equilibrium, that is, the disease dies out eventually.

THEOREM 5.6. The disease free equilibrium of the system (5.1) is globally asymptotically stable if $R_0 < 1$ and unstable if $R_0 > 1$.

PROOF. From Theorem 5.5, If $R_0 < 1$, then the DFE of the model (5.1) is locally asymptotically stable, and if $R_0 > 1$, then the DFE is unstable. Consider $R_0 < 1$ and a positive solution of the system (5.1). To complete the proof, it is sufficient to show that this positive solution tends to the DFE as $t \to \infty$. From equation of $I(t)$:

$$\frac{dI_i}{dt} = \frac{\beta S_i I_i}{N_i} + \theta \sum_{\substack{j=1 \\ j \neq i}}^{n} m_{ij} I_j - \theta \sum_{\substack{j=1 \\ i \neq j}}^{n} m_{ji} I_i - (\gamma + \mu_i + d_i) I_i. \tag{5.21}$$

The right side of the equation (5.21) has the coefficient matrix of $F - V$. For $R_0 =$

$\rho(FV^{-1} < 1)$, each eigenvalues of $F - V$ lies in the left half plane (by Theorem A4). Hence, each positive solution of (5.21) satisfies $\lim_{t\to\infty} I_i(t) = 0$. Since equation (5.21) is a linear system, the DFE of (5.21) is globally asymptotically stable. From the equation of $R(t)$:

$$\frac{dR_i}{dt} = \gamma I_i - (\alpha + d_i) R_i + p_i S_i. \tag{5.22}$$

Since each positive solution of $I_i(t)$ tends to zero as $t \to \infty$, then,
$\frac{dR_i}{dt} = -(\alpha + d_i) R_i + p_i S_i$ as $t \to \infty$. This linear system has coefficient matrix of $-G$ with $G$ as defined in the proof of Theorem 5.5, therefore $\lim_{t\to\infty} R_i(t) = 0$ since all eigenvalues of $-G$ lie in the left half plane. From the equation of $S(t)$:

$$\frac{dS_i}{dt} = \Lambda_i - \frac{\beta S_i I_i}{N_i} + \theta \sum_{\substack{j=1 \\ j\neq i}}^{n} m_{ij} S_j - \theta \sum_{\substack{j=1 \\ i\neq j}}^{n} m_{ji} S_i + \alpha R_i - (p_i + d_i) S_i. \tag{5.23}$$

Since, $\lim_{t\to\infty} I_i(t) = 0$, and $\lim_{t\to\infty} R_i(t) = 0$, then,
$\frac{dS_i}{dt} = \Lambda_i + \theta \sum_{\substack{j=1 \\ j\neq i}}^{n} m_{ij} S_j - \theta \sum_{\substack{i=1 \\ i\neq j}}^{n} m_{ji} S_i - (p_i + d_i) S_i$. This is the system of differential equations

$$\frac{dS}{dt} = \Lambda - CS \tag{5.24}$$

Where, $\frac{dS}{dt} = [\frac{dS_1}{dt}, \frac{dS_2}{dt}, ..., \frac{dS_n}{dt}]^T$, $S = [S_1, S_2, ..., S_n]$, and $C$ is defined in the Theorem 5.5. The solutions of the equation (5.24) can be derived in two parts, namely, homogeneous and particular solutions. The homogeneous part is the solution of $\frac{dS}{dt} = -CS$. Since $-C$ is the negative of a non-singular M-matrix, by Theorem (A3) all its eigenvalues lie in the left half plane. Thus, $\lim_{t\to\infty} S_h(t) = 0$ with $S_h(t)$ denoting the homogeneous solution of (5.24). Matrix $C$ is an irreducible non-singular M-matrix

and therefore by Theorem (A2), it has a positive inverse. Therefore, $S^0 = C^{-1}\lambda$ is the particular solution for (5.24), and $S = S_h + S^0$ is the general solution for (5.24). Hence, $\lim_{t\to\infty} S_i = S_i^0$, completing the proof that the DFE is globally asymptotically stable. □

## 5.5 Special Cases of n-Cluster Model

In this section, we considered a particular two cases of the system (5.1) with n=1 and n=2. In the case n=1, the population dynamics among single cluster is given by a system of three ordinary differential equations. This represents the case that the clusters are isolated from each other. There n=1 does mean that we have only one cluster. It simply means that all clusters are isolated and do not affect each other. Therefore, there is no migration rates between clusters, so, $m_{ij} = \theta = 0$. In the case n=2, the population dynamics among two clusters is given by a system of six ordinary differential equations, and the migration rates will be between two clusters, so we have, $m_{12}$ and $m_{21}$.

### Single Cluster Model

The n-cluster system (5.1) with n=1 will be as following:

$$\begin{aligned}
\frac{dS_1}{dt} &= \Lambda_1 - \frac{\beta S_1 I_1}{N_1} + \alpha R_1 - (p_1 + d_1) S_1 \\
\frac{dI_1}{dt} &= \frac{\beta S_1 I_1}{N_1} - (\gamma + \mu_1 + d_1) I_1 \\
\frac{dR_1}{dt} &= \gamma I_1 - (\alpha + d_1) R_1 + p_1 S_1
\end{aligned} \tag{5.25}$$

Where $N_1 = S_1(t) + I_1(t) + R_1(t)$

Well-Posedness of Single cluster Model

In this section, we want to prove that the model solutions for single cluster are always non-negative and bounded provided that the initial conditions is non-negative.

COROLLARY 5.7. If the parameter values and the initial condition of the model (5.25) are non-negative, then the solutions of model (5.25) are non-negative and bounded.

PROOF. Corollary 5.7 is a direct implication of Theorem 5.1. We only need to let n=1, the rest follows. Specifically, for n=1, we have

$$\frac{dN}{dt} = \Lambda_1 - d_1 N_1 - \mu_1 I_1 \leq \Lambda_1 - (d_1 + \mu_1) N_1 \tag{5.26}$$

Then, $\limsup_{t\to\infty} \mathrm{N(t)} \leq \Lambda_1 / (d_1 + \mu_1)$. Hence, the feasible region:

$$\Gamma = \left\{ (S_1, I_1, R_1) \in \mathbb{R}^3_+ \mid S_1 + I_1 + R_1 \leq \Lambda_1 / (d_1 + \mu_1) \right\} \tag{5.27}$$

is positively invariant with respect to model (5.25). □

## Analysis of Single Cluster Model

### Existence of Disease-Free Equilibrium

At the disease-free equilibrium, we have an absence of infection. Thus, the infected compartment will have zero individuals and the entire population will comprise of susceptible and recovered individuals.

THEOREM 5.8. If the parameter values of the model (5.25) are non-negative, then the model will have a unique disease-free equilibrium that exists at the point ($S_1^*$, 0, $R_1^*$).

PROOF. We denote the disease-free equilibrium with ($S_1^*$, 0, $R_1^*$). At equilibrium state, the rate of change of each variable is equal to zero. i.e:

$$S_1' = I_1' = R_1' = 0$$

Hence, by setting the right-hand side of system (5.25) equal to zero, adding the two equations:

$$S_1' = \Lambda_1 - \frac{\beta S_1 I_1}{N_1} + \alpha R_1 - (p_1 + d_1)\, S_1$$

$$I_1' = \frac{\beta S_1 I_1}{N_1} - (\gamma + \mu_1 + d_1)\, I_1$$

and setting $I_1 = 0$, it becomes:

$$\Lambda_1 + \alpha {R_1}^* - (p_1 + d_1){S_1}^* = 0 \tag{5.28}$$

From equation:

$$R_1' = \gamma I_1 - (\alpha + d_1)\, R_1 + p_1 S_1$$

we got that:

$$R_1{}^* = \frac{p_1 S_1^*}{\alpha + d_1}$$

By substituting $R_1$ in (5.28), we got:

$$S_1^* = \frac{\Lambda_1}{p_1 + d_1 - r\alpha p_1} \quad \text{where } r = \frac{1}{\alpha + d_1} \tag{5.29}$$

And, we can re-write $R_1^*$ to be:

$$R^* = r p_1 S_1^*$$

Note that $N_1^* = S_1^* + R_1^*$. The uniqueness of DFE is straightforward, therefore it was omitted from the proof.

It remains to show that $S_1^*$ is always positive. We need to prove that $p_1 + d_1 - \frac{\alpha p_1}{r} > 0$ where $r = \alpha + d_1$.

So, $p_1 + d_1 > \frac{\alpha p_1}{r}$. Divided by $p_1$ for both sides, we got that:

$$\frac{d_1}{p_1} + 1 > \frac{\alpha}{\alpha + d_1}$$

Divided by $\alpha$ for both sides, we got that

$$\frac{d_1}{p_1} + 1 > \frac{1}{1 + \frac{d_1}{\alpha}}$$

Let: $\frac{d_1}{p_1} = a$, and $\frac{d_1}{\alpha} = b$. Hence, $a + 1 > \frac{1}{1+b}$

Then, $(a+1)(b+1) > 1$, so $ab + a + b + 1 > 1$

Then, $ab + a + b > 0$. Hence, $S_1^*$ is always positive and this completes the proof. □

### Basic Reproduction Number $R_0$ for Single Cluster

The basic reproduction number, $R_0$, is defined as the expected number of secondary infections produced by a single case of an infection introduced to a completely susceptible population [149]. The magnitude of $R_0$ determines the severity of infection. Larger values of $R_0 > 1$ lead to faster disease spread, whereas smaller values of $R_0 < 1$ lead to the disease dying out more rapidly.

Equilibrium points can be analyzed using $R_0$. The disease- free equilibrium is locally asymptotically stable if $R_0 < 1$ and unstable if $R_0 > 1$. Therefore, if $R_0 < 1$ , the disease will disappear from the community and die out, and if $R_0 > 1$ , the epidemic will occur in the community. On the other hand, the endemic equilibrium is locally stable when $R_0 > 1$ and unstable when $R_0 < 1$.

By using the Next Generation Matrix (NGM) [20, 149], the expression for $R_0$ can be derived for single cluster model (5.25). Specifically, the next generation matrix is given by $K = FV^{-1}$. Hence, we introduced two matrices, the first matrix, denoted $F$, containing infection terms and the second matrix, $V$, containing the transfer terms. The eigenvalues of the total new infections matrix (i.e, eigenvalues of $FV^{-1}$) are calculated. The basic reproduction number, therefore, is the largest of these eigenvalues. Mathematically, this can be summarized as follows:
$F = [\frac{\partial F_i(x_0)}{\partial x_j}]$, and $V = [\frac{\partial V_i(x_0)}{\partial x_j}]$ , where $F_i$ represents the new infections, $V_i$ represents the transfer terms, and the value $x_0$ represents the disease-free equilibrium.

Calculating the exact expression for $R_0 = \rho(FV^{-1})$ of the general n-cluster model (5.1) is very complicated unless n is a small positive integer. Here, we obtained the basic reproduction number for n=1 which corresponds to the system (5.25).

Therefore,

$$F = [\frac{\beta {S^*}_1}{{N^*}_1}].$$

$$V = -[-(\gamma + \mu_1 + d_1)].$$

Then,

$$K = FV^{-1} = [\frac{\frac{\beta {S^*}_1}{{N^*}_1}}{\gamma + \mu_1 + d_1}].$$

Note that we have only one eigenvalue.

Hence,

$$R_0^{[1]} = \frac{\beta \Lambda_1}{{N^*}_1(p_1 + d_1 - r\alpha p_1)(\gamma + \mu_1 + d_1)} \quad \text{where } r = \frac{1}{\alpha + d_1} \tag{5.30}$$

Note that $p_1 + d_1 - r\alpha p_1$ is always positive and therefore $R_0$ is well-defined.

**Existence of Endemic Equilibrium**

The disease cannot be totally eradicated at the endemic equilibrium, but it remains in the population. For the disease to persist in the population, susceptible, infected, and recovered compartments cannot be zero, i.e.: $EE = (S_1^*, I_1^*, R_1^*) \neq (0,\ 0,\ 0)$. To find the endemic equilibrium, we have to solve the system (5.25) simultaneously taking into consideration the fact that $(S_1^*, I_1^*, R_1^*) \neq (0,\ 0,\ 0)$.

THEOREM 5.9. The endemic equilibrium EE is unique and locally asymptotically stable if the basic reproduction number $R_0^{[1]} > 1$.

PROOF. Let us assume that the system (5.25), has a unique equilibrium at EE = $({S^*}_1, {I_1}^*, {R_1}^*)$ such that:

$$\mathrm{S}_1^* = \frac{{N_1}^* (\gamma + \mu_1 + d_1)}{\beta} \tag{5.31}$$

and,

$$I_1^* = \frac{\Lambda_1 - \frac{{N_1}^*(\mathrm{p_1}+\mathrm{d_1})(\gamma+\mu_1+d_1)}{\beta} + \frac{{N_1}^*\alpha \mathrm{p_1} r(\gamma+\mu_1+d_1)}{\beta}}{(\gamma + \mu_1 + d_1) - \alpha\gamma r} \tag{5.32}$$

Where $\mathrm{r} = \frac{1}{\alpha+\mathrm{d_1}}$. We need to prove the model has positive endemic equilibrium if $R_0^{[1]} > 1$. We can re-write $S_1^*$ and $I_1^*$ in the term of $R_0^{[1]}$ such that:

$$S_1^* = \frac{\Lambda_1}{(p_1 + d_1 - r\alpha p_1)R_0^{[1]}} \tag{5.33}$$

and,

$$I_1^* = \frac{(p_1 + d_1 - r\alpha p_1)(\gamma + \mu_1 + d_1)}{\beta(\gamma + \mu_1 + d_1) - \alpha\gamma r}(R_0^{[1]} - 1) \tag{5.34}$$

The model has no positive endemic equilibrium if $R_0^{[1]}$ since $S_1^*$ and $I_1^*$ would be negative, which indicate unrealistic biological system. If $R_0^{[1]} = 1$, then we would have the disease-free equilibrium that we discussed earlier in the previous section. Hence, for a positive endemic equilibrium system, we would require that $R_0^{[1]} > 1$.

□

**n-Cluster Model with n=2**

The 2-cluster model is a special case of n-cluster model when n=2, and it will be as the following:

$$
\begin{aligned}
\frac{dS_1}{dt} &= \Lambda_1 - \frac{\beta S_1 I_1}{N_1} + \theta m_{12} S_2 - \theta m_{21} S_1 + \alpha R_1 - (p_1 + d_1) S_1 \\
\frac{dI_1}{dt} &= \frac{\beta S_1 I_1}{N_1} + \theta m_{12} I_2 - \theta m_{21} I_1 - (\gamma + \mu_1 + d_1) I_1 \\
\frac{dR_1}{dt} &= \gamma I_1 - (\alpha + d_1) R_1 + p_1 S_1 \\
\frac{dS_2}{dt} &= \Lambda_2 - \frac{\beta S_2 I_2}{N_2} + \theta m_{21} S_1 - \theta m_{12} S_2 + \alpha R_2 - (p_2 + d_2) S_2 \\
\frac{dI_2}{dt} &= \frac{\beta S_2 I_2}{N_2} + \theta m_{21} I_1 - \theta m_{12} I_2 - (\gamma + \mu_2 + d_2) I_2 \\
\frac{dR_2}{dt} &= \gamma I_2 - (\alpha + d_2) R_2 + p_2 S_2
\end{aligned}
\tag{5.35}
$$

Where $\sum_{i=1}^{2} N = S_1(t) + I_1(t) + R_1(t) + S_2(t) + I_2(t) + R_2(t)$.

**Well-Posedness of 2-Cluster Model**

Similar to single cluster section, we want to prove that the 2-cluster model (5.35) has solutions that are non-negative and bounded provided that the initial conditions is non-negative.

COROLLARY 5.10. If the parameter values and the initial condition of 2-cluster model are non-negative, then the solutions of model (5.35) are non-negative and bounded.

PROOF. Similar to the proof of Theorem 5.1, hence the feasible region is given by

$$
\Gamma = \left\{ (S_i, I_i, R_i) \in \mathbb{R}^3_+ \mid S_i + I_i + R_i \leq (\Lambda_1 + \Lambda_2) / (d_1 + \mu_1 + d_2 + \mu_2), i = 1, 2 \right\}
\tag{5.36}
$$

This completes the proof. □

## Analysis of 2-Cluster Model

In this section, we analyzed existence and stability of four different equilibrium solutions:

1. Both clusters are at the disease free equilibrium.
2. Cluster one is at endemic state and cluster two is at the disease free state.
3. Cluster one is at the disease free state and cluster two is at the endemic state.
4. Both clusters are at the endemic state.

### Existence of Disease-Free Equilibrium

At the disease-free equilibrium, we have an absence of the two infection compartments $I_1$ and $I_2$. Thus, the infected compartments will have zero individuals.

THEOREM 5.11. If the parameter values of the 2- cluster model (5.35) are non-negative, then the model will have a unique disease-free equilibrium.

PROOF. We denote DFE with $(\mathrm{S}_1^*, 0, \mathrm{R}_1^*,\ \mathrm{S}_2^*, 0, \mathrm{R}_2^*)$. At equilibrium state, the rate of change of each variable is equal to zero. i.e:

$$S_1' = I_1' = R_1' = S_2' = I_2' = R_2' = 0$$

Hence, by setting the right-hand side of system (5.35) equal to zero, adding the first two equations of the model, and setting $\mathrm{I}_1, \mathrm{I}_2 = 0$ : we got

$$\Lambda_1 + \theta m_{12} S_2 - \theta m_{21} S_1 + \alpha R_1 - (p_1 + d_1) S_1 = 0 \tag{5.37}$$

From the third equation $R_1^*$ of the model (5.35) , we got: $\mathrm{R}_1^* = \frac{p_1 S_1}{(\alpha + d_1)}$. Then, by substituting $\mathrm{R}_1^*$ in (5.37) , we got:

$$S_1^* = \mathrm{a}\left(\Lambda_1 + \theta m_{12} S_2^*\right) \tag{5.38}$$

where $\mathrm{a} = \frac{1}{\theta \mathrm{m}_{21} + \mathrm{p}_1 + \mathrm{d}_1 - \frac{\alpha p_1}{r}}$ , and,

$$R_1^* = \frac{\mathrm{a} p_1 \left(\Lambda_1 + \theta m_{12} S_2^*\right)}{\alpha + d_1} \tag{5.39}$$

By substituting $S_1^*$ in the fourth equation of $S_2^*$ in the model (5.35), we got:

$$S_2^* = \frac{\Lambda_2 + \frac{\Lambda_1 \theta m_{21}}{\theta m_{21} + p_1 + d_1 - \frac{\alpha p_1}{r}}}{\theta m_{12} + p_2 + d_2 - \theta m_{12}\left(\frac{\theta m_{21}}{\theta m_{21} + p_1 + d_1 - \frac{\alpha p_1}{r}}\right)}$$

so,

$$S_2^* = \frac{\Lambda_2 + \mathrm{a}\Lambda_1 \theta m_{21}}{(\theta m_{12} + p_2 + d_2) - \mathrm{a}\theta^2 m_{21} m_{12}} \tag{5.40}$$

and,

$$R_2^* = \frac{p_2 S_2^*}{(\alpha + d_2)} \tag{5.41}$$

It remains to show that $S_2^*$ is always positive. We need to prove $(\theta \mathrm{m}_{12} + p_2 + \mathrm{d}_2) - \mathrm{a}\theta m_{21} \theta \mathrm{m}_{12} > 0$. So, $\theta \mathrm{m}_{12} + p_2 + \mathrm{d}_2 > \mathrm{a}\theta m_{21} \theta \mathrm{m}_{12}$. Divided by $\theta \mathrm{m}_{12}$

$$\Rightarrow \frac{p_2 + \mathrm{d}_2}{\theta \mathrm{m}_{12}} + 1 > \mathrm{a}\theta m_{21}$$

$$\Rightarrow \frac{p_2 + \mathrm{d}_2}{\theta \mathrm{m}_{12}} + 1 > \frac{1}{1 + \frac{\mathrm{P}_1 + \mathrm{d}_1 - \frac{\alpha p_1}{r}}{\theta m_{21}}}$$

Let: $\frac{p_2+\mathrm{d}_2}{\theta \mathrm{m}_{12}} = b, \frac{\mathrm{P}_1+\mathrm{d}_1-\frac{\alpha p_1}{r}}{\theta m_{21}} = c$ Hence, $\mathrm{b}+1 > \frac{1}{1+c} \Rightarrow (\mathrm{b}+1)(\mathrm{c}+1) > 1 \Rightarrow \mathrm{bc}+\mathrm{b}+\mathrm{c}+1 > 1$ So, $bc+b+c > 0$.

Hence, $S_2^*$ is always positive. □

**Basic Reproduction Number $R_0$ for 2-Cluster**

We obtained the basic reproduction number, $R_0$ of the model equations (5.35) which is the spectral radius $\rho$ of the next generation matrix $K$, where, $K = FV^{-1}$

Let $A_1 = \frac{\beta S_1 I_1}{N_1}$, $A_2 = \frac{\beta S_2 I_2}{N_2}$ , $g_1 = \theta m_{12} I_2 - \theta m_{21} I_1 - (\gamma + \mu_1 + \mathrm{d}_1) I_1$, $g_2 = \theta m_{21} I_1 - \theta m_{12} I_2 - (\gamma + \mu_2 + \mathrm{d}_2) I_2$. So,

$$F = \begin{bmatrix} \frac{dA_1}{dI_1} & \frac{dA_1}{dI_2} \\ \frac{dA_2}{dI_1} & \frac{dA_2}{dI_2} \end{bmatrix} = \begin{bmatrix} \frac{\beta S_1^*}{N_1} & 0 \\ 0 & \frac{\beta S_2^*}{N_2} \end{bmatrix} = \begin{bmatrix} \beta_1 & 0 \\ 0 & \beta_2 \end{bmatrix} \tag{5.42}$$

where

$$\beta_1 = \frac{\beta {S^*}_1}{N_1^*}, \beta_2 = \frac{\beta S_2^*}{N_2^*}$$

And,

$$V = -\begin{bmatrix} \frac{dg_1}{dI_1} & \frac{dg_1}{dI_2} \\ \frac{dg_2}{dI_1} & \frac{dg_2}{dI_2} \end{bmatrix} = -\begin{bmatrix} -(\theta m_{21} + \gamma + \mu_1 + \mathrm{d}_1) & \theta m_{12} \\ \theta m_{21} & -(\theta m_{12} + \gamma + \mu_2 + \mathrm{d}_2) \end{bmatrix}$$

Hence,

$$V = \begin{bmatrix} \theta m_{21} + \gamma + \mu_1 + \mathrm{d}_1 & -\theta m_{12} \\ -\theta m_{21} & \theta m_{12} + \gamma + \mu_2 + \mathrm{d}_2 \end{bmatrix} \tag{5.43}$$

Then,

$$FV^{-1} = \begin{bmatrix} \frac{\beta_1\theta m_{12}+\gamma+\mu_2+\mathrm{d}_2}{\det(V)} & \frac{\beta_1\theta m_{12}}{\det(V)} \\ \frac{\beta_2\theta m_{21}}{\det(V)} & \frac{\beta_2\theta m_{21}+\gamma+\mu_1+\mathrm{d}_1}{\det(V)} \end{bmatrix}$$

We have two eigenvalues:

$$\frac{(\beta_2 v_1 + \beta_1 v_2) \pm \sqrt{[(\beta_2 v_1 - \beta_1 v_2)]^2 + 4\theta^2\beta_1\beta_2 m_{12} m_{21}}}{2 \det V}$$

Then, the basic reproduction number $R_0$ of two clusters is,

$$R_0^{[12]} = \frac{(\beta_2 v_1 + \beta_1 v_2) + \sqrt{[(\beta_2 v_1 - \beta_1 v_2)]^2 + 4\theta^2\beta_1\beta_2 m_{12} m_{21}}}{2 \det V} \tag{5.44}$$

Where,

$v_1 = \theta m_{21} + \gamma + \mu_1 + \mathrm{d}_1,$

$v_2 = \theta m_{12} + \gamma + \mu_2 + \mathrm{d}_2,$

$detV = v_1 v_2 - \theta^2 m_{12} m_{21}$

$\beta_1 = \frac{\beta S_1^*}{N_1^*}$, and,

$\beta_2 = \frac{\beta S_2^*}{N_2^*}$

The disease-free equilibrium is globally asymptotically stable if $R_0^{[12]} < 1$, and unstable if $R_0^{[12]} > 1$

REMARK 5.12. From equation (5.44), it can be seen that the $R_0^{[12]}$ expression is

the positive root of a quadratic equation. When there is no movement between the clusters,( i.e $\theta = m_{12} = m_{21} = 0$) , this expression can be reduced to $R_0^{[1]}$ expression in (5.30). When the number of clusters is increased to three, it is expected that the $R_0$ expression will be the greatest positive root of a cubic polynomial. These can be extended to the general n-cluster model. Our attempts to find a recursive formula for $R_0$ expression have not been fruitful. However, we anticipate that search recursive formula can be obtained.

**Existence of Endemic Equilibrium: Cluster 1 at Endemic Equilibrium State, and Cluster 2 at Disease-Free Equilibrium State**

THEOREM 5.13. The endemic equilibrium $EE_1$ has a unique equilibrium at $(S_1^*, I_1^*, R_1^*, S_2^*, 0, R_2^*)$ if $R_0^{[1]} > 1$ and $R_0^{[2]} < 1$.

PROOF. Although the proof of this theorem can be obtained from the Theorem 5.3, we would likely to find $EE_1$. Note that $I_2^* = 0$ because $R_0^{[2]} < 1$ and therefore the DFE at the second cluster is stable. For the disease to persist in the population at cluster 1 , susceptible, infected and recovered compartments cannot be zero, i.e: $EE_1 = (S_1^*, \mathrm{I}_1^*, \mathrm{R}_1^*) \neq (0, 0, 0)$. To find endemic equilibrium for cluster 1, we have to solve the first three equations of the system (5.35) simultaneously taking into consideration the fact that $(S_1^*, I_1^*, R_1^*) \neq (0, 0, 0)$. We know from the equation (5.40) :

$$S_2^* = \frac{\Lambda_2 + \mathrm{a}\Lambda_1\theta m_{21}}{(\theta \mathrm{m}_{12} + p_2 + \mathrm{d}_2) - \mathrm{a}\theta m_{21}\theta \mathrm{m}_{12}} \tag{5.45}$$

From the recovered equation $R_1(t)$, we got:

$$R_1^* = \frac{\gamma I_1^* + p_1 S_1^*}{\alpha + \mathrm{d}_1}$$

By adding the first two equations of the model (5.35), $S_1(t)$ and $I_1(t)$, we got

$$\mathrm{S}_1^* = \frac{\Lambda_1 + \theta \mathrm{m}_{12}\ \mathrm{S}_2^* + \mathrm{cl}_1^*}{\theta \mathrm{m}_{21} + \mathrm{p}_1 + \mathrm{d}_1 - \mathrm{r}\alpha \mathrm{p}_1} \tag{5.46}$$

Where $\mathrm{c} = \mathrm{r}\alpha\gamma - (\theta \mathrm{m}_{21} + \mathrm{p}_1 + \mathrm{d}_1)$, $r = \frac{1}{\alpha + d_1}$

and,

$$I_1^* = \frac{(\theta \mathrm{m}_{21} + \gamma + \mu_1 + \mathrm{d}_1) - f}{g} \tag{5.47}$$

Where $f = \frac{\beta\left(\Lambda_1 + \theta \mathrm{m}_{12} S_2^*\right)}{N_1^*(\theta \mathrm{m}_{21} + \mathrm{p}_1 + \mathrm{d}_1 - \alpha \mathrm{p}_1 r)}$

and,

$$g = \frac{\beta\left(\mathrm{r}\alpha\gamma - (\theta \mathrm{m}_{21} + \gamma + \mu_1 + \mathrm{d}_1)\right)}{\mathrm{N}_1^*\left(\theta \mathrm{m}_{21} + \mathrm{p}_1 + \mathrm{d}_1 - \alpha \mathrm{p}_1 r\right)}$$

□

**Existence of Endemic Equilibrium: Cluster 2 at Endemic Equilibrium State, and Cluster 1 at Disease-Free Equilibrium State**

THEOREM 5.14. The endemic equilibrium $EE_2$ has a unique equilibrium at $(S_1^*, 0, R_1^*, S_2^*, I_2^*, R_2^*)$ if $R_0^{[1]} < 1$ and $R_0^{[2]} > 1$.

PROOF. Although the proof of this theorem can be obtained from the Theorem 5.3, we would likely to find $EE_2$. Note that $I_1^* = 0$ because $R_0^{[1]} < 1$ and therefore the DFE at the first cluster is stable. For the disease to persist in the population at cluster 2, susceptible, infected and recovered compartments cannot be zero, i.e: $EE_2 = (S_2^*, {I_2}^*, {R_2}^*) \neq (0, 0, 0)$. To find endemic equilibrium for cluster 2, we have

to solve the the last three equations of the system (5.35) simultaneously taking into consideration the fact that $(\mathrm{S}_2^*, \mathrm{I}_2^*, \mathrm{R}_2^*) \neq (0,0,0)$ We know that from equation (5.38):

$$S_1^* = a\left(\Lambda_1 + \theta m_{12} S_2^*\right) \tag{5.48}$$

where $\mathrm{a} = \frac{1}{\theta \mathrm{m}_{21} + \mathrm{p}_1 + \mathrm{d}_1 - \frac{\alpha p_1}{r}}$

By adding equations of $S_2(t)$ and $I_2(t)$, we got:

$$\Lambda_2 + \theta m_{21} S_1 - \theta m_{12} S_2 + \alpha R_2 - \left(p_2 + d_2\right) S_2 - \theta m_{12} I_2 - \left(\gamma + \mu_2 + d_2\right) I_2 = 0 \tag{5.49}$$

From equation of $R_2(t)$ , we got:

$$R_2^* = \frac{\gamma I_2^* + p_2 S_2^*}{\alpha + \mathrm{d}_2} \tag{5.50}$$

By substituting $R_2^*$ in equation (5.49), we got:

$$\mathrm{S}_2^* = \frac{\Lambda_2 + \mathrm{a}\Lambda_1 \theta \mathrm{m}_{12} - \mathrm{c}_1 \mathrm{I}_2^*}{\theta \mathrm{m}_{12} + \mathrm{p}_2 + \mathrm{d}_2 - \mathrm{r}_1 \alpha \mathrm{p}_2 - \mathrm{a}\theta^2 m_{21} \mathrm{m}_{12}} \tag{5.51}$$

Where, $r_1 = \frac{1}{\alpha + d_2}, a = \frac{1}{\theta m_{21} + p_1 + d_1 - \frac{\alpha p_1}{r}}$ ,

and, $\mathrm{c}_1 = \mathrm{r}_1 \alpha\gamma - \left(\theta \mathrm{m}_{12} + \gamma + \mu_2 - \mathrm{r}_1 \alpha\gamma\right)$

and,

$$I_2^* = \frac{\theta m_{12} + \gamma + \mu_2 + d_2 - 1}{\beta N_2^* k} \tag{5.52}$$

Where, $\mathrm{k} = \frac{\Lambda_2 + \mathrm{a}\Lambda_1 \theta \mathrm{m}_{12}}{\theta \mathrm{m}_{12} + \mathrm{p}_2 + \mathrm{d}_2 - \mathrm{r}_1 \alpha \mathrm{p}_2 - \mathrm{a}\theta^2 m_{21} \mathrm{m}_{12}}$ □

We observed that when we have two clusters, where cluster 1 is at a disease-free state, and cluster 2 is at an endemic state. We may still have a case where the first

community deals with endemic and new infections because the second community is in an endemic state, and there is human mobility between the two communities. In the next section we can observe different cases of the two clusters.

**Existence of Endemic Equilibrium: Cluster 1 and Cluster 2 at Endemic Equilibrium State**

When both clusters are at the endemic status finding the exact expression for the endemic equilibrium is a highly nontrivial task. However, by applying the Theorem 5.4, it showed that the endemic equilibrium for two clusters exist and stable if and only if $R_0^{[12]} > 1$ , $R_0^{[1]} > 1$, and $R_0^{[2]} > 1$. Hence, we know that we had the following cases:

1. DFE = both clusters are at the disease free equilibrium (i.e $R_0^{[1]} < 1$, and $R_0^{[2]} < 1$) is stable when $R_0^{[12]} < 1$. Hence, the infection will eventually die out by itself.
2. DFE = both clusters are at the disease free equilibrium (i.e $R_0^{[1]} < 1$, and $R_0^{[2]} < 1$) is unstable when $R_0^{[12]} > 1$. In this case, each cluster can not be endemic by their own, but both clusters reach endemic status. Hence, we should limit the human movement between the clusters.
3. $EE_1$= cluster 1 is at endemic state, but cluster 2 is at the disease free equilibrium state. So, $R_0^{[1]} > 1$, $R_0^{[2]} < 1$, and $R_0^{[12]} > 1$. In this case, we need to reduce $R_0^{[1]}$ to less than one. Limiting human movements will not control the infection. We should increase the vaccination rate to reduce $R_0^{[1]}$.
4. $EE_2$ = cluster 2 is at the endemic state, but cluster 1 is at the disease free equilibrium state. So, $R_0^{[2]} > 1$, $R_0^{[1]} < 1$, and $R_0^{[12]} > 1$. In this case, we need

to reduce $R_0^{[2]}$ to less than one. Limiting human movements will not control the infection. We should increase the vaccination rate to reduce $R_0^{[2]}$.

5. $EE_{12}$ = both clusters are at the endemic state. So, $R_0^{[12]} > 1$ , $R_0^{[1]} > 1$, and $R_0^{[2]} > 1$.

**Numerical Verification of Two Clusters**

The first step in the numerical simulations is verifying the theorems related to existence of equilibrium solutions for two cluster model. We have tested the following cases numerically:

1. If $R_0^{[1]} < 1$, $R_0^{[2]} < 1$, and $R_0^{[12]} > 1$, then DFE is unstable, and If $R_0^{[1]} < 1$, $R_0^{[2]} < 1$, and $R_0^{[12]} < 1$, then DFE is stable.
2. If $R_0^{[1]} > 1$, $R_0^{[2]} < 1$, and $R_0^{[12]} > 1$, then $EE_1$ exists, and DFE is unstable.
3. If $R_0^{[2]} > 1$, $R_0^{[1]} < 1$,and $R_0^{[12]} > 1$,then $EE_2$ exists and and DFE is unstable.
4. If $R_0^{[1]} > 1$, $R_0^{[2]} > 1$, and $R_0^{[12]} > 1$, then, $EE_{12}$ exists and it is stable.

The equations of the model (5.35) were solved numerically using the MATLAB ode45 solver which is based on the fourth-order Runge-Kutta method. The stability of the method was well established in [50].

If we consider the set of parameters, $\lambda_1 = 100$, $\beta = 0.5$, $N_1 = 1500$, $\alpha = 0.001$, $p_1 = 0.2$, $d_1 = 0.002$, $\gamma = 0.14$, $\mu_1 = 0.001$, $\lambda_2 = 200$, $N_2 = 1000$, $p_2 = 0.1$, $d_2 = 0.001$, $\mu_2 = 0.023$, $\theta$=1 , $m_{12} = 150$, and $m_{21} = 50$. We noticed from Figure 13.a both clusters are reach the endemic equilibrium state where $R_0^{[1]} = 4.34$, $R_0^{[2]} = 5.67$, and $R_0^{[12]} = 1.0095$. In this case, the infection will persist in the communities and spread out.

In the next case, we tried to control the infection in community 2, so, we increased the vaccination rate in cluster 2 to become $p_2 = 0.8$, and decrease the human movements from community 1 to community 2 to become $m_{21} = 10$. We noticed from Figure 13.b cluster 2 is at disease free equilibrium state where $R_0^{[2]} = 0.60$. However, cluster 1 is at endemic state where $R_0^{[1]} = 3.01$, and $R_0^{[12]} = 1.19$. Even cluster 2 is at disease free equilibrium, there is still a chance to become again at endemic state because of the human movements between the clusters and low vaccination rate in cluster 1.

In the third case, we tried to control the infection in community 1, so, we increased the vaccination rate in cluster 1 to become $p_2 = 0.8$, and decrease the human movements from community 2 to community 1 to become $m_{12} = 100$. We noticed from Figure 13.c cluster 1 is at disease free equilibrium state where $R_0^{[1]} = 0.24$. However, cluster 2 is at endemic state where $R_0^{[2]} = 1.21$, and $R_0^{[12]} = 2.38$. As previous case, despite of cluster 1 is at disease free equilibrium, there is still a chance to become again at endemic state because of the human movements between the clusters and low vaccination rate in cluster 2. which explained that $R_0^{[12]} > 1$ in both previous cases.

Now, let discuss an interesting case, where each cluster can not be endemic by their own (i.e each one of them is at disease free state), but both clusters reach endemic state, where $R_0^{[1]} = 0.06$, $R_0^{[2]} = 0.7954$, and $R_0^{[12]} = 1.42$. In this situation, the disease free state for each cluster is not stable even $R_0^{[1]} < 1$ and $R_0^{[2]} < 1$, and that happened because of $R_0^{[12]} > 1$. As we observed in Figure 14.e, both clusters have infection cases and can not reach the free disease state. To solve this issue, we

restricted the human movements between the two clusters, so, $m_{12} = m_{21} = \theta = 0$. Also, to make sure the infection will not spread out and die out, we increased the vaccination rates in cluster 1 and cluster 2 to become $p_1 = 0.5$ and $p_2 = 0.7$, respectively. We noticed in Figure 14.f both clusters are at stable disease free state where the disease die out, and $R_0^{[1]} = 0.0013$, $R_0^{[2]} = 0.61$, and $R_0^{[12]} = 0.001$.

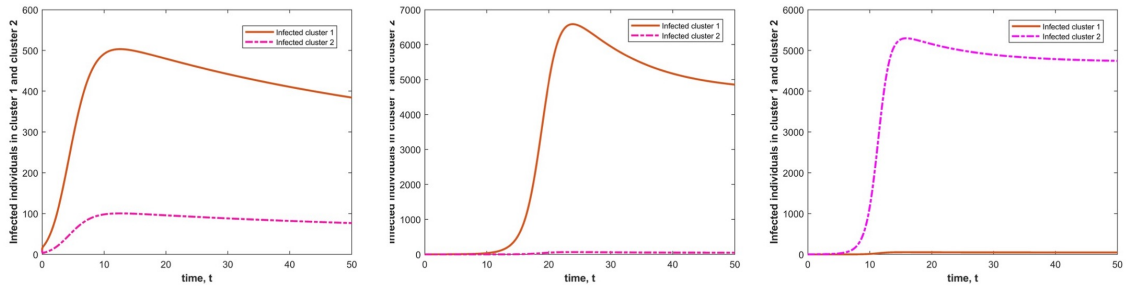


Figure 13: (a) Case 1: Both clusters are at the endemic state. (b) Case 2: Cluster 1 is at endemic state, but cluster 2 is at the disease free equilibrium state. (C) Case 3: Cluster 2 is at endemic state, but cluster 1 is at the disease free equilibrium state.

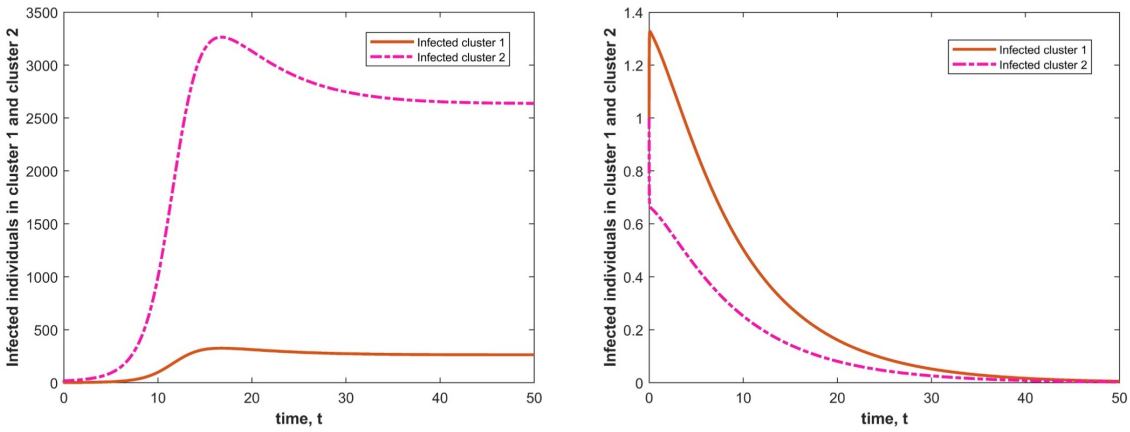


Figure 14: (d) Case 4: Both clusters are at the disease free equilibrium, but its unstable. (e) Case 5: Both clusters are at the disease free equilibrium, but its stable.

**Numerical Simulation**

We carried out numerical simulations of the model (5.35) to assess the impact of human behaviors, beliefs and control measures on spreading the disease in the communities. If we consider the set of parameters, $\lambda_1 = 100$, $\beta = 0.8$, $N_1 = 1500$, $\alpha = 0.001$, $p_1 = 0.5$, $d_1 = 0.002$, $\gamma = 0.14$, $\mu_1 = 0.001$, $\lambda_2 = 200$, $N_2 = 1000$, $p_2 = 0.4$, $d_2 = 0.001$, $\mu_2 = 0.023$, $\theta$=1 , $m_{12} = 100$, and $m_{21} = 50$.

We have the following four cases:

1. The first case is when the first community has a vaccination rate of 50% and the second community has a vaccination rate of 40% at the beginning of the pandemic. We want to observe the effect of human behaviors and beliefs on both communities if they act irresponsibly and stop taking the vaccine. We can observe in Figure 15.A both communities have seen an increase in cases of the new infection. However, community 1 has more infection cases even with a higher vaccination rate. That happened because the human movement from community 2 to community 1 is higher than from community 1 to community 2.
2. In the second case, we want to observe the effect of human mobility on spreading the disease. In this case, we ignored the effect of movements from cluster 2 to cluster 1, so, $\theta = m_{12} = 0$. As we can see in Figure 15.B, cluster 1 is at disease-free equilibrium state where the disease died out, and cluster 2 is at endemic equilibrium state, where the disease is persist in the community. Therefore, control measures such as travel restrictions, isolation, and quarantine may limit the spread of the disease, specifically in the early stages of an

outbreak when it is confined to a particular local area that acts as a major hotspot. However, human mobility restrictions may be less effective once the outbreak is more widespread.

3. The third case is the inequities of vaccination rates. In this case, the second community vaccination rate was increased from 40% to 90%, while the first community has the same vaccination rate. We noticed that in Figure 15.C, even we have high vaccination rate in the second community, it is still having endemic and dealing with lots of new infections cases because the first community has low vaccination rate. Inequities in vaccination rates across communities will negatively impact all communities.
4. The last case when the vaccine immunity is waning and its effect decrease with time. As we can see in Figure 15.D, there is an increase in infected cases after 15 months of taking the vaccine. Different studies showed that the immunity against the disease substantially decreased after six months of receiving the second dose of the COVID-19 vaccine [151]. Despite the immunity against COVID-19 decreased with the time, the first two doses of the vaccination are effective in preventing severe illness, hospitalization, and death [152].

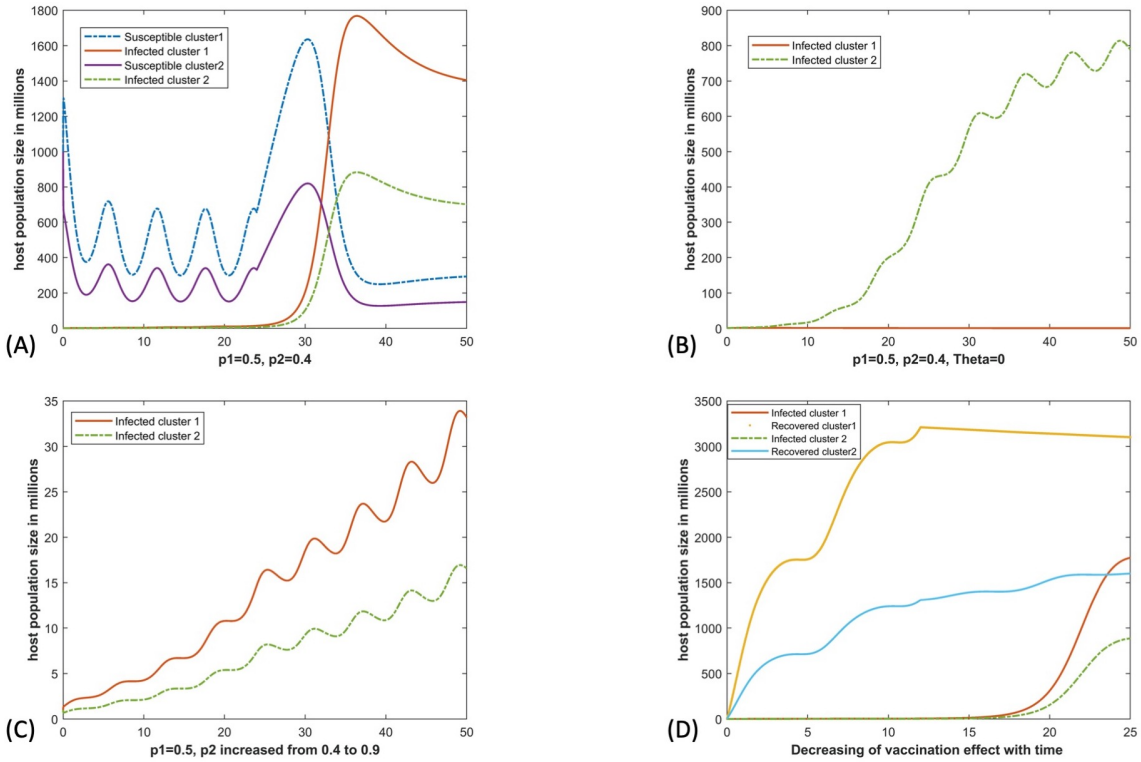


Figure 15: (A) Case 1: The impact of stop vaccinate two populations after had vaccination rate as $p_1 = 0.5$ and $p_1 = 0.4$. (B) Case 2: The impact of human mobility between two communities. (C) Case 3: The impact of inequities of vaccination rates. (D) Case 4: The impact of decreasing the effectiveness of the vaccine with time.

## 5.6 Discussion and Conclusions

In this chapter, we proposed mathematical model of COVID-19 transmission in clusters environment that are connected through human mobility. We analyzed the model (5.1) mathematically by studying the positivity and boundedness of the model solutions, the local and global stability of the disease-free equilibrium of n-clusters. Also, we proved the uniqueness of the disease free equilibrium and the endemic equilibrium. Moreover, we studied mathematically two different cases of spatial transmission of individuals traveling between 2-clusters, and single cluster and derived $R_0$ for each case. Also, we studied mathematically and numerically the existence and stability of four different equilibrium solutions:

1. Cluster 1 and cluster 2 are at the disease-free state.
2. Cluster one (or two) is at endemic state but cluster two (or one) is at the disease-free state.
3. Cluster 1 and cluster 2 are at the endemic state.

We observed that to control the spread of the infection between the communities, we had to limit human movements and increase the vaccination rates.

To monitor the impact of control measures and prevention on spreading the disease in the communities, we studied four cases of human behaviors, beliefs, and vaccination rates on spreading COVID-19 in the communities. In the first case, we observed the need of establishing health communication strategies that effectively convince the individuals to vaccinate against COVID-19. Increasing the awareness receiving the vaccine will help to control the spread of COVID-19 in the communities. Despite of the effective of vaccinating, many individuals are refusing the COVID-19

immunization for different reasons. For instance, several studies have found that one-fifth to one-third of Americans do not intend to vaccinate, and many more are undecided [150].

In fact, an effective vaccination may help protect communities in two ways: direct protection (vaccinating high-risk individuals to prevent disease) and indirect protection (vaccinating those in contact with high-risk people to reduce transmission). Therefore, developing health communication strategies that effectively encourage individuals to vaccinate against COVID-19 might have significant public health implications.

In the second case we showed that restricting human movement may be advantageous, particularly in the early phases of an outbreak when it is restricted to a specific small location that serves as the primary hotspot. For instance, In Wuhan, China, human mobility was associated with the high transmission of SARS-CoV-2, and social distancing policies and isolation effectively controlled the epidemic [154]. In Malaysia, the substantial spread of COVID-19 cases was linked to a religious gathering held without adhering to the social distancing recommendation [156]. Because of that, stricter lockdown measures were enforced around the world to combat rising infection cases such as shutdown orders, traveling restriction, quarantine, school closures and working remotely. However, human mobility restrictions may be less effective once the outbreak is more widespread. Therefore, a combination of control measures such as travel restrictions and vaccination can mitigate the spread of the disease and reduce local transmission of COVID-19.

In the third case, we noticed that the inequities in vaccination rates across communities would negatively impact the communities. Inequities in vaccination rates

across communities are likely the result of several causes, including unequal access to health care information and services, low-income, and medical racism. Moreover, poor countries face challenges because of a lack of vaccines for their population. For instance, according to the World Health Organization, only 3 % of Africa's population was fully vaccinated [153]. Low vaccination rates cause the development of new variants that can be more transmissible. Therefore, vaccinating unvaccinated people and reducing vaccination inequities should be prioritized. if the vaccination coverage in low-income countries remains insufficient, SARS-CoV-2 may develop into different variants that are more suited to circumventing natural and vaccine-induced immunity, putting other communities with high vaccination rates at risk [153].

In the last case, we showed that the effectiveness of the vaccine decreased with time. However, the COVID-19 vaccines are expected to be effective at preventing severe illness, hospitalization, and death in case the individuals get infected [91]. Because of widespread immunization, the coronavirus will infect fewer people. This will limit the virus's ability to propagate among communities and determine the virus's ability to evolve into new variants [87].

# CHAPTER 6
# INCORPORATING GLOBAL DYNAMICS TO IMPROVE THE ACCURACY OF SIR MODEL

## 6.1 Overview

Mathematical models of infectious diseases exhibit robust dynamics, such as stable endemic, disease-free equilibriums or convergence of the solutions to periodic epidemic waves. In the present chapter, we showed that such dynamics can be significantly improved by incorporating local and global infection dynamics into disease models. To demonstrate improved accuracy, we extended a standard Susceptible-Infected-Recovered (SIR) model by incorporating the global dynamics of the COVID-19 pandemic. The extended SIR model assumes three possibilities for susceptible individuals traveling outside of their community:

- They can return to the community without any exposure to the infection.
- They can be exposed and develop symptoms after returning to the community.
- They can be tested positively during the trip and remain quarantined until fully recovered.

To examine the predictive accuracy of the extended SIR model, we studied the prevalence of the COVID-19 infection in six randomly selected cities and states influenced by the COVID-19 global pandemic: Kansas City, Saint Louis, San Francisco, Missouri, Illinois, and Arizona. The extended SIR model was parameterized using a two-step model-fitting algorithm. The extended SIR model significantly outperformed the

standard SIR model and revealed oscillatory behaviors with an increasing trend of infected individuals.

This chapter has been published in PLOS One Journal [85].

## 6.2 Introduction

One of the simplest, yet powerful, disease models is the standard Susceptible-Infected-Recovered (SIR) model, which was first introduced by Kermack and McKendrick in a series of three papers [40, 41, 42]. In a standard SIR model, the host population is divided into susceptible, infected and recovered individuals, denoted by $S(t)$, $I(t)$ and $R(t)$, respectively. These quantities track the numbers of individuals in each compartment over different time periods [27, 60]. The standard SIR model without birth and death is represented by the set of ordinary differential equations [35].

$$\begin{aligned} \frac{dS}{dt}(t) &= -\beta S(t)I(t) \\ \frac{dI}{dt}(t) &= \beta S(t)I(t) - \gamma I(t) \\ \frac{dR}{dt}(t) &= \gamma I(t) \end{aligned} \tag{6.1}$$

Where $\beta$ is the average number of susceptible individuals infected by one infectious individual per contact per unit of time (the transmission rate), and $\gamma$ is the average number of infected individuals recovered per unit of time (recovery rate).

For decades, the standard SIR model in equation (6.1) has been extended to various forms by adding different compartments to suit the biological, spatio-temporal and social aspects of the disease dynamics or to study the impact of intervention

strategies on the disease transmission dynamics in different communities [30, 43]. For instance, the standard SIR has been extended to SIR models with diffusion [32], contaminated environment [33, 34], delay terms [67], several strains of infection [20], and multiple routes of infection [19].

Recently, several researchers utilized mathematical modeling to analyze, and predict the transmission dynamics of COVID-19 pandemic [38, 44, 63]. Dynamics of COVID-19 epidemic has been simulated using different versions of SIR or SEIR (susceptible, exposed, infected and recovered) models [38, 44]. The main modification include adding asymptomatic and symptomatic infection compartments [63], hospitalization compartment [18], and quarantined and isolated compartments [38]. These models are presumably able to predict and simulate the number of infected cases by taking into consideration the asymptomatic and symptomatic cases, deaths, needs of beds in hospitals, and effect of control measures and the interventions to decrease the number of cases.

The abovementioned extended SIR models contribute to the existing literature. However, they largely ignore the effects of global dynamics of infection on local communities. The presence of a global pandemic or a widespread infection can largely influence the dynamics of infection in a local community. Most communities are well-connected and the assumption that the disease exists only within the community is invalid [69].There have been attempts to include the global dynamics in different SIR models [48, 67]. Nevertheless, such extended SIR models have several unknown parameters and poorly fit to data of host population. Due to lack flexibility and poor fitness to data, there is a need for develop SIR models that are more practical.

Moreover, regardless of the parameter values, most numerical simulations of SIR models are limited to three distinct dynamics. The first of these dynamics is the solution curve of infected individuals may exhibit an epidemic wave before converging to a disease-free equilibrium [46], secondly, the solution curve of infected converge to an endemic equilibrium [62], the third of these dynamics is the solution curve of infected converge to periodic epidemic waves [52]. For the standard SIR model (6.1), the dynamics are even more limited. Namely, the solution curves always represent the same qualitative dynamics: an epidemic wave of the infectious population, an inverted S shape for susceptible population, and S shape for the recovered population. Regardless of the set of parameter values and initial conditions, such qualitative behaviors will always remain the same (see panels Figure 16A- Figure 16C ). A quick review of the number of individuals infected with COVID-19, at the country [53] , state [66], or community level [49] , shows that the dynamics of COVID-19 is more complicated than a single epidemic wave.

The present chapter aims to address this issue. We extended the SIR model to a new model that includes the global impacts of the infection and is also capable of fitting well to infectious disease data. To incorporate the global effect and test the predictive accuracies of the extended model, we selected randomly six cities and states influenced by the COVID-19 global pandemic: Kansas City, Saint Louis, San Francisco, Missouri, Illinois, and Arizona.

We assumed three possibilities to consider in the SIR modeling of COVID-19: Susceptible individuals from a local community can travel in and out of their community without any exposure to COVID-19, they can be exposed to COVID-

19 while traveling and develop symptoms after they return to their community, or they can be diagnosed with COVID-19 during their traveling and return to their community after recovery.

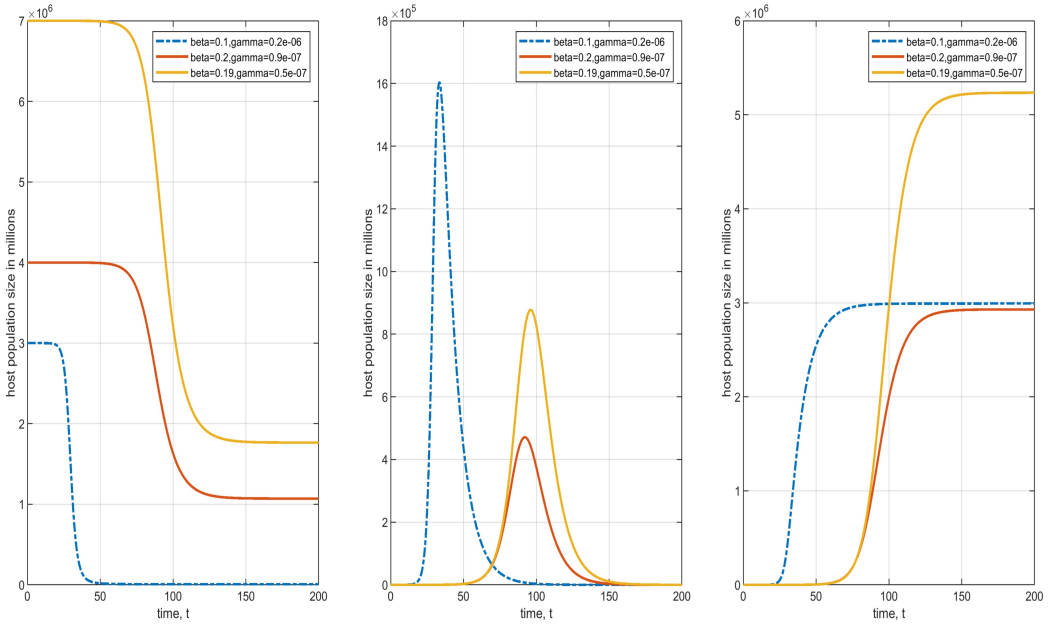


Figure 16: Qualitative behavior of the standard SIR model remains the same regardless of the parameter values ($\beta$ and $\gamma$).
From left to right : (A) An inverted S-shape occurs for the susceptible population.
(B) A bell-shaped epidemic wave of infected population.
(C) A S-shaped curve of a recovered population.

## 6.3 Materials and Methods

### COVID-19 Data

The COVID-19 data used in this study were obtained from the Health Department of Kansas City, Saint Louis, San Francisco, Missouri, Illinois, and Arizona [28, 29, 68, 73]. The data were dated from March 10, 2020 to March 7, 2021 (a total of 363 days). We did not include data after March 7, 2021 because our model does not include the effects of vaccination and it would be inappropriate to include the data thereafter. Specifically, the data variables consisted of date, total number of cases, new cases, total deaths, new deaths and total number of individuals tested for COVID-19. We used abovementioned data to extract the daily number of susceptible, infected, and recovered individuals (see Appendix A for the algorithm used for generating the data).

Table 12 provides the basic descriptive statistics of Kansas City, Saint Louis, San Francisco, Missouri, Illinois, and Arizona of daily COVID-19 data of infected individuals. Observe that the statistics of susceptible and recovered data are comparable (see Tables A5 to A10 in Appendix A for the basic descriptive statistics). However, the statistics of infected individuals are at a much lower scale.

To estimate the number of susceptible individuals, we assumed an average incubation period of 5 days for COVID-19 [59]. We also considered one day for obtaining the COVID-19 test results. Hence, all of those who were tested positive were susceptible from the beginning until 6 days prior to obtaining the test results. Also, we added the individual who take the test, but their results were negative. These individuals had presumably high risk of getting infected and therefore susceptible.

The number of infected individuals were calculated by considering an average infection period 14 days [55]. Hence, we cumulatively added of new cases for 14 days until they recovered.

Table 12: Descriptive Statistics of Kansas City (KC), Saint Louis (SL), San Francisco (SF), Missouri (MO), Illinois (IL), and Arizona (AZ) daily COVID-19 data from March 10, 2020 to March 7, 2021

.

| Measures | Infected in KC | Infected in SL | Infected in SF | Infected in MO | Infected in IL | Infected in AZ |
|---|---|---|---|---|---|---|
| Minimum | 1 | 1 | 2 | 0 | 0 | 0 |
| Maximum | 4109 | 2201 | 4600 | 62456 | 168855 | 129240 |
| Mean | 1413.140 | 772.60 | 1305.50 | 18395.38 | 45387.31 | 31215.03 |
| Median | 1280 | 549 | 917 | 15793 | 27896 | 16242 |
| Range | 4108 | 2200 | 4598 | 62456 | 168855 | 129240 |
| Standard Deviation | 1137.49 | 565.87 | 1141.94 | 16777.20 | 42645.57 | 33702.66 |

## Model Formulation

We divided our population of N individuals living in a local community into sup-populations (i.e., compartments) of susceptible compartment $S(t)$, infected compartment $I(t)$, and recovered compartment $R(t)$. As shown in Figure 17, the extended SIR model of COVID-19 transmission assumed three possibilities for susceptible individuals traveling outside of the community: They can return to the community without any exposure (the net rate is $f(t) = f_2(t) - f_1(t)$), they can be exposed COVID-19 and develop symptoms after returning to the community (the inflow rate

of $g(t)$), or they can be tested positive during their trip and remain quarantined until fully recovered and thereafter return to the community (the inflow rate of $h(t)$). Then, the extended SIR model is formulated by the following system of deterministic non-linear differential equations while Figure 17 gives the flow diagram of the model.

$$\begin{aligned}
\frac{dS}{dt}(t) &= -\beta S(t)I(t) + f(t) \\
\frac{dI}{dt}(t) &= \beta S(t)I(t) - \gamma I(t) + g(t) \\
\frac{dR}{dt}(t) &= \gamma I(t) + h(t)
\end{aligned} \tag{6.2}$$

where $\beta$ and $\gamma$ are the same parameters as in system (6.1). Functions $f(t)$, $g(t)$, and $h(t)$ are differentiable and bounded and take into account the global effects of the infection. To avoid overfitting, our goal is to estimate $f$, $g$, and $h$ and using least complicated forms.

Although adding exposed population can provide interesting dynamics, we decided to exclude the exposed compartment from our modeling. This is due to lack of data associated with exposed population. Namely, there is no known method of accurately identify the time series of exposed population in a community. In addition, the more compartments are added the harder it becomes to accurately estimate the parameter values.

In some cases, the confidence intervals of estimated parameter values become extremely large due to high number of parameters and insufficient amount of data. With this rationale in mind, we therefore employed a two-step method to estimate the parameters of the model.

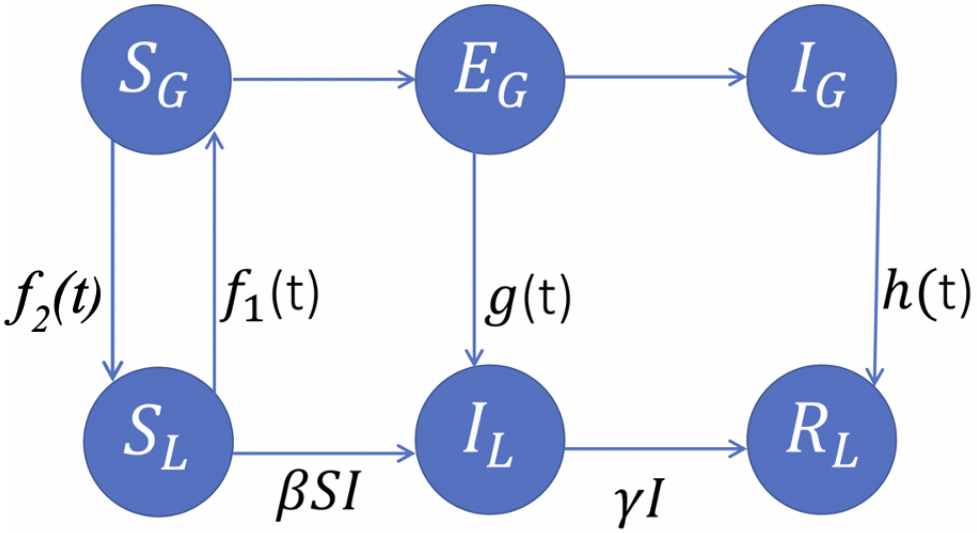


Figure 17: A schematic representation of the extended SIR model coupled with a global SEI model. L and G correspond to the number of individuals in the local and global communities, respectively.

**Model Fitting**

The single-step numerical methods such as linearization and discretization [56] to estimate the parameter values of model (6.2) fail to converge, due to high degrees of freedom and unknown intervals of parameter estimations. We therefore proposed a two-step process for parameters estimation of model (6.2). We first estimated the parameter values of the standard SIR model (6.1) and then we determined the functions $f(t)$, $g(t)$ and $h(t)$ using the residual data of $S(t)$, $I(t)$ and $R(t)$ subpopulations. As mentioned before, we used the COVID-19 data of susceptible, infected and recovered individuals in Kansas City, Saint Louis, San Francisco, Missouri, Illinois, and Arizona for an epidemic period starting from March 10, 2020 to March 7, 2021.

In the first step, we numerically solved the system (6.2) using the MATLAB ode45 solver which is based on the fourth order Runge-Kutta method. The stability of the method is well established in [50]. For data fitting, the optimization function *fmincon* was used along with the common technique of the least-squares method [22, 64]. This method minimizes the sum of the squared residuals, that is, the difference between model predictions and their corresponding data values. The sum of the squared residuals is calculated using the formula below:

$$E = \frac{1}{M}\sum_{I=1}^{M}(y - y_i)^2 \tag{6.3}$$

where M represents the total number of data points considered for fitting and $y$ and $y_i$ represent the values predicted by the model and those from the data, respectively.

We estimated the SIR parameter values by considering the following factors. Several studies indicated that the COVID-19 transmission rate of infection was 0.5 [23, 25]. Hence, we set $\beta = 0.5$. Also, some studies assumed the average recovery period (i.e $\frac{1}{\gamma}$) is about 7 days [23, 25], which results in the initial value of $\gamma = 0.13$. Also, to be consistent with the data, we set our initial conditions to the number of susceptible, infected and recovered at t=1. The estimated model parameters are provided in Table 13.

In the second step, we fitted the global effect of infection on the community by estimating functions $f(t)$, $g(t)$ and $h(t)$ in model (6.2). Although model selection can be done using Akaike's Information Criteria (AIC) and Bayesian Information Criteria (BIC) methods, we used the MATLAB curve fitting toolbox to measure the goodness of fit (adjusted $R^2$, sum of the squared residuals, etc.) to find the optimal

forms of functions $f(t)$, $g(t)$ and $h(t)$. Specifically, the model fitting resulted in the following forms:

$$f(t) = \lambda_1 t + \lambda_2$$

$$g(t) = a_1 b_1 \cos(b_1 T + c_1) + a_2 b_2 \cos(b_2 T + c_2) + a_3 b_3 \cos(b_3 T + c_3) \tag{6.4}$$

$$h(t) = p_1 t + p_2$$

## 6.4 Results

Using the COVID-19 data, we estimated the functions corresponding to the global effects $f(t), g(t)$ and $h(t)$ in model (6.2) using the above-mentioned two steps in Kansas City, Saint Louis, San Francisco, Missouri, Illinois, and Arizona. The estimated net rate for the susceptible individual who can return to the community without any exposure was given by $f(t) = \lambda_1 t + \lambda_2$. The estimated net rate of the individual who exposed to the infection and develop symptoms after returning to the community was given by $g(t) = a_1 b_1 \cos(b_1 T + c_1) + a_2 b_2 \cos(b_2 T + c_2) + a_3 b_3 \cos(b_3 T + c_3)$, and the estimated net rate of the individual who tested positive during their trip and remain quarantined until fully recovered and thereafter return to the community was given by $h(t) = p_1 t + p_2$.

All parameter estimations of step 1 and step 2 are summarized in Table 13 and Table 14, respectively. From Table 13, we noticed that the transmission rate in the states; Missouri, Illinois, and Arizona were much higher than the cities; Kansas City, Saint Louis, and San Francisco, which was due to the larger population size of states and cities. Note that the estimated values for recovery rates were different than those

of the standard SIR model because of the recovery rate was influenced by the global effects. In Table 14, there are three parameters, $a$, $b$ and $c$ where $a$ represents the amplitude of each wave for each city or state, $b$ represents the frequency of each wave, and $c$ represents the phase shift of each wave. Also, the values of $T$ represents the period of each wave. For instance, for the state of Missouri and the city of Kansas City had almost the same of three periodic epidemic waves of COVID-19. One happens every two years , the other wave happens every four months and half, and the last one every nine months. The periodic waves could be associated with several factors such as, traveling, major social events, infection prevention policies, changes to the coronavirus itself, and the increase of people who become susceptible because they have not developed some immunity [72].

Table 13: Estimated parameter values of model (6.2) based on data of Kansas City, Saint Louis, San Francisco, Missouri, Illinois, and Arizona

| Parameter | Description | KC | SL | SF | MO | IL | AZ |
|---|---|---|---|---|---|---|---|
| $\lambda_1$ | Linear recruitment rate | 100 | 99.9997 | 71.42 | -20 | 600 | -20 |
| $\lambda_2$ | Constant recruitment rate | -0.2481 | -0.3278 | -0.0809 | -1.32 | 8.62 | -10 |
| $\beta$ | Transmission rate | $2.9 \times 10^{-16}$ | $5.49 \times 10^{-4}$ | $4.9 \times 10^{-4}$ | 8.23 | 8.22 | 3.998 |
| $\gamma$ | Recovery rate* | $7.3 \times 10^{-15}$ | 0.1275 | $1.97 \times 10^{-9}$ | 1.003 | 1.002 | 0.59 |
| $p_1$ | Linear flow of recovered | 0.633 | 0.288 | 0.553 | 10.2 | 23.92 | 14.92 |
| $p_2$ | Constant flow of recovered | -8.01 | 2.876 | -15.17 | -477.6 | -1190 | -729.9 |

* The estimated values for the recovery rates are different than those of the standard SIR model.

Table 14: Parameters of global effects functions in Infected model based on data of Kansas City, Saint Louis, San Francisco, Missouri, Illinois, and Arizona.

| Parameter | KC | SL | SF | MO | IL | AZ |
|---|---|---|---|---|---|---|
| $a_1$ | 2412 | 5763 | 1929 | $3.28 \times 10^4$ | $8.69 \times 10^4$ | $6.65 \times 10^4$ |
| $b_1$ | 0.009 | 0.0149 | 0.005 | 0.009 | 0.0051 | 0.0142 |
| $c_1$ | 2.548 | 1.75 | 2.94 | 2.43 | 2.794 | 2.008 |
| $T1 = 2\pi/b1$ | 698 | 421.5 | 1256 | 698 | 1231.4 | 442.2 |
| $a_2$ | 609.1 | 416.6 | $1.41 \times 10^4$ | 7048 | $3.85 \times 10^4$ | $3.007 \times 10^4$ |
| $b_2$ | 0.046 | 0.05 | 0.037 | 0.048 | 0.031 | 0.027 |
| $c_2$ | -1.81 | 3.58 | -4.875 | 3.88 | -3.53 | -2.812 |
| $T2 = 2\pi/b2$ | 136.5 | 125.6 | 169.7 | 130.8 | 202.6 | 232.6 |
| $a_3$ | 826.1 | 5072 | $1.42 \times 10^4$ | $1.3 \times 10^4$ | $2.03 \times 10^4$ | $2.7 \times 10^5$ |
| $b_3$ | 0.025 | 0.017 | 0.037 | 0.025 | 0.048 | 0.029 |
| $c_3$ | 3.64 | -1.70 | 4.48 | -2.4 | -2.47 | 0.138 |
| $T2 = 2\pi/b2$ | 251.2 | 369.4 | 169.7 | 251.2 | 130.8 | 216.5 |

The panel of Fig 18.A - Fig 18.F shows that the extended SIR model of the susceptible solution curve fits well to the data of susceptible subpopulation in the cities and states. Likewise, Table A11 in Appendix A, shows the goodness of fit of susceptible subpopulation for Kansas City, Saint Louis, San Francisco, Missouri, Illinois, and Arizona data where $R^2 = 0.9909, 0.9911, 0.9802, 0.9878, 0.9761, 0.9583$, respectively. Similarly, Fig 19.A - Fig 19.F shows the extended SIR model in the

subpopulations of recovered individuals fits well to the data and have a goodness of fit $R^2 = 0.9873, 0.9893, 0.9804, 0.9844, 0.9748, 0.9606$, respectively (See Table A11 in Appendix A).

Fig 20.A - Fig 20.F shows that the dynamics of COVID-19 in the cities and states were more complicated than a single epidemic wave as common in the standard SIR model. The extended model is capable of revealing the underlying behaviors hidden in the data. Also, the extended SIR model in the subpopulations of infected individuals fits well to the data and have goodness of fit $R^2 = 0.9542, 0.9287, 0.962, 0.9438, 0.9015, 0.9492$ for Kansas City, Saint Louis, San Francisco, Missouri, Illinois, and Arizona data, respectively. (See Table A11 in Appendix A). Therefore, the inclusion of global effects to the SIR model can substantially improve the predictive accuracy of the model.

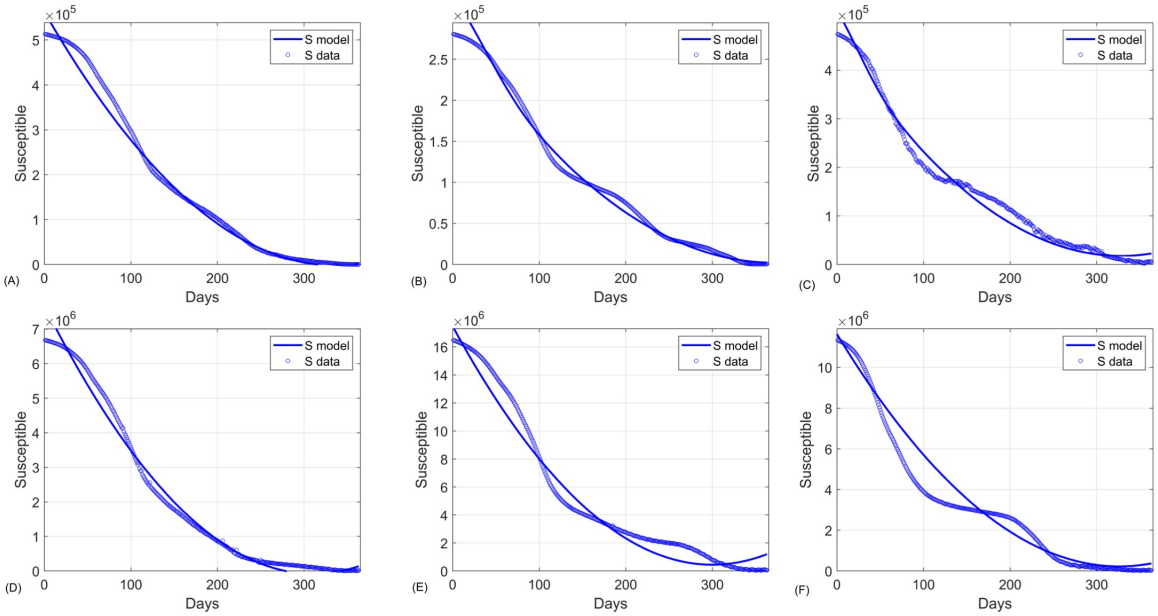


Figure 18: The extended SIR model fitted to the COVID-19 data of susceptible subpopulation in (A) Kansas City, (B) Saint Louis, (C) San Francisco, (D) Missouri, (E) Illinois, and (F) Arizona.

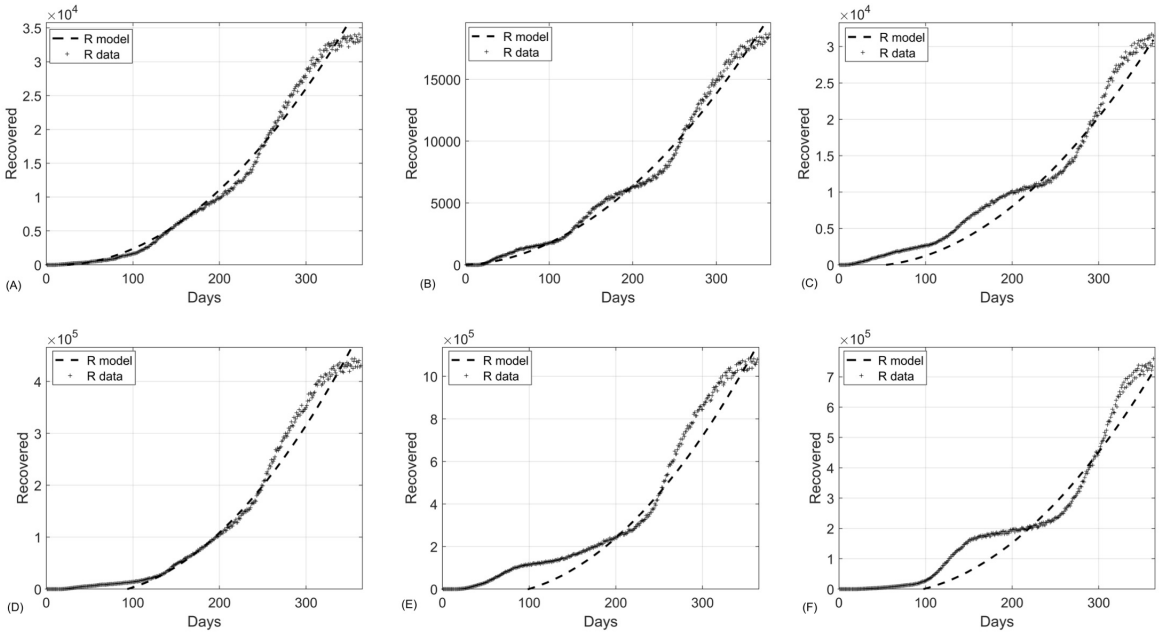


Figure 19: The extended SIR model fitted to the COVID-19 data of recovered subpopulation in (A) Kansas City, (B) Saint Louis, (C) San Francisco, (D) Missouri, (E) Illinois, and (F) Arizona.

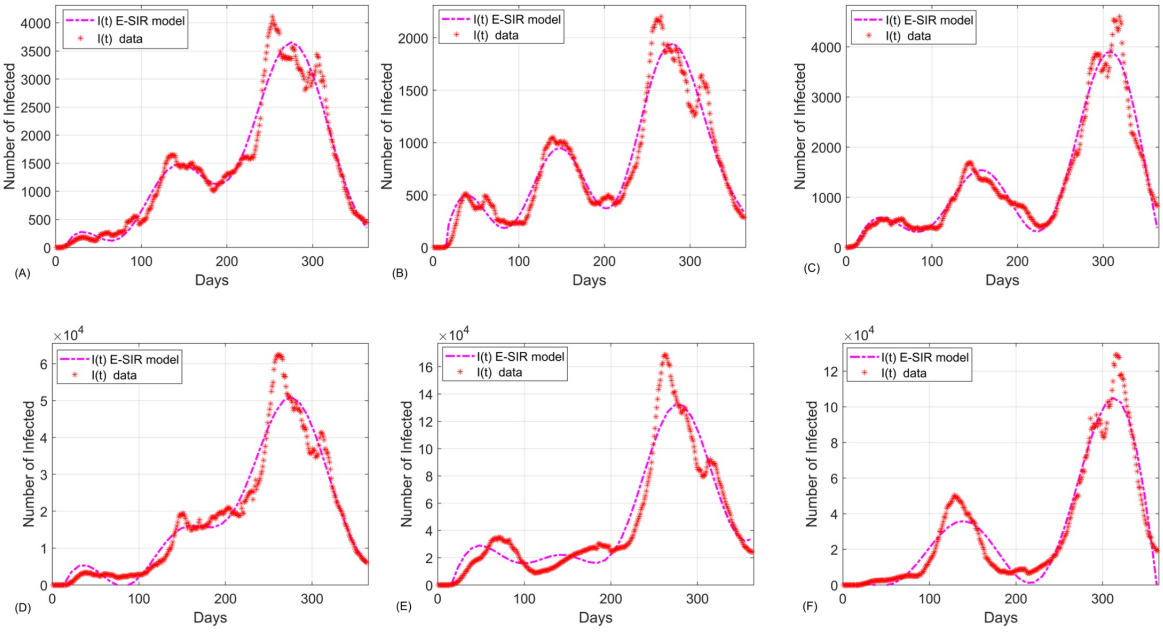


Figure 20: The extended SIR model fitted to the COVID-19 data of infected subpopulation in (A) Kansas City, (B) Saint Louis, (C) San Francisco, (D) Missouri, (E) Illinois, and (F) Arizona.

## 6.5 Discussion and Conclusions

The present chapter highlights the importance of including global dynamics of infection in disease models to achieve higher predictive accuracies. We introduced a two-step algorithm for accurate estimation of infection parameters by considering both global and local effects of the infection spread in a disease model. The first step leads to estimation of local parameters (i.e., the transmission and recovery rates, $\beta$ and $\gamma$ , respectively) whereas the second step incorporates the global effects of the infection (i.e., estimation of functions $f(t)$, $g(t)$ and $h(t)$). To test the methodology, we applied the two-step model fitting algorithm to the extended SIR model (6.2) using Kansas City, Saint Louis, San Francisco, Missouri, Illinois, and Arizona data from March 10, 2020 to March 7, 2021. As shown in the panel of Fig 18, Fig 19, and Fig 20, the two-step method resulted in solution curves that fit well to the COVID-19 data. The goodness of fit becomes more apparent when it is compared to that of the standard SIR model (6.1). Therefore, we compared the standard SIR model with the extended SIR model using the first 212 Kansas City COVID-19 data. As shown in Fig 21a and Fig 21b, the solution curves of the standard SIR model poorly fit to the COVID-19. Moreover, Table 15 shows the comparisons of model fitness for the standard and extended SIR model. The extended SIR model of the susceptible solution curve has $R^2 = 0.9905$ while in standard model $R^2 = 0.1551$. Similarly the extended SIR model outperformed the standard SIR model in the subpopulations of recovered individuals ($R2 = 0.9912$ versus $R^2 = 0.47$), and the subpopulation of infected individuals ($R^2 = 0.7083$ versus $R^2 = -258.65$). Note that the negative $R^2$ value is because the classical SIR model did not follow the trend of the data.

In addition to higher predictive accuracies of the extended SIR model (6.2), the solution curves revealed oscillatory behaviors with an increasing trend of infected individuals. This contrasts with the standard SIR model, where regardless of chosen parameter values, the solution curves always exhibit the same qualitative behaviors (see Figure 16A- Figure 16C).

Although the standard SIR has been proven beneficial for studying the local dynamics of various infections, it fails to capture the global effects of widespread disease. The failure of standard SIR model to forecast the COVID-19 pandemic can be described by a variety of factors. One of these factors is that the standard SIR model assumes the population is closed and isolated, and ignored the effects of the global dynamics of infection on neighboring communities, which is not a valid assumption [69]. Hence, by including the global infection effects in the disease models, we can identify underlying mechanisms governing the dynamics of infectious diseases.

In spite of several studies indicate that include temperature factor in the SIR model could potentially improve the model outcomes [70], recent studies suggested that the temperature has no influence on the propagation of the COVID-19 virus [71, 74]. In fact, some strains of the virus alter depending on their environment. They may live and grow in a variety of geographical areas or temperatures. Outside of laboratory tests, there is no way to anticipate how the virus would react in heat and humidity or even cold and dry temperatures.

The inability of the standard SIR model to fit the COVID-19 data has been identified by other researchers [45]. Nonetheless, the presence of a breakpoint due to strong policy interventions, as mentioned in [45], does not necessarily reduce the

prevalence of infection in a community dealing with a pandemic. In conclusion, Including the global dynamics of the infection and applying the two-step model fitting algorithm can enable us to extract vital information (e.g., presence of epidemic waves) from the data.

Table 15: Comparisons of model fitness for the standard and extended SIR models

| Fitness | Extended | Standard |
|---|---|---|
| Corrected AIC | $3.28 \times 10^3$ | $4.31 \times 10^3$ |
| AIC | $3.04 \times 10^3$ | $4.07 \times 10^3$ |
| SSR ($R^2$) for S | $3.22 \times 10^9$ (0.9905) | $5.04 \times 10^8$ (0.1551) |
| SSR ($R^2$) for I | $4.12 \times 10^5$ (0.7083) | $-1.51 \times 10^8$ ($-258.65$)* |
| SSR ($R^2$) for R | $3.51 \times 10^9$ (0.9912) | $1.66 \times 10^9$ (0.4700) |

* The standard SIR model has an extremely poor fitting with respect to the infected individuals.

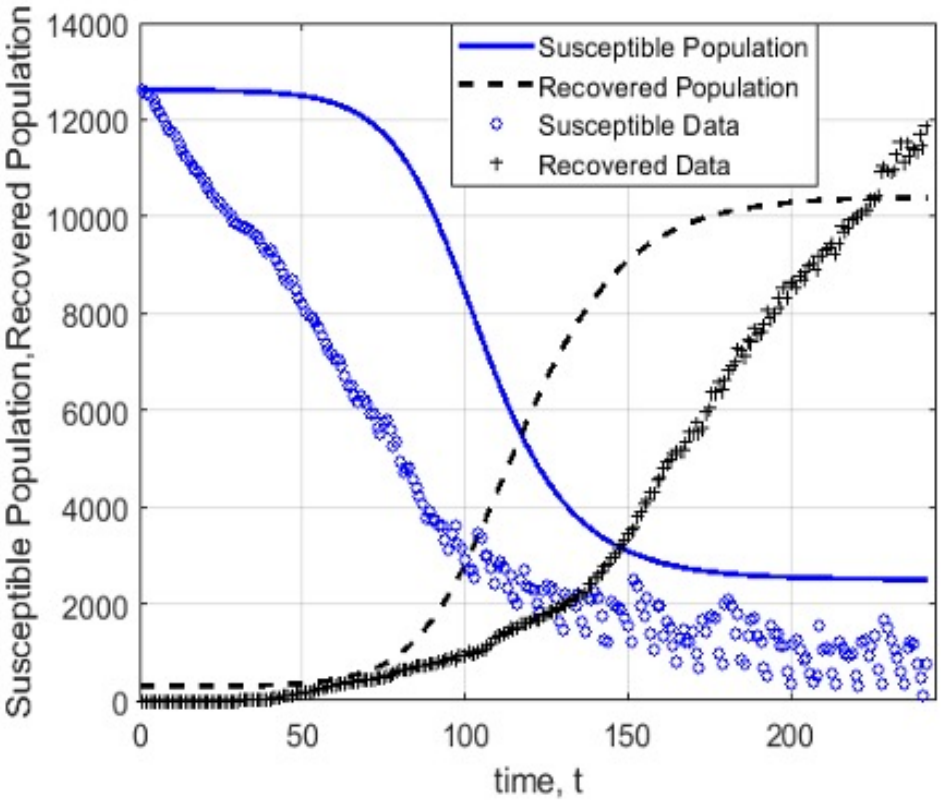


(a) The standard SIR model poorly fits to the susceptible and recovered data in Kansas City, Missouri.

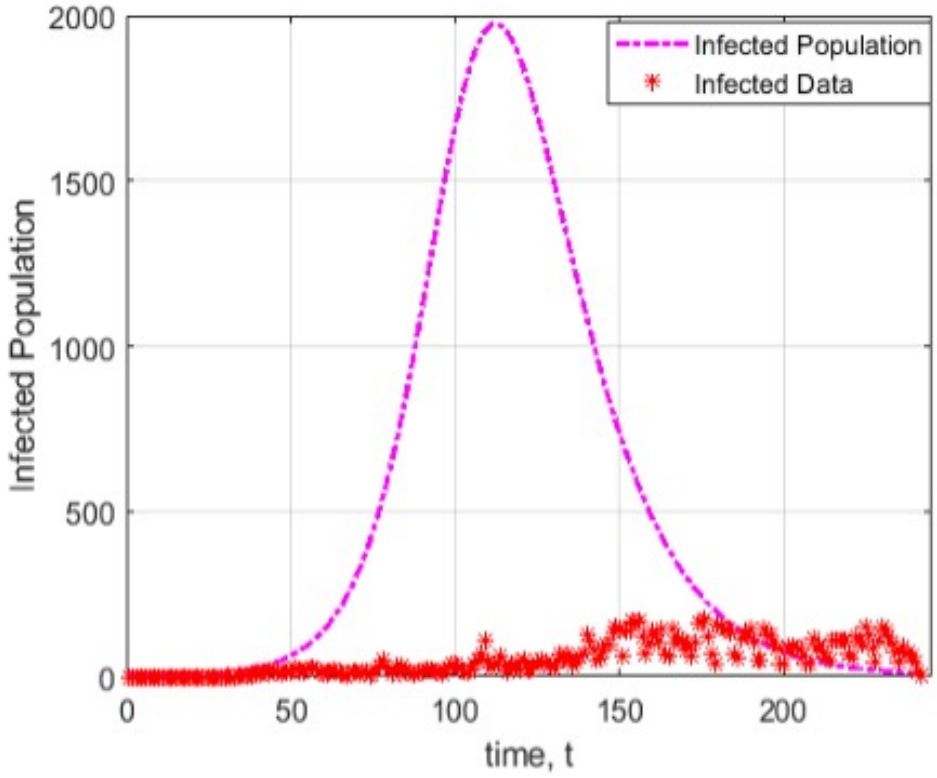


(b) The standard SIR model poorly fits to the infected data in Kansas City, Missouri.

Figure 21: The standard SIR model fitted to COVID-19 data.

# CHAPTER 7

# PERIODIC WAVES OF COVID-19 EMERGED FROM HOPF BIFURCATION

## 7.1 Overview

Periodic and oscillatory behaviors of COVID-19 infection have been observed in different regions of the world [142, 143, 144]. While there are several underlying factors resulting in oscillatory behaviors of the number of COVID-19 infected individuals, there is a need to distinguish between these factors. Particularly, are oscillations due to seasonal variations in the temperature? [143, 145]. Are they related to seasonal changes in the movements of individuals such as school opening, traveling during the summer, or holidays? [146]. Or, is it an intrinsic nature of the COVID-19 infection? For instance, it has been shown that COVID-19 transmissibility changes from one variant to another. Several SARS-CoV-2 variants have been detected across the world [87]. In the United States, the Centers for Disease Control and Prevention (CDC) has identified four variations of concern: Alpha, Beta, Gamma, and Delta. The World Health Organization (WHO) recently found a new concerning variation known as Omicron. According to the organization, these varieties appear to spread more easily and fast. Each variety evolved individually, and they all have unique mutations and mutations in common [161].

The main purpose of this chapter is to use the mathematical theory of Hopf bifurcation to test the main hypothesis that the presence of COVID-19 oscillations can be due to its intrinsic nature. Note that we will not rule out the other factors,

such as spatial movements of individuals or changes to the ambient temperature. To test if the model exhibits Hopf bifurcation, we built a mathematical model of COVID-19. The significance of this result lies in the fact that periodic waves of COVID-19 can be emerged by host-pathogen dynamics of COVID-19. Hence, periodic solutions can be generated by factors other than seasonality or anthropogenic activities such as traveling, school opening, and increased economic activities.

In addition, we analyzed the model mathematically by studying the local stability of the disease-free equilibrium and endemic equilibrium. Also, we derived the basic reproduction number $R_0$ using the method of the Next Generation Matrix (NGM). Moreover, we tested if the model meets the conditions of Hopf bifurcation to understand the dynamics of the disease at the occurrence of a second wave and the kind of treatment measures needed to curtail it. Using Hopf bifurcation and its numerical simulations illustrated that the severity of a COVID-19 outbreak can be directly influenced by the rates of infected individuals.

## 7.2 Model Formulation

In the attempt to create a mathematical model of COVID-19 for a local community, we made certain assumptions based on the characteristics of COVID-19 and the epidemiological state of the individuals.

- The susceptible individuals became exposed and got infected when the individuals have not developed some immunity, whether from natural infection or through vaccination. Otherwise,the susceptible individuals move to recovered compartment.
- The infected compartment was divided into three classes depending on the symptoms' development:
    1. The first infected class for individuals with asymptomatic infection. The infected people with asymptomatic infections will recover without needing medical care.
    2. The second infected class is for individual with unreported or undocumented infection. Because of the shortage in testing kite especially early on in the course of the pandemic, hospitals and disease control centers were only able to test the subsample of people with severe symptoms or travel history. Therefore, unreported infections may go unrecognized because they often experience mild symptoms which they can infect a large proportion of the population.
    3. The third infected class is for individual with reported infection. Infected individuals in one of these two classes have one of the disease stages. First, they have a mild disease requiring medical care such as medicine,

and then they recover. The second stage is when they have a severe disease that needs specific medical care, such as ventilators, and then they may recover or die.

- The number of vaccinated population was negligible. For instance, Pfizer is 95% effective, Moderna is 94.1% effective, and Johnson & Johnson is 72% effective in preventing COVID-19 [91].
- Isolated individuals were immune to the infection (ex: students and teachers who are switching to online platform).

Based on these assumptions, we proposed the following COVID-19 mathematical model to study the dynamics of COVID-19:

$$
\begin{aligned}
\frac{dS}{dt}(t) &= (1-P)\Lambda - S(t)(\beta_A I_A(t) + \beta_U I_U(t) + \beta_R I_R(t) + \mu_n).\\
\frac{dE}{dt}(t) &= S(t)(\beta_A I_A(t) + \beta_U I_U(t) + \beta_R I_R(t)) - (\gamma + \mu_n)E(t).\\
\frac{dI_A}{dt}(t) &= p_A\gamma E(t) - (\eta_A + \mu_n)I_A(t),\\
\frac{dI_U}{dt}(t) &= p_U\gamma E(t) - (\alpha_U + \eta_U + \mu_n)I_U(t).\\
\frac{dI_R}{dt}(t) &= p_R\gamma E(t) - (\alpha_R + \eta_R + \mu_n)I_R(t).\\
\frac{dM_D}{dt}(t) &= \eta_U I_U(t) + \eta_R I_R(t) - (\sigma_M + \eta_M + \mu_n)M_D(t).\\
\frac{dS_D}{dt}(t) &= \alpha_U I_U(t) + \alpha_R I_R(t) - (\sigma_S + \alpha_S + \mu_s + \mu_n)S_D(t).\\
\frac{dR}{dt}(t) &= \eta_A I_A(t) + (\sigma_M + \eta_M)M_D(t) + (\sigma_S + \alpha_S)S_D(t) + P\Lambda - \mu_n R(t).
\end{aligned}
\tag{7.1}
$$

with the total population being:

$$N(t) = S(t) + E(t) + I_A(t) + I_U(t) + I_R(t) + M_D(t) + S_D(t) + R(t)$$

Given the above-mentioned assumptions and the set of ordinary differential equations representing the model (7.1), a compartmental diagram of the proposed COVID-19 model is seen in Figure 22, and a summary of parameters and variables is given in Table 16 .

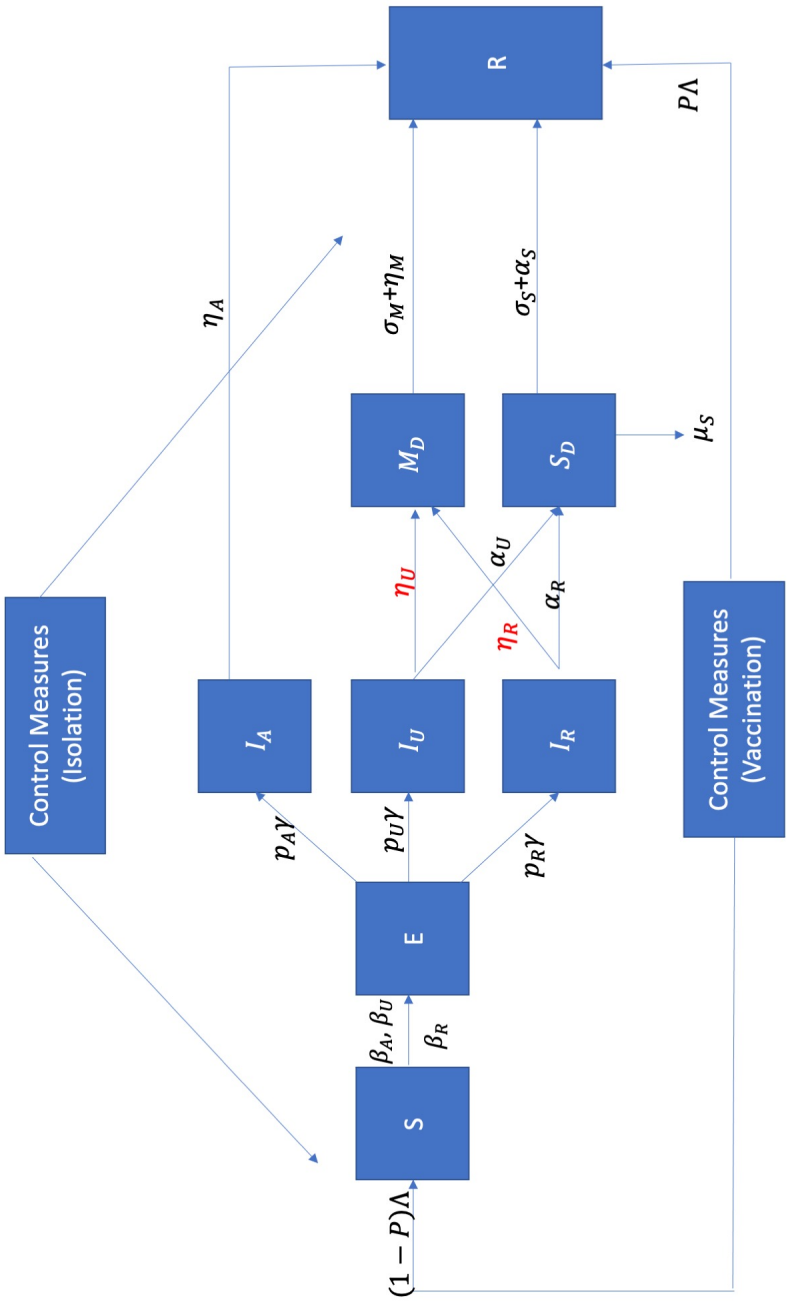


Figure 22: A compartmental diagram of the COVID-19 model 7.1 of asymptomatic, undocumented, and reported infection with control measures. See Table 16 for a summary of the parameters and variables.

Table 16: Summary of the variables and parameters used in the COVID-19 model

| Symbol | Description |
|---|---|
| S(t) | Number of susceptible individual at time t |
| E(t) | Number of exposed individual at time t |
| $I_A(t)$ | Number of asymptomatic infected individual at time t |
| $I_U(t)$ | Number of unreported infected individual at time t |
| $I_R(t)$ | Number of reported infected individual at time t |
| $M_D(t)$ | Number of individual has mild disease at time t |
| $S_D(t)$ | Number of individual has severe disease at time t |
| R(t) | Number of recovered individual |
| $\beta_A$, $\beta_U$, $\beta_R$ | Transmission rate of the disease |
| $\gamma$ | Transition rate from exposed compartment to infected compartment |
| $p_A$ | The proportion of asymptomatic infection. |
| $p_U$ | The proportion of unreported infection |
| $p_R$ | The proportion of reported infection |
| $\eta_A$ | The proportion of recovered infections of asymptomatic infection |
| $\eta_U$ | The proportion of unreported infected progress to mild disease |
| $\eta_R$ | The proportion of reported infected progress to mild disease |
| $\alpha_U$ | The proportion of unreported infected will progress to severe disease |
| $\alpha_R$ | The proportion of reported infected will progress to severe disease |
| $\eta_A$ | The proportion of recovered infections of asymptomatic infection |
| $\sigma_M + \eta_M$ | The proportion of mild disease translate to recovered compartment |
| $\sigma_s + \eta_s$ | The proportion of severe disease translate to recovered compartment |
| $\eta_A$ | The proportion of recovered infections of asymptomatic infection |
| $\mu_s$ | The mortality rate |
| $\mu_n$ | The death rate |
| $\Lambda$ | recruitment rate |
| P | vaccination rate |

## 7.3 Positivity and Boundness of the Model

The first step for validating COVID-19 model is to ensure that all solutions with non-negative initial conditions remain bounded and non-negative.

THEOREM 7.1. The solutions to all subpopulation ($S(t)$, $E(t)$, $I_A(t)$, $I_U(t)$, $I_R(t)$, $M_D(t)$, $S_D(t)$, and $R(t)$) in the model (7.1) are non-negative for all time $t \geq 0$ given any finite non-negative initial conditions of $S(0) \geq 0, E(0) \geq 0, I_A(0) \geq 0$, $I_U(0) \geq 0, I_R(0) \geq 0$, $M_D(0) \geq 0$, and $S_D(0) \geq 0$.

PROOF. All the subpopulations defined by the model (7.1) are continuously differentiable. As such, if all subpopulations have non-negative initial conditions, and that if any of the subpopulations is zero at time $t = t_i \geq 0$, its derivative is non-negative by inspection. Let assume $S(0) \geq 0$, $S(t_1) = 0$ at time instant $t = t_1$ then, we can rewrite $S(t)$ using (7.1),

$\frac{dS(t_1)}{dt} = (1-P)\Lambda \geq 0$, hence $S(t)$ is non-negative for all time $t \geq 0$. Next, let assume $E(0) \geq 0$, $E(t_2) = 0$, $S(t_2) \geq 0$, $I_A(t) \geq 0$, $I_U(t) \geq 0$ and $I_R(t) \geq 0$ at time instant $t = t_2$, we can rewrite $E(t)$ using (7.1),

$\frac{dE(t_2)}{dt} = S(t_2)(\beta_A I_A(t_2) + \beta_U I_U(t_2) + \beta_R I_R(t_2)) \geq 0$, hence $E(t)$ is nonnegative for all time $t \geq 0$.

Next, let assume $I_A(0) \geq 0$, $I_A(t_3) = 0$, and $E(t_3) \geq 0$ at time instant $t = t_3$ ,we can rewrite $I_A(t)$ using (7.1),

$\frac{dI_A(t_3)}{dt} = p_A \gamma E(t_3) \geq 0$, hence $I_A(t)$ is nonnegative for all time $t \geq 0$.

Now, let assume $I_U(0) \geq 0$, $I_U(t_4) = 0$, and $E(t_4) \geq 0$ at time instant $t = t_4$ ,we can rewrite $I_U(t)$ using (7.1),

$\frac{dI_U(t_4)}{dt} = p_U\gamma E(t_4) \geq 0$, hence $I_U(t)$ is nonnegative for all time $t \geq 0$.

Next, let assume $I_R(0) \geq 0$, $I_R(t_5) = 0$, and $E(t_5) \geq 0$ at time instant $t = t_5$, we can rewrite $I_R(t)$ using (7.1),

$\frac{dI_R(t_5)}{dt} = p_R\gamma E(t_5) \geq 0$, hence $I_R(t)$ is nonnegative for all time $t \geq 0$.

Assume $M_D(0) \geq 0$, $M_D(t_6) = 0$, and $I_U(t_6)$, $I_R(t_6) \geq 0$ at time instant $t = t_6$ ,$M_D(t)$ using (7.1) becomes:

$\frac{dM_D(t_6)}{dt} = \eta_U I_U(t_6) + \eta_R I_R(t_6) \geq 0$, hence $M_D(t)$ is nonnegative for all time $t \geq 0$.

Assume $S_D(0) \geq 0$, $S_D(t_7) = 0$, and $I_U(t_7)$, $I_R(t_7) \geq 0$ at time instant $t = t_7$ ,$S_D(t)$ using (7.1) becomes:

$\frac{dS_D(t_7)}{dt} = \alpha_U I_U(t_7) + \alpha_R I_R(t_7) \geq 0$ , hence $S_D(t)$ is nonnegative for all time $t \geq 0$.

Lastly, $R(0) \geq 0$, $R(t_8) = 0$, and $M_D(t_8)$, $S_D(t_8) \geq 0$ at time instant $t = t_8$,$R(t)$ using (7.1) becomes:

$\frac{dR(t_8)}{dt} = (\sigma_M + \eta_M)M_D(t_8)(\sigma_S + \alpha_S)S_D(t_8) + P\Lambda \geq 0$, hence $R(t)$ is nonnegative for all time $t \geq 0$.

Hence, the all model solutions with non-negative initials are non-negative. □

THEOREM 7.2. The total population $N(t)$ is finitely upper-bounded for any non-negative initial conditions

PROOF. The total population of the system (7.1) can be written as the following:

$$\frac{dN(t)}{dt} = \frac{dS(t)}{dt} + \frac{dE(t)}{dt} + \frac{dI_A(t)}{dt} + \frac{dI_U(t)}{dt} + \frac{dI_R(t)}{dt} + \frac{dM_D(t)}{dt} + \frac{dS_D(t)}{dt} + \frac{dR(t)}{dt}$$

$$= \Lambda - \mu_n(S(t) + E(t) + I_A(t) + I_U(t) + I_A R(t) + M_D(t) + S_D(t) + R(t)$$

since Theorem 7.1 has established that all subpopulations are non-negative and given that all parameters are assumed to be positive, then $\frac{dN(t)}{dt}$ becomes:

$$\frac{dN(t)}{dt} \approx \Lambda - \mu_n(N(t)) \tag{7.2}$$

We can then deduce that

$$\frac{dN(t)}{dt} \leq \Lambda - \mu_n(N(t)) \tag{7.3}$$

where an integration of the inequality (7.3) yields

$$N(t) \leq N(0)e^{-\mu_n t} + \frac{\Lambda}{\mu_n}(1 - e^{-\mu_n t}) \leq Max(N(0), \frac{\Lambda}{\mu_n})$$

for all time $t \geq 0$. Hence, the total population N(t) is finitely upper-bounded. Therefore, the biologically feasible is that:

$$\begin{aligned} \Omega = \{(S, E, I_A, I_U, I_R, M_D, S_D, R) \in \mathbb{R} : 0 \leq S(t) + E(t) + I_A(t) + \\ I_U(t) + I_R(t) + M_D(t) + S_D(t) + R(t) \leq \frac{\Lambda}{\mu_n}\}. \end{aligned} \tag{7.4}$$

□

## 7.4 Analysis of COVID-19 Model

### Existence of Disease-Free Equilibrium

The disease free equilibrium state is the state where the disease die out which means the absence of the infection. Thus, all infected compartments will be zero except susceptible and recovered compartments.

THEOREM 7.3. If the parameter values of the model (7.1) are non-negative, then

the model will have a unique disease-free equilibrium that exists at the point

$$(S^*, 0, 0, 0, 0, 0, 0, R^*).$$

PROOF. We denote DFE with $(S^*, 0, 0, 0, 0, 0, 0, R^*)$. At the disease- free state, the rate of change of each variable is equal to zero. i.e:

$$S' = E' = I'_A = I'_U = I_A = M'_D = S'_D = R' = 0$$

Hence, by setting the right-hand side of system (7.1) equal to zero :

$$\frac{dS}{dt}(t) = (1-P)\Lambda - S(t)(\beta_A I_A(t) + \beta_U I_U(t) + \beta_R I_R(t) + \mu_n) = 0$$

$$\frac{dE}{dt}(t) = S(t)(\beta_A I_A(t) + \beta_U I_U(t) + \beta_R I_R(t)) - (\gamma + \mu_n)E(t) = 0$$

$$\frac{dI_A}{dt}(t) = p_A\gamma E(t) - (\eta_A + \mu_n)I_A(t) = 0$$

$$\frac{dI_U}{dt}(t) = p_U\gamma E(t) - (\alpha_U + \eta_U + \mu_n)I_U(t) = 0$$

$$\frac{dI_R}{dt}(t) = p_R\gamma E(t) - (\alpha_R + \eta_R + \mu_n)I_R(t) = 0$$

$$\frac{dM_D}{dt}(t) = \eta_U I_U(t) + \eta_R I_R(t) - (\sigma_M + \eta_M + \mu_n)M_D(t) = 0$$

$$\frac{dS_D}{dt}(t) = \alpha_U I_U(t) + \alpha_R I_R(t) - (\sigma_S + \alpha_S + \mu_s + \mu_n)S_D(t) = 0$$

$$\frac{dR}{dt}(t) = \eta_A I_A(t) + (\sigma_M + \eta_M)M_D(t) + (\sigma_S + \alpha_S)S_D(t) + P\Lambda - \mu_n R(t) = 0$$

The disease-free equilibrium is given by:

$$DFE = (\frac{(1-P)\Lambda}{\mu_n}, 0, 0, 0, 0, 0, 0, \frac{P\Lambda}{\mu_n}). \tag{7.5}$$

□

**Basic Reproduction Number $R_0$**

As we defined $R_0$ in Chapter 5, $R_0$ is the expected number of secondary infections produced by a single case of an infection introduced to a completely susceptible population.

COVID-19 model (7.1) has more infected compartments, hence, the Jacobian method is hard to apply as it relies on the algebraic Routh-Hurwitz conditions for stability of the Jacobian matrix. Therefore, we used the Next Generation Matrix (NGM) [20, 149]. Specifically, the next generation matrix is given by $K = FV^{-1}$.

We introduced two matrices, the first matrix, denoted $F$, containing infection terms and the second matrix, $V$, containing the transfer terms. The eigenvalues of the total new infections matrix (i.e, eigenvalues of $FV^{-1}$) are calculated. The basic reproduction number, therefore, is the largest of these eigenvalues. Mathematically, this can be summarized as follows:
$F = [\frac{\partial F_i(x_0)}{\partial x_j}]$, and $V = [\frac{\partial V_i(x_0)}{\partial x_j}]$ , where $F_i$ represents the new infections, $V_i$ represents the transfer terms, and the value $x_0$ represents the disease-free equilibrium. The basic reproduction number, $R_0$, is the spectral radius given by $\rho(FV^{-1})$.

Now, The Jacobian matrix evaluated at disease-free equilibrium

$$(S^*, E^*, I_A^*, I_U^*, I_R^*, M_D^*, S_D^*, R^*) = (\frac{(1-P)\Lambda}{\mu_n}, 0, 0, 0, 0, 0, 0, \frac{P\Lambda}{\mu_n})$$

is given by

$$J_{DFE} = \begin{pmatrix} -\mu_n & 0 & -\frac{\beta_A\Lambda(1-P)}{\mu_n} & -\frac{\beta_U\Lambda(1-P)}{\mu_n} & -\frac{\beta_R\Lambda(1-P)}{5}\mu_n & 0 & 0 & 0 \\ 0 & -(\gamma+\mu_n) & \frac{\beta_A\Lambda(1-P)}{\mu_n} & \frac{\beta_U\Lambda(1-P)}{\mu_n} & \frac{\beta_R\Lambda(1-P)}{\mu_n} & 0 & 0 & 0 \\ 0 & p_A\gamma & -(\eta_A+\mu_n) & 0 & 0 & 0 & 0 & 0 \\ 0 & p_U\gamma & 0 & -(\alpha_U+\eta_U+\mu_n) & 0 & 0 & 0 & 0 \\ 0 & p_R\gamma & 0 & 0 & -(\alpha_R+\eta_R+\mu_n) & 0 & 0 & 0 \\ 0 & 0 & 0 & \eta_U & \eta_R & -(\sigma_M+\eta_M+\mu_n) & 0 & 0 \\ 0 & 0 & 0 & \alpha_U & \alpha_R & 0 & -(\sigma_S+\alpha_S+\mu_s+\mu_n) & 0 \\ 0 & 0 & \eta_A & 0 & 0 & (\sigma_M+\eta_M) & (\sigma_S+\alpha_S) & -\mu_n \end{pmatrix}$$

Using the next generation matrix, it is clear that the reproduction number $R_0$ is the spectral radius of the next generation matrix derived from the exposed and infected class. Thus,

$$F = \begin{pmatrix} 0 & \frac{\beta_A\Lambda(1-P)}{\mu_n} & \frac{\beta_U\Lambda(1-P)}{\mu_n} & \frac{\beta_R\Lambda(1-P)}{\mu_n} & 0 & 0 \\ 0 & 0 & 0 & 0 & 0 & 0 \\ 0 & 0 & 0 & 0 & 0 & 0 \\ 0 & 0 & 0 & 0 & 0 & 0 \\ 0 & 0 & 0 & 0 & 0 & 0 \\ 0 & 0 & 0 & 0 & 0 & 0 \end{pmatrix} \tag{7.6}$$

and,

$$V = \begin{pmatrix} \gamma+\mu_n & 0 & 0 & 0 & 0 & 0 \\ -p_A\gamma & \eta_A+\mu_n & 0 & 0 & 0 & 0 \\ -p_U\gamma & 0 & \alpha_U+\eta_U+\mu_n & 0 & 0 & 0 \\ -p_R\gamma & 0 & 0 & \alpha_R+\eta_R+\mu_n & 0 & 0 \\ 0 & 0 & -\eta_U & -\eta_R & \sigma_M+\eta_M+\mu_n & 0 \\ 0 & 0 & -\alpha_U & -\alpha_R & 0 & \sigma_S+\alpha_S+\mu_s+\mu_n \end{pmatrix} \tag{7.7}$$

so,

$$K = FV^{-1} = \begin{pmatrix} C(\frac{p_A\beta_A}{\eta_A+\mu_n} + \frac{p_U\beta_U}{\alpha_U+\eta_U+\mu_n} + \frac{p_R\beta_R}{\alpha_R+\eta_R+\mu_n}) & \frac{(1-P)\Lambda\beta_A}{\mu_n(\eta_A+\mu_n)} & \frac{(1-P)\Lambda\beta_U}{\mu_n(\alpha_U+\eta_U+\mu_n)} & \frac{(1-P)\Lambda\beta_R}{\mu_n(\alpha_R+\eta_R+\mu_n)} & 0 & 0 \\ 0 & 0 & 0 & 0 & 0 & 0 \\ 0 & 0 & 0 & 0 & 0 & 0 \\ 0 & 0 & 0 & 0 & 0 & 0 \\ 0 & 0 & 0 & 0 & 0 & 0 \\ 0 & 0 & 0 & 0 & 0 & 0 \end{pmatrix} \tag{7.8}$$

Where,

$$C = \frac{\gamma\Lambda(1-P)}{\mu_n(\gamma+\mu_n)}$$

So, the matrix (7.8) is the is the next generation matrix of the system (7.1).

Thus, the basic reproductive number is given as

$$R_0 = \rho(K) = C(\frac{p_A\beta_A}{\eta_A+\mu_n} + \frac{p_U\beta_U}{\alpha_U+\eta_U+\mu_n} + \frac{p_R\beta_R}{\alpha_R+\eta_R+\mu_n}). \tag{7.9}$$

Where, $C = \frac{\gamma\Lambda(1-P)}{\mu_n(\gamma+\mu_n)}$.

We observed that the reproduction number $R_0$ is associated with the transmission rate of the disease $\beta_A$,$\beta_U$, and $\beta_R$ and with the vaccination rate $P$.

THEOREM 7.4. The rate of reduction in $R_0$ with respect to $P$ is larger than the reduction rate with respect to $\beta_A$, $\beta_U$, and $\beta_R$.

PROOF. let assume $\beta_A = \beta_U = \beta_R = \beta$. Provided that:

$$Q_1 = \frac{\partial R_0}{\partial P}, Q_2 = \frac{\partial R_0}{\partial \beta}$$

Which $Q_1$ is the derivative of $R_0$ with respect to vaccination rate, and $Q_2$ is the derivative of $R_0$ with respect to transmission rate.

Then,

$$Q_1 = \frac{\partial R_0}{\partial P} = \frac{-\gamma\Lambda}{\mu_n(\gamma+\mu_n)}\left(\frac{p_A\beta_A}{\eta_A+\mu_n} + \frac{p_U\beta_U}{\alpha_U+\eta_U+\mu_n} + \frac{p_R\beta_R}{\alpha_R+\eta_R+\mu_n}\right). \tag{7.10}$$

And,

$$Q_2 = \frac{\partial R_0}{\partial \beta} = \frac{-\gamma\Lambda(1-P)}{\mu_n(\gamma+\mu_n)}\left(\frac{p_A}{\eta_A+\mu_n} + \frac{p_U}{\alpha_U+\eta_U+\mu_n} + \frac{p_R}{\alpha_R+\eta_R+\mu_n}\right). \tag{7.11}$$

Hence,

$$\frac{Q_1}{Q_2} = \frac{\frac{-\gamma\Lambda}{\mu_n(\gamma+\mu_n)}\left(\frac{p_A\beta_A}{\eta_A+\mu_n} + \frac{p_U\beta_U}{\alpha_U+\eta_U+\mu_n} + \frac{p_R\beta_R}{\alpha_R+\eta_R+\mu_n}\right)}{\frac{-\gamma\Lambda(1-P)}{\mu_n(\gamma+\mu_n)}\left(\frac{p_A}{\eta_A+\mu_n} + \frac{p_U}{\alpha_U+\eta_U+\mu_n} + \frac{p_R}{\alpha_R+\eta_R+\mu_n}\right)} = \frac{\beta_A+\beta_U+\beta_R}{(1-P)}$$

So, the rate of reduction in $R_0$ with respect to $P$ is larger than the reduction rate with respect to $\beta_A$, $\beta_U$, and $\beta_R$ if $3\beta > 1-P$. □

**Existence of Endemic Equilibrium**

The endemic equilibrium state is the state where the disease can not be totally die out, but it persist in the population. For the disease to be persist, all the model compartments must not be zero at endemic equilibrium point, i.e.:

$$(S^*, E^*, I_A^*, I_U^*, I_R^*, M_D^*, S_D^*, R^*) \neq (0,0,0,0,0,0,0,0)$$

In order to obtain endemic equilibrium point, we have to solve equations of the model (7.1) simultaneously taking into consideration the fact that $(S^*, E^*, I_A^*, I_U^*, I_R^*, M_D^*, S_D^*, R^*) \neq (0,0,0,0,0,0,0,0)$.

THEOREM 7.5. An unique endemic equilibrium of the model (7.1) exists at the point $(S^*, E^*, I_A^*, I_U^*, I_R^*, M_D^*, S_D^*, R^*)$.

PROOF. First, we need to show that $S^*, I_A^*, I_U^*, I_R^*, M_D^*, S_D^*$, and $R^*$ can be written based on the number of exposed individuals $E^*$, by solve the equations of the system (7.1) simultaneously.

From $\frac{dI_A}{dt}(t) = p_A\gamma E(t) - (\eta_A + \mu_n)I_A(t) = 0$, we have

$$\begin{aligned} I_A &= \frac{p_A\gamma E(t)}{(\eta_A + \mu_n)} \\ so, I_A^* &= aE. \end{aligned} \tag{7.12}$$

where, $a = \frac{p_A\gamma}{(\eta_A+\mu_n)}$

From $\frac{dI_U}{dt}(t) = p_U\gamma E(t) - (\alpha_U + \eta_U + \mu_n)I_U(t) = 0$, we have

$$\begin{aligned} I_U &= \frac{p_U\gamma E(t)}{(\alpha_U + \eta_U + \mu_n)} \\ so, I_U^* &= uE. \end{aligned} \tag{7.13}$$

where, $u = \frac{p_U\gamma}{(\alpha_U+\eta_U+\mu_n)}$

From $\frac{dI_R}{dt}(t) = p_R\gamma E(t) - (\alpha_R + \eta_R + \mu_n)I_R(t) = 0$, we have

$$\begin{aligned} I_R &= \frac{p_R\gamma E(t)}{(\alpha_R + \eta_R + \mu_n)} \\ so, I_R^* &= rE. \end{aligned} \tag{7.14}$$

where, $r = \frac{p_R\gamma}{(\alpha_R+\eta_R+\mu_n)}$

From $\frac{dM_D}{dt}(t) = \eta_U I_U(t) + \eta_R I_R(t) - (\sigma_M + \eta_M + \mu_n)M_D(t) = 0$, we have

$$M_D = \frac{\eta_U I_U(t) + \eta_R I_R(t)}{(\sigma_M + \eta_M + \mu_n)}$$
$$so, M_D^* = dE. \tag{7.15}$$

where, $d = \frac{\eta_U u + \eta_R r}{(\sigma_M + \eta_M + \mu_n)}$

From $\frac{dS_D}{dt}(t) = \alpha_U I_U(t) + \alpha_R I_R(t) - (\sigma_S + \alpha_S + \mu_s + \mu_n) S_D(t) = 0$, we have

$$S_D = \frac{\alpha_U I_U(t) + \alpha_R I_R(t)}{(\sigma_S + \alpha_S + \mu_s + \mu_n)}$$
$$so, S_D^* = s_d E. \tag{7.16}$$

where, $s_d = \frac{\alpha_U u + \alpha_R r}{(\sigma_S + \alpha_S + \mu_s + \mu_n)}$

From $\frac{dR}{dt}(t) = \eta_A I_A(t) + (\sigma_M + \eta_M) M_D(t) + (\sigma_S + \alpha_S) S_D(t) + P\Lambda - \mu_n R(t) = 0$,

we have

$$R = P\Lambda + \frac{((\sigma_M + \eta_M) d + (\sigma_S + \alpha_S) s_d)}{\mu_n} E(t)$$
$$so, R^* = yE. \tag{7.17}$$

where, $y = P\Lambda + \frac{((\sigma_M + \eta_M) d + (\sigma_S + \alpha_S) s_d)}{\mu_n}$

By adding the first two equation of the system (7.1),

$$(1 - P)\Lambda - S(t)(\beta_A I_A(t) + \beta_U I_U(t) + \beta_R I_R(t) + \mu_n) = 0 \tag{7.18}$$

$$S(t)(\beta_A I_A(t) + \beta_U I_U(t) + \beta_R I_R(t)) - (\gamma + \mu_n) E(t) = 0 \tag{7.19}$$

We got,

$$S = \frac{(1-P)\Lambda - (\mu_n + \gamma)}{\mu_n} E(t)$$
$$so, S^* = bE. \tag{7.20}$$

where, $b = \frac{(1-P)\Lambda-(\mu_n+\gamma)}{\mu_n}$ □

Substituting the the values of (7.12), (7.13), (7.14), and (7.20) in the equation (7.19), we got,

$$E^* = \frac{\gamma + \mu_n}{b(\beta_A a + \beta_U u + \beta_R r)} \tag{7.21}$$

Where, $b = \frac{(1-P)\Lambda-(\mu_n+\gamma)}{\mu_n}$, $a = \frac{p_A\gamma}{(\eta_A+\mu_n)}$, $u = \frac{p_U\gamma}{(\alpha_U+\eta_U+\mu_n)}$, and $r = \frac{p_R\gamma}{(\alpha_R+\eta_R+\mu_n)}$
Hence, the endemic equilibrium point satisfied at:

$$EE = (S^*, E^*, I_A^*, I_U^*, I_R^*, M_D^*, S_D^*, R^*). \tag{7.22}$$

## 7.5 Local Stability of the Equilibriums

Local stability of equilibrium means that the solutions with initial values close to this equilibrium remain close to the equilibrium and approach the equilibrium.

### Local Stability of the Disease-Free Equilibrium

THEOREM 7.6. The disease-free equilibrium of the model (7.1) is locally asymptotically stable when $R_0 < 1$ and unstable when $R_0 > 1$.

PROOF. We tried to use the Jacobian stability approach to prove the stability of the disease-free equilibrium state. From the previous section, we have the Jacobian

matrix evaluated at disease-free equilibrium which is given by

$$J_{DFE} = \begin{pmatrix} -\mu_n & 0 & -\frac{\beta_A\Lambda(1-P)}{\mu_n} & -\frac{\beta_U\Lambda(1-P)}{\mu_n} & -\frac{\beta_R\Lambda(1-P)}{\mu_n} & 0 & 0 & 0 \\ 0 & -(\gamma+\mu_n) & \frac{\beta_A\Lambda(1-P)}{\mu_n} & \frac{\beta_U\Lambda(1-P)}{\mu_n} & \frac{\beta_R\Lambda(1-P)}{\mu_n} & 0 & 0 & 0 \\ 0 & p_A\gamma & -(\eta_A+\mu_n) & 0 & 0 & 0 & 0 & 0 \\ 0 & p_U\gamma & 0 & -(\alpha_U+\eta_U+\mu_n) & 0 & 0 & 0 & 0 \\ 0 & p_R\gamma & 0 & 0 & -(\alpha_R+\eta_R+\mu_n) & 0 & 0 & 0 \\ 0 & 0 & 0 & \eta_U & \eta_R & -(\sigma_M+\eta_M+\mu_n) & 0 & 0 \\ 0 & 0 & 0 & \alpha_U & \alpha_R & 0 & -(\sigma_S+\alpha_S+\mu_s+\mu_n) & 0 \\ 0 & 0 & \eta_A & 0 & 0 & (\sigma_M+\eta_M) & (\sigma_S+\alpha_S) & -\mu_n \end{pmatrix} \tag{7.23}$$

For DFE being stable, all eigenvalues of $J_{DFE}$ must have negative real parts.

From (7.23), we see that the eigenvalues are $\lambda_1 = -\mu$, $\lambda_2 = -(\sigma_S + \alpha_S + \mu_s + \mu_n)$, $\lambda_3 = -(\sigma_M + \eta_M + \mu_n)$, and $\lambda_4 = -\mu$ which reduce the Jacobian matrix to $4 \times 4$ as following:

$$J_{DFE} = \begin{pmatrix} -(\gamma + \mu_n) & \frac{\beta_A\Lambda(1-P)}{\mu_n} & \frac{\beta_U\Lambda(1-P)}{\mu_n} & \frac{\beta_R\Lambda(1-P)}{\mu_n} \\ p_A\gamma & -(\eta_A + \mu_n) & 0 & 0 \\ p_U\gamma & 0 & -(\alpha_U + \eta_U + \mu_n) & 0 \\ p_R\gamma & 0 & 0 & -(\alpha_R + \eta_R + \mu_n) \end{pmatrix} \tag{7.24}$$

Using wolfram alpha command eigenvalues$(-a, b, c, d), (e, -f, 0, 0), (g, 0, -h, 0), (i, 0, 0, -j)$ we can get all eigenvalues of the reduced $4 \times 4$ matrix where $a = -(\gamma + \mu_n)$, $b = \frac{\beta_A\Lambda(1-P)}{\mu_n}$, $c = \frac{\beta_U\Lambda(1-P)}{\mu_n}$, $d = \frac{\beta_R\Lambda(1-P)}{\mu_n}$, $e = p_A\gamma$, $f = -(\eta_A + \mu_n)$, $g = p_U\gamma$, $h = -(\alpha_U + \eta_U + \mu_n)$, $i = p_R\gamma$, and $j = -(\alpha_R + \eta_R + \mu_n)$.

However, the expressions are tedious and extremely long (about 20 pages for all eigenvalues expressions). Therefore, it is not practical to use the standard stability analysis and determine the stability of the disease-free equilibrium. Instead, we can use the following Theorem which was proved by Pauline van den Driessche [149].

THEOREM 7.7. Consider the disease transmission model given by (7.1) with $f(x)$ satisfying conditions (A1)–(A5). If $x_0$ is a DFE of the model, then $x_0$ is locally asymptotically stable if $R_0 < 1$, but unstable if $R_0 > 1$, where $R_0$ is defined by (7.9).

PROOF. Conditions A1 and A2 are satisfied by Theorem 7.1 and Theorem 7.2 (positivity and boundedness theorems). Conditions A3 and A4 are automatically satisfied by the structure of the proposed model (7.1). Condition A5 is saying that the eigenvalues of (7.23) must all have negative real parts if all transmission rates are equal to zero. We already showed that $\lambda_1, \lambda_2, \lambda_3$, and $\lambda_4$ are negative. If all transmission rates are equal to zero, so, $\beta_A = \beta_U = \beta_R = 0$. Then $b, c$ and $d = 0$ in the matrix (7.24) will be all zero.
Therefore, the eigenvalues will be: $\lambda_5 = -(\gamma + \mu_n)$, $\lambda_6 = -(\eta_A + \mu_n)$, $\lambda_7 = -(\alpha_U + \eta_U + \mu_n)$, and $\lambda_8 = -(\alpha_R + \eta_R + \mu_n)$. Hence, the disease free equilibrium is locally asymptotically stable. □

□

**Local Stability of the Endemic Equilibrium**

THEOREM 7.8. The endemic equilibrium is locally asymptotically stable if the basic reproduction number $R_0 > 1$.

PROOF. In Theorem 7.5, we proved the, the uniqueness of endemic equilibrium $EE = (S^*, E^*, I_A^*, I_U^*, I_R^*, M_D^*, S_D^*, R^*)$ such that:

$$S^* = \frac{(1-P)\Lambda - (\mu_n + \gamma)}{\mu_n} E(t) \tag{7.25}$$

$$I_A^* = \frac{p_A \gamma}{(\eta_A + \mu_n)} E(t) \tag{7.26}$$

$$I_U^* = \frac{p_U \gamma}{(\alpha_U + \eta_U + \mu_n)} E(t) \tag{7.27}$$

$$I_R^* = \frac{p_R \gamma}{(\alpha_R + \eta_R + \mu_n)} E(t) \tag{7.28}$$

$$M_D^* = \frac{\eta_U I_U(t) + \eta_R I_R(t)}{(\sigma_M + \eta_M + \mu_n)} \tag{7.29}$$

$$S_D^* = \frac{\alpha_U I_U(t) + \alpha_R I_R(t)}{(\sigma_S + \alpha_S + \mu_s + \mu_n)} \tag{7.30}$$

$$R^* = P\Lambda + \frac{((\sigma_M + \eta_M)d + (\sigma_S + \alpha_S)s_d)}{\mu_n} E(t) \tag{7.31}$$

$$E^* = \frac{\gamma + \mu_n}{b(\beta_A a + \beta_U u + \beta_R r)} \tag{7.32}$$

Where, $b = \frac{(1-P)\Lambda - (\mu_n + \gamma)}{\mu_n}$, $a = \frac{p_A \gamma}{(\eta_A + \mu_n)}$, $u = \frac{p_U \gamma}{(\alpha_U + \eta_U + \mu_n)}$, and $r = \frac{p_R \gamma}{(\alpha_R + \eta_R + \mu_n)}$

We noticed that all the endemic points depend on the exposed point. We can write $E^*$ in the term of $R_0$ such that:

$$E^* = \frac{(a\beta_A + u\beta_U + r\beta_R)}{R_0 - 1} \tag{7.33}$$

It can be seen that the model has no positive endemic equilibrium if $R_0 < 1$ since $E^*, I_A^*, I_U^*, I_R^*$ would be negative, which indicate an unrealistic biological system. Hence, for a positive endemic equilibrium system, we would require that $R_0 > 1$.

□

## 7.6 Hopf Bifurcation

Hopf bifurcation is one of the most common methods for generating limit cycles and recurring phenomena. The Hopf bifurcation point arises when the Jacobian matrix of a dynamic system evaluated at equilibrium, includes a simple pair of entirely imaginary eigenvalues, resulting in a nonhyperbolic critical point [147]. More precisely, Hopf bifurcation is a local bifurcation in which a dynamical system's equilibrium loses stability due to a pair of complex conjugate eigenvalues, and their real parts change from a negative value to a positive value. A small-amplitude limit cycle branches from the equilibrium under adequately general assumptions about the dynamical system.

The qualitative picture of the flows of Hopf bifurcation can be revealed by analyzing the stability and bifurcations based on the standard form, and the stability of the bifurcating limit cycle is determined by the coefficients of the standard form. Hopf bifurcations can be classified as supercritical or subcritical, indicating whether the bifurcating limit cycle is stable or unstable.

To obtain the necessary and sufficient conditions for the occurrence of a Hopf bifurcation around the endemic equilibrium, we need to do the following steps:

1. Use the Jacobian matrix and evaluate it at the endemic equilibrium $(S^*, E^*, I_A^*, I_U^*, I_R^*, M_D^*, S_D^*, R^*)$. We do not need to know the exact expression of the endemic equilibrium. Simply, we enter $(S^*, E^*, I_A^*, I_U^*, I_R^*, M_D^*, S_D^*, R^*)$.
2. Find as many as eigenvalues that we can, and write the characteristic equation.
3. Make simplifying assumptions to change the highest degree of the polynomial

to polynomial of degree 3.

To determine the qualitative behaviors of the models, we need to know if the eigenvalues of the endemic equilibrium can become complex or not. Here are the possibilities:

- All eigenvalues are real and negative: the endemic equilibrium is asymptotically stable and the solution curves are all monotonic (i.e. the are no oscillations about the endemic equilibrium).
- All eigenvalues are real and non-positive: the endemic equilibrium could be stable in Liapunov sense.
- There is an eigenvalue with positive real part: the endemic equilibrium is unstable and disease-free equilibrium is stable.
- Some eigenvalues are complex with negative real parts and the rest are real and negative: the endemic equilibrium is asymptotically stable and the solution curves are all oscillatory and converging to the endemic equilibrium.
- Some eigenvalues are complex with positive real parts and the rest are real and negative: the endemic equilibrium is unstable and the solution curves are all oscillatory and diverge from the endemic equilibrium.

**Hopf Bifurcation Analysis of the Proposed Model (7.1)**

We focued on studying the phenomenon of Hopf bifurcation, which could occur around an endemic equilibrium of the system (7.1) when the real part of two complex, conjugate eigenvalues with nonzero imaginary part crosses zero.

THEOREM 7.9. If $\beta_R = 0$, $\beta_U = 0$, $C > 0$, $a_1^2 - 4b_1 < 0$, and $a_1$ changing from negative to positive, then the model exhibits a Hopf bifurcation.

PROOF. By use the Jacobian matrix and evaluate it at the endemic equilibrium, we have,

$$J_{EE} = \begin{pmatrix} a_{11} & 0 & -\beta_A S^* & -\beta_U S^* & -\beta_R S^* & 0 & 0 & 0 \\ a_{21} & -(\gamma+\mu_n) & \beta_A S^* & \beta_U S^* & \beta_R S^* & 0 & 0 & 0 \\ 0 & p_A\gamma & -(\eta_A+\mu_n) & 0 & 0 & 0 & 0 & 0 \\ 0 & p_U\gamma & 0 & -(\alpha_U+\eta_U+\mu_n) & 0 & 0 & 0 & 0 \\ 0 & p_R\gamma & 0 & 0 & -(\alpha_R+\eta_R+\mu_n) & 0 & 0 & 0 \\ 0 & 0 & 0 & \eta_U & \eta_R & -(\sigma_M+\eta_M+\mu_n) & 0 & 0 \\ 0 & 0 & 0 & \alpha_U & \alpha_R & 0 & -(\sigma_S+\alpha_S+\mu_s+\mu_n) & 0 \\ 0 & 0 & \eta_A & 0 & 0 & (\sigma_M+\eta_M) & (\sigma_S+\alpha_S) & -\mu_n \end{pmatrix} \tag{7.34}$$

Where,

$$a_{11} = -(\beta_A I_A^*(t) + \beta_U I_U^*(t) + \beta_R I_R^*(t)) - \mu_n.$$

$$a_{21} = (\beta_A I_A^*(t) + \beta_U I_U^*(t) + \beta_R I_R^*(t)).$$

To search for Hopf bifurcation case, we make simplifying assumptions to change $8 \times 8$ matrix to $3 \times 3$ matrix by put $\beta_R = \beta_U = 0$ (transmission of infection from undocumented and reported individuals is negligible). Hence, we get,

$$J_{EE} = \begin{pmatrix} -(\beta_A I_A^*(t) + \mu_n) & 0 & -\beta_A S^* \\ \beta_A I_A^*(t) & -(\gamma + \mu_n) & \beta_A S^* \\ 0 & p_A\gamma & -(\eta_A + \mu_n) \end{pmatrix} \tag{7.35}$$

Then, the characteristic equation of the reduced system (7.1) at an endemic equilibrium $EE^* = (S^*, E^*, I_A^*, I_U^*, I_R^*, M_D^*, S_D^*, R^*)$ was computed from (7.35) and is given by:

$$P(\lambda) = \lambda^3 + A\lambda^2 + B\lambda + C = 0 \tag{7.36}$$

Where,

$$A = \beta_A I_A^* + \gamma + \eta_A + 3\mu_n.$$

$$B = (\beta_A I_A^* + \mu_n)(\gamma + \mu_n) + (\beta_A I_A^* + \mu_n)(\eta_A + \mu_n) + (\gamma + \mu_n)(\eta_A + \mu_n) - \beta_A S^* p_A \gamma.$$

$$C = (\beta_A S^* \beta_A I_A^* p_A \gamma) + (\beta_A I_A^* + \mu_n)(\gamma + \mu_n)(\eta_A + \mu_n) - (\beta_A I_A^* + \mu_n) P_A \gamma \beta_A S^*. \tag{7.37}$$

We obtained necessary and sufficient conditions for the occurrence of a Hopf bifurcation around $EE^* = (S^*, E^*, I_A^*, I_U^*, I_R^*, M_D^*, S_D^*, R^*)$.

LEMMA 7.10. If $C > 0$, then $P(\lambda)$ has a real negative root.

PROOF. We have $\lim_{\lambda \to \infty} P(\lambda) = \infty$, and $P(0) = C > 0$. Hence by Intermediate Value Theorem (IVT), $P(\lambda)$ must have a negative real roots. □

Hence, by Lemma 7.10, equation (7.36) can be written in the form:

$$P(\lambda) = \lambda^3 + (a_1 - r_1)\lambda^2 + (b_1 - r_1 a_1)\lambda - r_1 b_1 = 0 \tag{7.38}$$

By equating equation (7.36) and equation (7.38), we get that:

$$\begin{aligned} A &= a_1 - r_1 \\ B &= b_1 - r_1 a_1 \\ C &= -r_1 b_1 \end{aligned} \tag{7.39}$$

From equations (7.37) and (7.39), we got that,

$$a_1 = \beta_A I_A^* + \gamma + \eta_A + 3\mu_n + r_1$$

$$b_1 = (\beta_A I_A^* + \mu_n)(\gamma + \mu_n) + (\beta_A I_A^* + \mu_n)(\eta_A + \mu_n) + (\gamma + \mu_n)(\eta_A + \mu_n) - \beta_A S^* p_A \gamma + r_1 a_1 \tag{7.40}$$

Then, the roots of the equation (7.38) is given by:

$$\begin{cases} r_1 \\ -a_1/2 - (a_1^2 - 4b_1)^{(1/2)}/2 \\ (a_1^2 - 4b_1)^{(1/2)}/2 - a_1/2 \end{cases} \tag{7.41}$$

Therefore, For Hopf bifurcation to occur, we need these conditions to be satisfied: $a_1^2 - 4b_1 < 0$, and $a_1$ changing from negative to positive. □

THEOREM 7.11. Suppose that the $C^4$-system (7.1) with $\mathbf{x} \in \mathbf{R}^n$ and $\mu \in \mathbf{R}$ has a critical point $\mathrm{x}_0$ for $\mu = \mu_0$ and that $D\mathrm{f}(\mathrm{x}_0, \mu_0)$ has a simple pair of pure imaginary eigenvalues and no other eigenvalues with zero real part. Then there is a smooth curve of equilibrium points $\mathbf{x}(\mu)$ with $\mathbf{x}(\mu_0) = \mathbf{x}_0$ and the eigenvalues, $\lambda(\mu)$ and $\bar{\lambda}(\mu)$ of $\mathrm{Df}(\mathbf{x}(\mu), \mu)$, which are pure imaginary at $\mu = \mu_0$, vary smoothly with $\mu$. Furthermore, if

$$\frac{d}{d\mu}[\mathrm{Re}\,\lambda(\mu)]_{\mu=\mu_0} \neq 0$$

then there is a unique two-dimensional center manifold passing through the point $(x_0, \mu_0)$ and a smooth transformation of coordinates such that the system (7.1) on the center manifold is transformed into the normal form

$$\dot{x} = -y + ax\left(x^2 + y^2\right) - by\left(x^2 + y^2\right) + O\left(|x|^4\right)$$

$$\dot{y} = x + bx\left(x^2 + y^2\right) + ay\left(x^2 + y^2\right) + O\left(|x|^4\right)$$

in a neighborhood of the origin which, for $a \neq 0$, has a weak focus of multiplicity one at the origin and

$$\dot{x} = \mu x - y + ax\left(x^2 + y^2\right) - by\left(x^2 + y^2\right)$$

$$\dot{y} = x + \mu y + bx\left(x^2 + y^2\right) + ay\left(x^2 + y^2\right)$$

is a universal unfolding of this normal form in a neighborhood of the origin on the center manifold.

PROOF. The proof of the theorem is given in [158]. □

THEOREM 7.12. if $\lambda_1 < 0$, and $Re(\lambda_2) = Re(\lambda_3)$ goes from negative to positive, then we have a Hopf bifurcation.

PROOF. The following table covers the cases that have the complex conjugate roots and negative real part root. In each case, if the real part of $\lambda_2$ and $\lambda_3$ goes from negative to positive , then we have a Hopf bifurcation.

Table 17: Hopf bifurcation cases.

| $P(\lambda) = \lambda^3 + A\lambda^2 + B\lambda + C = 0$<br>Sufficient Conditions | Roots |
|---|---|
| Case 1 : $\beta < -2\alpha^{3/2}$ | $\lambda_1 = -2\alpha^{1/2}cosh\psi - a_1$<br>$\lambda_2 = \alpha^{1/2}cosh\psi - a_1 + i(3\alpha)^{1/2}sinh\psi$<br>$\lambda_3 = \alpha^{1/2}cosh\psi - a_1 - i(3\alpha)^{1/2}sinh\psi$ |
| Case 2: $\alpha = 0$, $-\infty < \beta < \infty$ | $\lambda_1 = -\beta^{1/3} - a_1$<br>$\lambda_2 = \beta^{1/3} - a_1 + 3i\beta^{2/3}/4$<br>$\lambda_3 = \beta^{1/3} - a_1 - 3i\beta^{2/3}/4$ |
| Case 3: $\alpha < 0$, $-\infty < \beta < \infty$ | $\lambda_1 = -2\alpha^{1/2}sinh\theta - a_1$<br>$\lambda_2 = -\alpha^{1/2}sinh\theta - a_1 + i(-3\alpha)^{1/2}cosh\theta$<br>$\lambda_3 = -\alpha^{1/2}sinh\theta - a_1 - i(-3\alpha)^{1/2}cosh\theta$ |

Where, $a_1 = \beta_A I_A^* + \gamma + \eta_A + 3\mu_n + r_1$, $b_1 = (\beta_A I_A^* + \mu_n)(\gamma + \mu_n) + (\beta_A I_A^* + \mu_n)(\eta_A + \mu_n) + (\gamma + \mu_n)(\eta_A + \mu_n) - \beta_A S^* p_A \gamma + r_1 a_1$, $C = -r_1 b_1$, $A \equiv 3a_1, B \equiv 3b_1, \alpha \equiv a_1^2 - b_1$, $\beta \equiv 2a_1^3 - 3a_1 b_1 + C$, $\psi = (1/3)\cosh^{-1}\left\{|\beta|/\left[2\alpha^{3/2}\right]\right\}$, and $\theta = (1/3)\sinh^{-1}\left\{\beta/\left[2(-\alpha)^{3/2}\right]\right\}$.

Based on Table 17, in case 1, if $\beta < -2\alpha^{3/2}$, Hopf bifurcation occurred when $\lambda_1 < 0$ and $Re(\lambda_2) = Re(\lambda_3) = (\alpha^{1/2}cosh\psi - a_1)$ changed from negative to positive. In case 2, if $\alpha = 0$ and $-\infty < \beta < \infty$, Hopf bifurcation occurred when $Re(\lambda_2) = Re(\lambda_3) = (\beta^{1/3} - a_1)$ changed from negative to positive. In case 3, if $\alpha < 0$ and, $-\infty < \beta < \infty$, Hopf bifurcation occurred when $Re(\lambda_2) = Re(\lambda_3) = (-\alpha^{1/2}sinh\theta - a_1)$ changed from negative to positive.

□

**Numerical Verification of Hopf Bifurcation**

We carried out numerical simulations of the model (7.1), in order to obtain Hopf bifurcation. The equations of the model (7.1) were solved numerically using the MATLAB ode45 solver which is based on the fourth-order Runge-Kutta method. The stability of the method was well established in [50].

If we consider the set of parameters, $\beta_A = 0.01$, $p_A = 0.2$, $p_U = 0.3$, $p_R = 0.47$, $\eta_A = 0.5$, $\eta_U = 0.05$ , $\alpha_U = 0.01$, $\eta_R = 0.02$, $\alpha_R = 0.01$, $\sigma_M = 0.1$, $\eta_M = 0.09$, $\sigma_S = 0.0009$, $\alpha_S = 0.0001$, $\mu_s = 0.195$, $\mu_n = 0.013$, $\gamma = 0.2$, $\lambda = 9$, and $P = 0.01$, we can see that system (7.1) has a unique endemic equilibrium $EE^* = (S^*, E^*, I_A^*, I_U^*, I_R^*, M_D^*, S_D^*, R^*) \approx (269, 25, 221, 57, 11, 4, 243)$.

Figure 23 shows the solution of the system (7.1) with with the initial conditions $S(0) = 1000, E(0) = 1, I_A(0) = 1, I_U(0) = 1, I_R(0) = 1, M_D = 1, S_D = 1, R = 1$. and it can be seen that all subpopulations converge to positive values, which represent the case when COVID-19 becomes endemic in the population.

However, a Hopf bifurcation occurs because the sign of $a_1$ is changed from negative to positive. Indeed, when $r_1 = -2$, the coefficients of the characteristic equation become $a_1 = -1.2415$, and $\Delta = -8.4925 < 0$, and when $\beta_A$ became 0.4, $a_1$ changed to positive to become $a_1 = 0.0307$, and $\Delta = -3.5424 < 0$ which satisfy the conditions of Theorem 7.9. Hence, endemic equilibrium point $EE^*$ switches from stable to unstable when $a_1^2 - 4b < 0$, and the sign of $a_1$ is changing from negative to positive. As a result, we observed that the model (7.1) exhibits Hopf bifurcation.

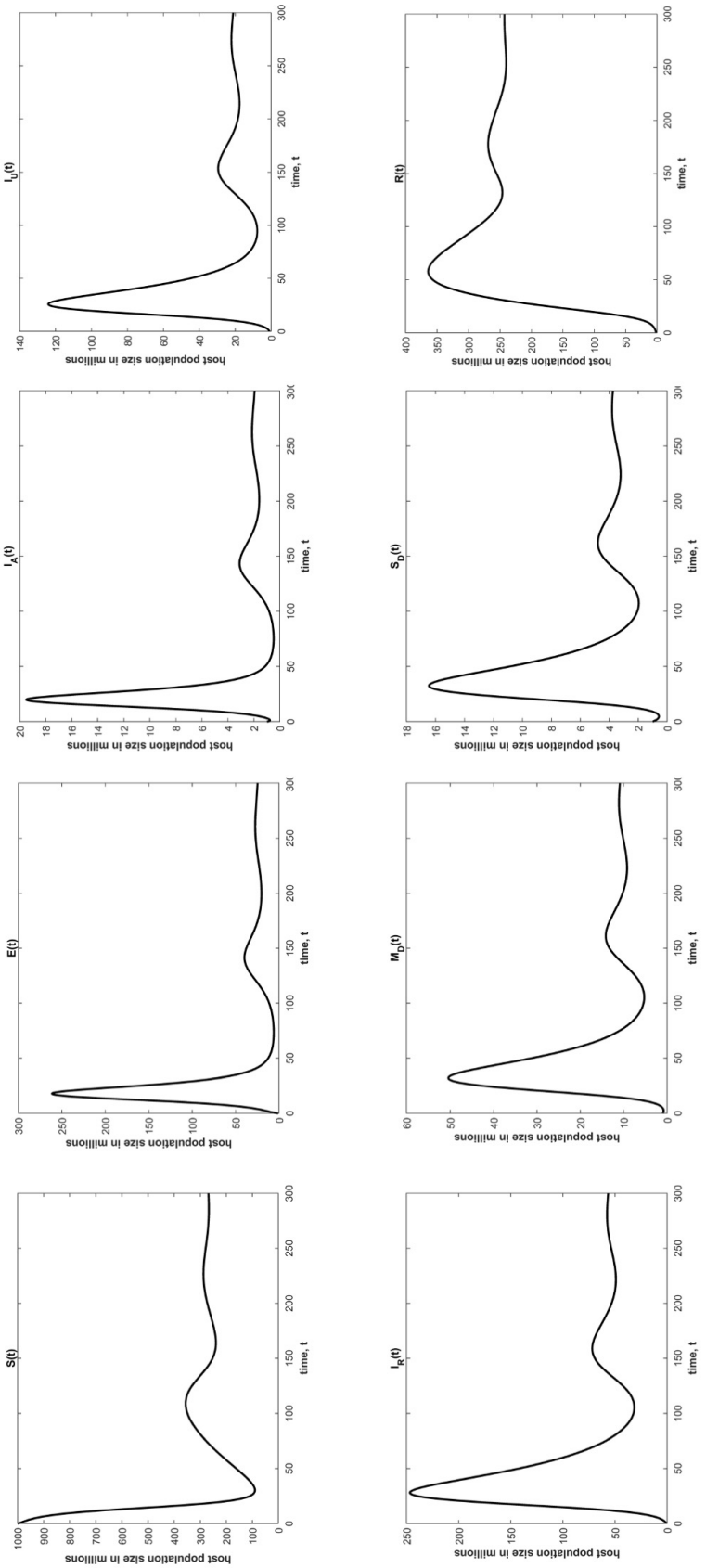


Figure 23: Hopf bifurcation for the model of COVID-19 (7.1).

## 7.7 Discussion and Conclusions

We proposed and studied COVID-19 epidemic model that includes three stages of infection compartment and two stages of disease compartment to investigate the dynamics of the Coronavirus Disease 2019 pandemic. In the present chapter, we analyzed the model (7.1) mathematically by proving the positivity and boundness of the model, and the uniqueness of the disease- free equilibrium and endemic equilibrium. Also, we proved the local stability of the disease-free equilibrium and endemic equilibrium. Moreover, we derived $R_0$ for the model (7.1). We concluded that the rate of reduction in $R_0$ with respect to vaccination rate is larger than the reduction rate with respect to transmission rates of the infection.

Epidemiologically, we understand the role of reproduction number in controlling disease. However, there are times that $R_0 < 1$ does not represent the eradication of the disease. Periodic waves can occur at that critical phase, which may be more endemic than the first. The periodic waves could be associated with several factors such as traveling, major social events, infection prevention measures, changes to the coronavirus itself, and the increase of people who become susceptible because they have not developed some immunity, whether from natural infection or through vaccination. [72]. Hence, public health departments and decision-makers need to increase the awareness in the societies. Wearing masks, avoiding crowds and poorly ventilated places, maintaining proper hygiene, adding more COVID-19 vaccination clinics and encouraging individuals to get the vaccine may help to control the severity and spread of the disease.

Also, we discussed Hopf bifurcation of the model to help government and policy makers decide an efficient response plan to combat periodic waves of the COVID-19 pandemic and to determine if the presence of COVID-19 oscillations can be due to it intrinsic nature. Studying Hopf bifurcation phenomena has important implications for epidemic control because this type of bifurcation can produce oscillatory patterns in the number of infected individuals. In the model (7.1), we have four classes of infected compartments: exposed, asymptomatic infected, undocumented infected, and reported infected. From Hopf bifurcation analysis of the proposed model (7.1), we can obtain the oscillations of the infected cases when the system loses stability at endemic equilibrium due to a pair of complex conjugate eigenvalues, and their real parts change from a negative value to a positive value. We verified mathematically and numerically the necessary and sufficient conditions for the occurrence of a Hopf bifurcation around the endemic point $EE^* = (S^*, E^*, I_A^*, I_U^*, I_R^*, M_D^*, S_D^*, R^*) \approx (269, 25, 221, 57, 11, 4, 243)$. Theses conditions include $C > 0$, $a_1^2 - 4b_1 < 0$, and $a_1$ changing from negative to positive.

Further research should still be conducted to improve our understanding of the COVID-19 model's different dynamics of oscillatory behavior. For instance, an initial investigation of the numerical solutions near the Hopf bifurcations is needed to observe if the oscillatory behavior of the model implies the stability of a range of periodic wave solutions. The most popular method for studying the stability of periodic wave is the Poincaré map that established by Henri Poincaré in 1881 [159]. The idea of the Poincaré map is as the following: If $\Gamma$ is a periodic orbit of the system

$$\dot{\mathbf{x}} = \mathbf{f}(\mathbf{x})$$

through the point $x_0$ and $\Sigma$ is a hyperplane perpendicular to $\Gamma$ at $x_0$, then for any point $\mathbf{x} \in \Sigma$ sufficiently near $\mathbf{x}_0$, the solution of the system through $\mathbf{x}$ at $t = 0, \phi_t(\mathbf{x})$, will cross $\Sigma$ again at a point $\mathbf{P}(\mathbf{x})$ near $\mathbf{x}_0$.

# CHAPTER 8

# CONCLUSIONS AND FUTURE WORK

## 8.1 Dissertation Conclusion

Although statistical and mathematical tools are essential to analyze the pandemic's distribution patterns, we should not expect perfect results reflecting complicated world issues. On the other hand, that does not mean these tools are useless. We made good predictions by incorporating human behaviors, beliefs, and demographical processes to improve the accuracy of the current epidemiological models. The modified models will help epidemiologists, decision-makers, and public health departments identify the dynamic spread and risk areas of the disease.

By using prospective spatial-temporal analysis, we were able to identify COVID-19 hotspot areas. Rapid detection of clusters can aid in determining the efficacy of current preventive and control policies. The prospective strategy described in Chapter 3 helped the KCMO Health Department quickly identify hot spots and allocate more resources to those regions to prevent similar outbreaks in the future. Adding more COVID-19 vaccination clinics or COVID-19 testing sites in high-risk areas may help control the severity and spread of the disease. Encouraging social distancing or enforcing mask mandates could also help prevent the spread of COVID-19 in these counties/regions. Surveillance data can help public health decision-makers better address the needs of under-served areas and promote a safer, healthier community.

It became clear that disparities would emerge among various demographics as

COVID-19 spread throughout communities. Therefore, we utilized retrospective spatial analysis concerning the demographic factors of gender, race, and ethnicity, which enabled us to provide an unbiased spatial analysis of COVID-19 data in Kansas City, MO. The spatial demographic analysis of COVID-19 data helped us gain a deeper understanding of disparities in the geographical distribution of COVID-19. Chapter 4 illustrates that specific demographics within Kansas City are more vulnerable to COVID-19 in spreading the disease and the resulting health outcomes after the illness.

Also, utilizing n-cluster combining with Ordinary Differential Equation (ODE) in Chapter 5 enabled us to predict $R_0$ for one cluster and two clusters. We studied and proved the impact of control measures and prevention, human behaviors, and beliefs on the spread of COVID-19 in the communities numerically. In Chapter 6, we modified the SIR model by using ODE and incorporating the global effects of COVID-19. We studied the prevalence of the COVID-19 infection in six randomly selected cities and states influenced by the COVID-19 global pandemic: Kansas City, Saint Louis, San Francisco, Missouri, Illinois, and Arizona. The extended SIR model significantly outperformed the standard SIR model and revealed oscillatory behaviors with an increasing trend of infected individuals. Also, the extended SIR enabled us to extract vital information (e.g., the presence of epidemic waves) from the data.

In addition, we built a mathematical model of COVID-19 to study the oscillatory behaviors of the number of COVID-19 infected by using Hopf bifurcation theorem in Chapter 7. We concluded that oscillations happen due to intrinsic nature of COVID-19 infection. Also, we were able to predict the $R_0$ for the COVID-19

model and we proved that the rate of reduction in $R_0$ with respect to vaccination rate is larger than the reduction rate with respect to transmission rate of the disease. Therefore, increasing the vaccination rate can control the spread of the disease in the community.

Finally, mathematical analysis of n-cluster and COVID-19 models make a contribution to mathematical studies as a whole. Through stability analysis and the existence of equilibria, we provide a usable model for future studies.

## 8.2 Future Work

There are several essential and relevant next steps to consider from this point forward. First, for prospective and retrospective analysis, we would like to complete the space-time analysis over an extended period which will provide a more reliable tool for surveillance after vaccine distribution. So, the trends and emerging clusters may change over time with updated current data. Second, we would like to examine spatial clusters with respect to demographic factors that adjust for age, socioeconomic status, and income level. Several studies suggested that these factors may impact the spread of COVID-19 across communities. Therefore, the adjusted analysis can improve the full perspective of spreading the disease in Kansas City, MO. Third, we can continue the analysis of the n-cluster model. It will be interesting to observe the dynamical system of n-cluster model when the model exceed two clusters. Also, we would like to pair the finding of emerging clusters of COVID-19 across Kansas City, MO at the zip code level with the n-cluster model using ordinary differential equations. We hope to estimate the Susceptible, Infected, and Recovered individuals (S,I,R) for each emerging cluster, and estimate the $R_0$ for each cluster by assuming

the human mobility between the clusters. Fourth, for COVID-19 model, we would establish conditions for stability of period solution wave.

# APPENDIX A

# SUPPLEMENTARY DOCUMENTS

## A.1 Supplementary Tables of Chapter 3 and Chapter 4

Table A1: Populations of Platte County, Clay County, and Jackson County in Kansas City, Missouri. These populations were collected based on zip code

| County | Platte County | Clay Couny | Jackson County | total |
|---|---|---|---|---|
| Population | 70,574 | 155,551 | 304,558 | 530,683 |

Table A2: Population of Platte County, Missouri based on the zip codes.

| zip code | population |
|---|---|
| 64151 | 26,128 |
| 64152 | 28,307 |
| 64153 | 5,383 |
| 64154 | 10,497 |
| 64164 | 259 |

Table A3: Population of Jackson County, Missouri based on the zip codes.

| zip code | Population |
|---|---|
| 64101 | 279 |
| 64102 | 0 |
| 64105 | 4,306 |
| 64106 | 9,360 |
| 64108 | 7,491 |
| 64109 | 9,188 |
| 64110 | 16,745 |
| 64111 | 17,398 |
| 64112 | 8,698 |
| 64113 | 12,120 |
| 64114 | 24,760 |
| 64120 | 297 |
| 64123 | 9,017 |
| 64124 | 10,534 |
| 64125 | 1,414 |
| 64126 | 6,488 |
| 64127 | 14,707 |
| 64128 | 12,056 |
| 64129 | 8,898 |
| 64130 | 20,215 |
| 64131 | 22,485 |
| 64132 | 14,474 |
| 64134 | 23,836 |
| 64136 | 2,211 |
| 64137 | 11,349 |
| 64138 | 26,485 |
| 64139 | 1,925 |
| 64145 | 5,288 |
| 64146 | 1,574 |
| 64147 | 640 |
| 64149 | 320 |

Table A4: Population of Clay County, Missouri based on the zip codes.

| zip code | population |
|---|---|
| 64116 | 15,372 |
| 64117 | 15,001 |
| 64118 | 42,493 |
| 64119 | 26,830 |
| 64155 | 23,108 |
| 64156 | 7,372 |
| 64157 | 19,680 |
| 64158 | 4,796 |
| 64165 | 197 |
| 64166 | 225 |
| 64167 | 477 |

## A.2 Generating Infected and Recovered Data Algorithm of Chapter 6

COVID-19 data used in this study were obtained from the health department of Kansas City, Saint Louis, San Francisco, Missouri, Illinois, and Arizona. The data were dated from March 10, 2020 March 7, 2021(a total of 363 days) Specifically, the data variables consisted of date, total number of cases, new cases, total deaths, new deaths and total number of individuals tested for COVID-19. We used abovementioned data to extract the daily number of recovered and susceptible and infected individuals.

To estimate the number of susceptible individuals, we assumed an average incubation period is 5 days for COVID-19. We also considered one day for obtaining the COVID-19 test results. Hence, all of those who were tested positive were susceptible from the beginning until 6 days prior to obtaining the test results. Also, we added the individual who take the test, but their results were negative. These individuals had presumably high risk of getting infected and therefore susceptible. The number of infected individuals were calculated by considering an average infection period 14 days. Hence, we cumulatively added of new cases for 14 days until they recovered. The algorithm to calculate the number of infected and recovered individuals as the following: $I(t) = N_i(1) + N_i(2) + ... + N_i(14)$, where $N_i$ is the infected individual at time t, and $t = 14$ days is the average time to get recovered from COVID-19.

I(2) = $N_i(1) + N_i(2)$

I(3) = $N_i(1) + N_i(2) + N_i(3)$

...

I(14) = $N_i(1) + N_i(2) + N_i(3) + \ldots + N_i(14)$

I(15) = $N_i(1) + N_i(2) + N_i(3) + \ldots + N_i(14) + N_i(15) - N_i(1)$ where infected cases at timet = 1

who get infected 14 days ago) is either recovered or died.

I(16) = $N_i(2) + \ldots + N_i(14) + N_i(15) + N_i(16)$

So,

For i = 1 : 14

value = $N_i$ (i)

I(i) = Cumsum(value)

end

For i = 15 : 212

value = $N_i$ (i-13:i)

I(i) = Cumsum(value)

end

For i = 15 : 212

(Cumulative infected cases from day 1 until day 14)

(A.1)

end

For i = 15 : 212

$value = N_i(i - 13 : i)$

I(i) = Cumsum(value)

end For i = 15 : 212

h = $N_i(1 : \text{i} - 15)$

R(i) = random(95 : 99) Cumsum(h)-Ndeath(i). Where Ndeath(i) is cumulative death cases until day t.

In the algorithm, we assume the percentage of recovered case between (95%- 99%) of the cumulative infected individual of COVID-19 until day t. Then, we subtracted from the cumulative number of death individual until day t.

## A.3 Supplementary Tables of Chapter 6

Table A5: Descriptive Statistics of Kansas City, Missouri daily COVID-19 data from March 10, 2020 to March 15, 2021.

| | Susceptible | Infected | Recovered |
|---|---|---|---|
| Minimum | 1 | 1 | 3.63 |
| Maximum | 253055 | 418 | 33388.86 |
| Mean | 118601.41 | 101.720548 | 12992.06 |
| Median | 115547 | 79 | 9201.55 |
| Standard Deviation | 87126.9128 | 93.8125249 | 12012.59 |
| Range | 253054 | 417 | 33385.23 |

Table A6: Descriptive Statistics of St. Louis, Missouri daily COVID-19 data from March 3, 2020 to March 15, 2021.

| | Susceptible | Infected | Recovered |
|---|---|---|---|
| Minimum | 1 | 0 | 0.90 |
| Maximum | 100499 | 251 | 18754.13 |
| Mean | 35294.4 | 54.19 | 7480.48 |
| Median | 28388 | 39 | 5948.61 |
| Standard Deviation | 30681.17 | 45.47 | 6273.94 |
| Range | 100498 | 251 | 18753.23 |

Table A7: Descriptive Statistics of San Francisco, California daily COVID-19 data from March 3, 2020 to March 15, 2021.

| | Susceptible | Infected | Recovered |
|---|---|---|---|
| Minimum | 4 | 0 | 1.85 |
| Maximum | 1643808 | 561 | 31991 |
| Mean | 583213.60 | 91.78 | 11447.04 |
| Median | 443535.5 | 57 | 9373.5 |
| Standard Deviation | 525197 | 92.30 | 10111.63 |

Table A8: Descriptive Statistics of Missouri State daily COVID-19 data from March 7, 2020 to March 7, 2021

| | Susceptible | Infected | Recovered |
|---|---|---|---|
| Minimum | 23 | 0 | 0.92 |
| Maximum | 4565866 | 6346 | 447847.34 |
| Mean | 1766197.31 | 1316.83 | 149603.84 |
| Median | 1364523.5 | 1004 | 84019 |
| Standard Deviation | 1543442.31 | 1303.66 | 155729.18 |
| Range | 4565843 | 6346 | 447846.42 |

Table A9: Descriptive Statistics of Illinois State daily COVID-19 data from March 4, 2020 to March 7, 2021

| | Susceptible | Infected | Recovered |
|---|---|---|---|
| Minimum | 0 | 0 | 3.73 |
| Maximum | 18640190 | 15415 | 1110245.55 |
| Mean | 6211815.73 | 3247.51 | 380113.95 |
| Median | 4309941 | 1980 | 215210.61 |
| Standard Deviation | 5883615.78 | 3155.73 | 365143.84 |
| Range | 18640190 | 15415 | 1110241.82 |

Table A10: Descriptive Statistics of Arizona State daily COVID-19 data from March 4, 2020 to March 7, 2021

| | Susceptible | Infected | Recovered |
|---|---|---|---|
| Minimum | 33 | 0 | 1.81 |
| Maximum | 7908105 | 17234 | 759587.6 |
| Mean | 2490586.88 | 2239.71 | 234635.6 |
| Median | 1827793 | 1132 | 184042.15 |
| Standard Deviation | 2373491.59 | 2649.54 | 233107.15 |
| Range | 7908072 | 17234 | 759585.78 |

Table A11: Goodness of fit of Kansas City, Saint Louis, San Francisco, Missouri, Illinois, and Arizona data.

| Fitness | KC | SL | SF | MO | IL | AZ |
|---|---|---|---|---|---|---|
| $R^2$ (Adjusted $R^2$ ) for S | 0.9909 (0.9908) | 0.9911 (0.991) | 0.9802 (0.9801) | 0.9878 (0.9878) | 0.9761 (0.976) | 0.9583 (0.958) |
| $R^2$ (Adjusted $R^2$ ) for I | 0.9542 (0.9531) | 0.9287 (0.9271) | 0.962 (0.9611) | 0.9438 (0.9425) | 0.9015 (0.8993) | 0.9492 (0.948) |
| $R^2$ (Adjusted $R^2$ ) for R | 0.9873 (0.9872) | 0.9893 (0.9892) | 0.9804 (0.9803) | 0.9844 (0.9843) | 0.9748 (0.9747) | 0.9606 (0.9604) |

## A.4 Mathematical Theorems

THEOREM A1. [148] Let $A = [a_{ij}] \in \mathbb{R}^{n\times n}$ have $a_{ij} \leq 0$ for $i \neq j$. If the sum of the entries in each column is positive, then $A$ is a non-singular M-matrix.

THEOREM A2. [148] If $A = [a_{ij}]$ is an irreducible non-singular M-matrix, then $A$ has an (entry-wise) positive inverse i.e., $A^{-1} = [k_{ij}]$ with $k_{ij} > 0$ .

THEOREM A3. [148] If $A$ is a M-matrix, then, $s(-A) \leq 0$. If $A$ is a non-singular M-matrix, then $s(-A) < 0$.

THEOREM A4. [149] If $F$ is a non-singular matrix, and $V$ is a non-singular M-matrix then

$$s(F - V) < 0 (> 0) \Leftrightarrow \rho(FV^{-1}) < 1 (> 1)$$

DEFINITION A5. [148] Consider the system

$$\acute{a} = g(u)$$

with $g \in C^1[\mathbb{R}^n, \mathbb{R}^n]$, and $g(u_0) = 0$. Let $A$ be the Jacobian of $g(u_0)$ at $u_0$. Then, the equilibrium $u_0$ is locally asymptotically stable if $s(A) < 0$, and unstable if $s(A) > 0$.

REFERENCES


1. Ali, I. & Alharbi, O. COVID-19: Disease, management, treatment, and social impact. *Science Of The Total Environment*. **728** pp. 138861 (2020), https://www.sciencedirect.com/science/article/pii/S0048969720323780
2. Gunzler, D. & Sehgal, A. Time-Varying COVID-19 Reproduction Number in the United States. *MedRxiv : The Preprint Server For Health Sciences*. pp. 2020.04.10.20060863 (2020,4), https://pubmed.ncbi.nlm.nih.gov/32511659
3. Hossain, M., Hasana, S., Mamun, A., Uddin, M., Wahed, M., Sarker, S., Behl, T., Ullah, I., Begum, Y., Bulbul, I., Amran, M., Rahman, M., Bin-Jumah, M., Alkahtani, S., Mousa, S., Aleya, L. & Abdel-Daim, M. COVID-19 Outbreak: Pathogenesis, Current Therapies, and Potentials for Future Management . *Frontiers In Pharmacology* . **11** pp. 1590 (2020), https://www.frontiersin.org/article/10.3389/fphar.2020.563478
4. Lotfi, M., Hamblin, M. & Rezaei, N. COVID-19: Transmission, prevention, and potential therapeutic opportunities. *Clinica Chimica Acta; International Journal Of Clinical Chemistry*. **508** pp. 254-266 (2020,9), https://pubmed.ncbi.nlm.nih.gov/32474009
5. Triggle, C., Bansal,D., Farag, E., Ding, H., & Sultan, A. COVID-19: Learning from Lessons To Guide Treatment and Prevention Interventions. *MSphere*. **5**, e00317-20 (2021,11), https://doi.org/10.1128/mSphere.00317-20
6. Sy, K., White, L. & Nichols, B. Population density and basic reproductive

number of COVID-19 across United States counties. *PLOS ONE*. **16**, e0249271 (2021,4), https://doi.org/10.1371/journal.pone.0249271

7. Mizumoto, K. & Chowell, G. Estimating risk for death from coronavirus disease, China, january–february 2020. *Emerging Infectious Diseases*. **26**, 1251 (2020)
8. Weston, S. & Frieman, M. COVID-19: knowns, unknowns, and questions. *Msphere*. **5**, e00203-20 (2020)
9. Bi, Q., Wu, Y., Mei, S., Ye, C., Zou, X., Zhang, Z., Liu, X., Wei, L., Truelove, S., Zhang, T. & Others Epidemiology and Transmission of COVID-19 in Shenzhen China: Analysis of 391 cases and 1,286 of their close contacts. *MedRxiv*. (2020)
10. Al-Ahmadi, K., Alahmadi, S. & Al-Zahrani, A. Spatiotemporal Clustering of Middle East Respiratory Syndrome Coronavirus (MERS-CoV) Incidence in Saudi Arabia, 2012–2019. *International Journal Of Environmental Research And Public Health* . **16**,(14),2520 (2019)
11. Chowell, G. & Rothenberg, R. Spatial infectious disease epidemiology: on the cusp. *BMC Medicine*. **16**, 192 (2018), https://doi.org/10.1186/s12916-018-1184-6
12. Gomes, D., Andrade, L., Ribeiro, C., Peixoto, M., Lima, S., Duque, A., Cirilo, T., Góes, M., Lima, A., Santos, M., Araújo, K. & Santos, A. Risk clusters of COVID-19 transmission in northeastern Brazil: prospective space–time modelling. *Epidemiology And Infection*. **148** pp. e188 (2020), https://www.cambridge.org/core/article/risk-clusters-of-covid19-transmission-in-northeastern-brazil-prospective-spacetime-modelling/E87C8EDF8DF13485272A23F83145A0EA

13. Grassly, N. & Fraser, C. Mathematical models of infectious disease transmission. *Nature Reviews Microbiology.* **6**, 477-487 (2008), https://doi.org/10.1038/nrmicro1845
14. Balcan, D., Gonçalves, B., Hu, H., Ramasco, J., Colizza, V. & Vespignani, A. Modeling the spatial spread of infectious diseases: The GLobal Epidemic and Mobility computational model. *Journal Of Computational Science.* **1**, 132-145 (2010)
15. Lyseen, A., Nøhr, C., Sørensen, E., Gudes, O., Geraghty, E., Shaw, N., Bivona-Tellez, C., Group, I. & Others A review and framework for categorizing current research and development in health related geographical information systems (GIS) studies. *Yearbook Of Medical Informatics.* **23**, 110-124 (2014)
16. Mbunge, E. Integrating emerging technologies into COVID-19 contact tracing: Opportunities, challenges and pitfalls. *Diabetes & Metabolic Syndrome: Clinical Research & Reviews.* **14**, 1631-1636 (2020)
17. Gross, B., Zheng, Z., Liu, S., Chen, X., Sela, A., Li, J., Li, D. & Havlin, S. Spatio-temporal propagation of COVID-19 pandemics. *EPL (Europhysics Letters).* **131**, 58003 (2020)
18. Alshammari, F. A Mathematical Model to Investigate the Transmission of COVID-19 in the Kingdom of Saudi Arabia. *Computational And Mathematical Methods In Medicine.* **2020** pp. 9136157 (2020), https://doi.org/10.1155/2020/9136157
19. Bani-Yaghoub, M., Gautam, R., Dopfer, D., Kaspar, C. & Ivanek, R. Effectiveness of environmental decontamination as an

infection control measure. *Epidemiology And Infection.* **140**, 542-553 (2012), https://www.cambridge.org/core/article/effectiveness-of-environmental-decontamination-as-an-infection-control-measure/FA961694D9AAE4773379262975087191

20. Bani-Yaghoub, M., Gautam, R., Shuai, Z., Driessche, P. & Ivanek, R. Reproduction numbers for infections with free-living pathogens growing in the environment. *Journal Of Biological Dynamics.* **6**, 923-940 (2012,3), https://doi.org/10.1080/17513758.2012.693206
21. Brauer, F. Mathematical epidemiology: Past, present, and future. *Infectious Disease Modelling.* **2**, 113-127 (2017), http://www.sciencedirect.com/science/article/pii/S2468042716300367
22. Byrd, R., Hribar, M. & Nocedal, J. An Interior Point Algorithm for Large-Scale Nonlinear Programming. *SIAM Journal On Optimization.* **9**, 877-900 (1999,1), https://doi.org/10.1137/S1052623497325107
23. Cauchemez, S., Fraser, C., Van Kerkhove, M., Donnelly, C., Riley, S., Rambaut, A., Enouf, V., Werf, S. & Ferguson, N. Middle East respiratory syndrome coronavirus: quantification of the extent of the epidemic, surveillance biases, and transmissibility. *The Lancet Infectious Diseases.* **14**, 50-56 (2014), http://www.sciencedirect.com/science/article/pii/S1473309913703049
24. Centers for Disease Control and Prevention COVID-19 data Tracker. , https://covid.cdc.gov/covid-data-tracker/casescasesper100klast7days
25. Chen, T., Rui, J., Wang, Q., Zhao, Z., Cui, J. & Yin, L. A mathematical model for simulating the phase-based transmissibility of a novel coronavirus. *Infectious*

*Diseases Of Poverty*. **9**, 24 (2020), https://doi.org/10.1186/s40249-020-00640-3

26. Chu, D., Akl, E., Duda, S., Solo, K., Yaacoub, S., Schünemann, H., Chu, D., Akl, E., El-harakeh, A., Bognanni, A., Lotfi, T., Loeb, M., Hajizadeh, A., Bak, A., Izcovich, A., Cuello-Garcia, C., Chen, C., Harris, D., Borowiack, E., Chamseddine, F., Schünemann, F., Morgano, G., Muti Schünemann, G., Chen, G., Zhao, H., Neumann, I., Chan, J., Khabsa, J., Hneiny, L., Harrison, L., Smith, M., Rizk, N., Giorgi Rossi, P., AbiHanna, P., El-khoury, R., Stalteri, R., Baldeh, T., Piggott, T., Zhang, Y., Saad, Z., Khamis, A., Reinap, M., Duda, S., Solo, K., Yaacoub, S. & Schünemann, H. Physical distancing, face masks, and eye protection to prevent person-to-person transmission of SARS-CoV-2 and COVID-19: a systematic review and meta-analysis. *The Lancet*. **395**, 1973-1987 (2020), http://www.sciencedirect.com/science/article/pii/S0140673620311429
27. Chen, D. Modeling the spread of infectious diseases: A review. *Analyzing And Modeling Spatial And Temporal Dynamics Of Infectious Diseases*. pp. 19-42 (2014)
28. The Atlantic The COVID Tracking Project. , https://covidtracking.com/data
29. City of Kansas City Health Department KCMO Stay at home order. , https://www.kcmo.gov/city-hall/departments/health/coronavirus-covid-19/stay-at-home-order-faq
30. Del Valle, S., Hethcote, H., Hyman, J. & Castillo-Chavez, C. Effects of behavioral changes in a smallpox attack model. *Mathematical Biosciences*. **195**, 228-251 (2005), http://www.sciencedirect.com/science/article/pii/S0025556405000593
31. Edoh, K. & MacCarthy, E. Network and equation-based models in epidemiology.

*International Journal Of Biomathematics*. **11** (2018,3)

32. Gai, C., Iron, D. & Kolokolnikov, T. Localized outbreaks in an S-I-R model with diffusion. *Journal Of Mathematical Biology*. **80**, 1389-1411 (2020), https://doi.org/10.1007/s00285-020-01466-1
33. Gautam, R., Lahodny, G., Bani-Yaghoub, M., Morley, P. & Ivanek, R. Understanding the role of cleaning in the control of Salmonella Typhimurium in grower-finisher pigs: a modelling approach. *Epidemiology And Infection*. **142**, 1034-1049 (2014), https://www.cambridge.org/core/article/understanding-the-role-of-cleaning-in-the-control-of-salmonella-typhimurium-in-growerfinisher-pigs-a-modelling-approach/0583A9978A127B4F47482EE6A8B048DF
34. Gautam, R., Bani-Yaghoub, M., Neill, W., Döpfer, D., Kaspar, C. & Ivanek, R. Modeling the effect of seasonal variation in ambient temperature on the transmission dynamics of a pathogen with a free-living stage: example of Escherichia coli O157:H7 in a dairy herd. *Preventive Veterinary Medicine*. **102**, 10-21 (2011), http://europepmc.org/abstract/MED/21764472
35. Harko, T., Lobo, F. & Mak, M. Exact analytical solutions of the Susceptible-Infected-Recovered (SIR) epidemic model and of the SIR model with equal death and birth rates. *Applied Mathematics And Computation*. **236** pp. 184-194 (2014), http://www.sciencedirect.com/science/article/pii/S009630031400383X
36. Hejblum, G., Setbon, M., Temime, L., Lesieur, S. & Valleron, A. Modelers' Perception of Mathematical Modeling in Epidemiology: A Web-Based Survey. *PLOS ONE*. **6**, e16531 (2011,1), https://doi.org/10.1371/journal.pone.0016531
37. Huppert, A. & Katriel, G. Mathematical modelling and prediction in infectious

disease epidemiology. *Clinical Microbiology And Infection.* **19**, 999-1005 (2013), http://www.sciencedirect.com/science/article/pii/S1198743X14630019

38. Ivorra, B., Ferrández, M., Vela-Pérez, M. & Ramos, A. Mathematical modeling of the spread of the coronavirus disease 2019 (COVID-19) taking into account the undetected infections. The case of China. *Communications In Nonlinear Science And Numerical Simulation.* **88** pp. 105303 (2020), http://www.sciencedirect.com/science/article/pii/S1007570420301350
39. Keeling, M. & Danon, L. Mathematical modelling of infectious diseases. *British Medical Bulletin.* **92**, 33-42 (2009,12), https://doi.org/10.1093/bmb/ldp038
40. Kermack, W. & McKendrick, A. Contributions to the mathematical theory of epidemics—III. Further studies of the problem of endemicity. *Bulletin Of Mathematical Biology.* **53**, 89-118 (1991), https://doi.org/10.1007/BF02464425
41. Kermack, W. & McKendrick, A. Contributions to the mathematical theory of epidemics—II. The problem of endemicity. *Bulletin Of Mathematical Biology.* **53**, 57-87 (1991), https://doi.org/10.1007/BF02464424
42. Kermack, W. & McKendrick, A. Contributions to the mathematical theory of epidemics—I. *Bulletin Of Mathematical Biology.* **53**, 33-55 (1991), https://doi.org/10.1007/BF02464423
43. Kim, S., Lee, J. & Jung, E. Mathematical model of transmission dynamics and optimal control strategies for 2009 A/H1N1 influenza in the Republic of Korea. *Journal Of Theoretical Biology.* **412** pp. 74-85 (2017), http://www.sciencedirect.com/science/article/pii/S0022519316303228
44. Kim, S., Seo, Y. & Jung, E. Prediction of COVID-19 transmission dynamics

using a mathematical model considering behavior changes in Korea . *Epidemiol Health*. **42** pp. e2020026-0 (2020,4), https://doi.org/10.4178/epih.e2020026

45. Kim, Y., Seo, M.& Yeom, H. Estimating a breakpoint in the pattern of spread of COVID-19 in South Korea. *International Journal Of Infectious Diseases*. **97** pp. 360-364 (2020,8)
46. Köhler-Rieper, F., Röhl, C. & De Micheli, E. A novel deterministic forecast model for the Covid-19 epidemic based on a single ordinary integro-differential equation. *The European Physical Journal Plus*. **135**, 599 (2020), https://doi.org/10.1140/epjp/s13360-020-00608-0
47. Kretzschmar, M.& Wallinga, J. Mathematical Models in Infectious Disease Epidemiology. *Modern Infectious Disease Epidemiology: Concepts, Methods, Mathematical Models, And Public Health*. pp. 209-221 (2009,7), https://www.ncbi.nlm.nih.gov/pmc/articles/PMC7178885/
48. Li, W., Lin, G., Ma, C.& Yang, F. Traveling wave solutions of a nonlocal delayed SIR model without outbreak threshold. *Discrete & Continuous Dynamical Systems - B*. **19**, 467-484, http://aimsciences.org//article/id/d99e6db9-456f-4a01-add9-e0b99b823bb4
49. MARC (Mid-America Regional Council)- Kansas City Region COVID-19 Data Hub. , https://marc2.org/covidhub/
50. May, R. & Noye, J. The Numerical Solution of Ordinary Differential Equations: Initial Value Problems. *Computational Techniques For Differentail Equations*. **83** pp. 1-94 (1984), http://www.sciencedirect.com/science/article/pii/S0304020808712003

51. Nwankwo, A. & Okuonghae, D. A Mathematical Model for the Population Dynamics of Malaria with a Temperature Dependent Control. *Differential Equations And Dynamical Systems*. (2019), https://doi.org/10.1007/s12591-019-00466-y

52. Oluyori, D. Backward and Hopf bifurcation analysis of an SEIRS COVID-19 epidemic model with saturated incidence and saturated treatment response. (2020), https://www.medrxiv.org/content/10.1101/2020.08.28.20183723v1.full.pdf

53. Ourworldindata Coronavirus Data. , https://ourworldindata.org/coronavirus

54. Panovska-Griffiths, J. Can mathematical modelling solve the current Covid-19 crisis?. *BMC Public Health*. **20**, 551 (2020), https://doi.org/10.1186/s12889-020-08671-z

55. Qin, J., You, C., Lin, Q., Hu, T., Yu, S. & Zhou, X. Estimation of incubation period distribution of COVID-19 using disease onset forward time: A novel cross-sectional and forward follow-up study. *Science Advances*. **6**, eabc1202 (2020,8), http://advances.sciencemag.org/content/6/33/eabc1202.abstract

56. Ramsay, J., Hooker, G., Campbell, D. & Cao, J. Parameter estimation for differential equations: a generalized smoothing approach. *Journal Of The Royal Statistical Society: Series B (Statistical Methodology)*. **69**, 741-796 (2007,11), https://doi.org/10.1111/j.1467-9868.2007.00610.x

57. Roberts, M. & Heesterbeek, J. Mathematical models in epidemiology. *Mathematical Models*. **49** pp. 6221 (2003)

58. Roddam, A. Mathematical Epidemiology of Infectious Diseases: Model Building, Analysis and Interpretation: O Diekmann and JAP Heesterbeek, 2000, Chichester: John Wiley pp. 303, £39.95. ISBN 0-471-49241-8. *International Journal*

*Of Epidemiology*. **30**, 186 (2001,2), https://doi.org/10.1093/ije/30.1.186

59. Rothan, H. & Byrareddy, S. The epidemiology and pathogenesis of coronavirus disease (COVID-19) outbreak. *Journal Of Autoimmunity*. **109** pp. 102433 (2020), http://www.sciencedirect.com/science/article/pii/S0896841120300469
60. Shrestha, S. & Lloyd-Smith, J. Introduction to mathematical modeling of infectious diseases. (2010)
61. Siettos, C. & Russo, L. Mathematical modeling of infectious disease dynamics. *Virulence*. **4**, 295-306 (2013,5), https://doi.org/10.4161/viru.24041
62. Sirijampa, A., Chinviriyasit, S. & Chinviriyasit, W. Hopf bifurcation analysis of a delayed SEIR epidemic model with infectious force in latent and infected period. *Advances In Difference Equations*. **2018**, 348 (2018), https://doi.org/10.1186/s13662-018-1805-6
63. Tomochi, M. & Kono, M. A mathematical model for COVID-19 pandemic—SIIR model: Effects of asymptomatic individuals. *Journal Of General And Family Medicine*. **n/a** (2020,11), https://doi.org/10.1002/jgf2.382
64. Waltz, R., Morales, J., Nocedal, J. & Orban, D. An interior algorithm for nonlinear optimization that combines line search and trust region steps. *Mathematical Programming*. **107**, 391-408 (2006), https://doi.org/10.1007/s10107-004-0560-5
65. Washingtonpost Markets live updates coronavirus economy. , https://www.washingtonpost.com/business/2020/03/12/markets-live-updates-coronavirus-economy/
66. Wu, S., Mertens, A., Crider, Y., Nguyen, A., Pokpongkiat, N., Djajadi, S., Seth, A., Hsiang, M., Colford, J., Reingold, A., Arnold, B., Hub-

bard, A.& Benjamin-Chung, J. Substantial underestimation of SARS-CoV-2 infection in the United States. *Nature Communications*. **11**, 4507 (2020), https://doi.org/10.1038/s41467-020-18272-4

67. Zhang, S., Yang, Y.& Zhou, Y. Traveling waves in a delayed SIR model with nonlocal dispersal and nonlinear incidence. *Journal Of Mathematical Physics*. **59** pp. 11513 (2018,1), https://ui.adsabs.harvard.edu/abs/2018JMP....59a1513Z
68. San Francisco Department Health San Francisco COVID-19 data. , https://sf.gov/resource/2021/covid-19-data-and-reports
69. Moein, S., Nickaeen, N., Roointan, A., Borhani, N., Heidary, Z., Javanmard, S., Ghaisari, J. & Gheisari, Y. Inefficiency of SIR models in forecasting COVID-19 epidemic: a case study of Isfahan. *Scientific Reports*. **11**, 4725 (2021), https://doi.org/10.1038/s41598-021-84055-6
70. Huang, D., Tao, H., Wu, Q., Huang, S. & Xiao, Y. Modeling of the Long-Term Epidemic Dynamics of COVID-19 in the United States. *International Journal Of Environmental Research And Public Health* . **18** (2021)
71. Kassem, A. Does Temperature Affect COVID-19 Transmission? . *Frontiers In Public Health* . **8** pp. 934 (2020), https://www.frontiersin.org/article/10.3389/fpubh.2020.554964
72. Maragakis, L. Coronavirus Second Wave, Third Wave and Beyond: What Causes a COVID Surge. (Johns Hopkins,2021)
73. Saint Louis Health Department Saint Louis COVID-19 Data. , https://www.stlouis-mo.gov/covid-19/data/index.cfm
74. Jamil, T., Alam, I., Gojobori, T. & Duarte, C. No Evidence for Temperature-

Dependence of the COVID-19 Epidemic . *Frontiers In Public Health* . **8** pp. 436 (2020), https://www.frontiersin.org/article/10.3389/fpubh.2020.00436

75. Anastassopoulou, C., Russo, L., Tsakris, A. & Siettos, C. Data-based analysis, modelling and forecasting of the COVID-19 outbreak. *PloS One*. **15**, e0230405 (2020)
76. Giordano, G., Blanchini, F., Bruno, R., Colaneri, P., Di Filippo, A., Di Matteo, A. & Colaneri, M. Modelling the COVID-19 epidemic and implementation of population-wide interventions in Italy. *Nature Medicine*. **26**, 855-860 (2020)
77. Lin, Q., Zhao, S., Gao, D., Lou, Y., Yang, S., Musa, S., Wang, M., Cai, Y., Wang, W., Yang, L. & Others A conceptual model for the coronavirus disease 2019 (COVID-19) outbreak in Wuhan, China with individual reaction and governmental action. *International Journal Of Infectious Diseases*. **93** pp. 211-216 (2020)
78. Balcan, D., Colizza, V., Gonçalves, B., Hu, H., Ramasco, J. & Vespignani, A. Multiscale mobility networks and the spatial spreading of infectious diseases. *Proceedings Of The National Academy Of Sciences*. **106**, 21484-21489 (2009)
79. Belik, V., Geisel, T. & Brockmann, D. Natural human mobility patterns and spatial spread of infectious diseases. *Physical Review X*. **1**, 011001 (2011)
80. Viboud, C., Bjørnstad, O., Smith, D., Simonsen, L., Miller, M. & Grenfell, B. Synchrony, waves, and spatial hierarchies in the spread of influenza. *Science*. **312**, 447-451 (2006)
81. Gousseff, M., Penot, P., Gallay, L., Batisse, D., Benech, N., Bouiller, K., Collarino, R., Conrad, A., Slama, D., Joseph, C. & Others Clinical recurrences of

COVID-19 symptoms after recovery: viral relapse, reinfection or inflammatory rebound?. *Journal Of Infection*. **81**, 816-846 (2020)

82. Seow, J., Graham, C., Merrick, B., Acors, S., Pickering, S., Steel, K., Hemmings, O., O'Byrne, A., Kouphou, N., Galao, R. & Others Longitudinal observation and decline of neutralizing antibody responses in the three months following SARS-CoV-2 infection in humans. *Nature Microbiology*. **5**, 1598-1607 (2020)
83. AlQadi, H., Bani-Yaghoub, M., Balakumar, S., Wu, S. & Francisco, A. Assessment of Retrospective COVID-19 Spatial Clusters with Respect to Demographic Factors: Case Study of Kansas City, Missouri, United States. *International Journal Of Environmental Research And Public Health* . **18** (2021)
84. AlQadi, H., Yaghoub, M., Wu, S., Balakumar, S. & Francisco, A. Prospective Spatial–Temporal Clusters of COVID-19 in Local Communities: Case Study of Kansas City, Missouri, United States. *Epidemiology & Infection*. pp. 1-24
85. AlQadi, H. & Bani-Yaghoub, M. Incorporating global dynamics to improve the accuracy of disease models: Example of a COVID-19 SIR model. *PloS One*. **17**, e0265815 (2022)
86. Centers for Disease Control and Prevention Symptoms of COVID-19. (2021), https://www.cdc.gov/coronavirus/2019-ncov/symptoms-testing/symptoms.html
87. Centers for Disease Control and Prevention How COVID-19 Spreads. (2021), https://www.cdc.gov/coronavirus/2019-ncov/prevent-getting-sick/how-covid-spreads.html
88. Culp, W. Coronavirus Disease 2019. *A & A Practice*. **14**, e01218 (2020),

https://www.who.int/docs/default-source/coronaviruse

89. Desjardins, M., Hohl, A. & Delmelle, E. Rapid surveillance of COVID-19 in the United States using a prospective space-time scan statistic: Detecting and evaluating emerging clusters. *Applied Geography*. **118**, 102202 (2020), https://doi.org/10.1016/j.apgeog.2020.102202
90. Kansas City Health Department KCMO Coronavirus Activity Timeline.. (2021), https://www.kcmo.gov/city-hall/departments/health/coronavirus
91. Katella, K. Comparing the COVID-19 Vaccines: How Are They Different?. (2021,11), https://www.yalemedicine.org/news/covid-19-vaccine-comparison
92. Kulldorff, M. Prospective time periodic geographical disease surveillance using a scan statistic. *Journal Of The Royal Statistical Society: Series A (Statistics In Society)*. **164**, 61-72 (2001,1), https://doi.org/10.1111/1467-985X.00186
93. Kulldorff, M. A spatial scan statistic. *Communications In Statistics - Theory And Methods*. **26**, 1481-1496 (1997,1), https://doi.org/10.1080/03610929708831995
94. Kulldorff, M., Feuer, E., Miller, B. & Freedma, L. Breast Cancer Clusters in the Northeast United States: A Geographic Analysis. *American Journal Of Epidemiology*. **146**, 161-170 (1997,7), https://doi.org/10.1093/oxfordjournals.aje.a009247
95. Kulldorff, M. & Nagarwalla, N. Spatial disease clusters: Detection and inference. *Statistics In Medicine*. **14**, 799-810 (1995,4), https://doi.org/10.1002/sim.4780140809
96. Missouri's COVID-19 Dashboard, COVID-19 Vaccination in Missouri. (2021), https://covidvaccine.mo.gov/data/

97. Takahashi, K., Kulldorff, M., Tango, T. & Yih, K. A flexibly shaped space-time scan statistic for disease outbreak detection and monitoring. *International Journal Of Health Geographics*. **7**, 14 (2008), https://doi.org/10.1186/1476-072X-7-14

98. Mbunge, E., Akinnuwesi, B., Fashoto, S., Metfula, A. & Mashwama, P. A critical review of emerging technologies for tackling COVID-19 pandemic. *Human Behavior And Emerging Technologies*. **3**, 25-39 (2021,1), https://doi.org/10.1002/hbe2.237

99. Kansas City Health Department Kansas City COVID-19 Information Center. (2021), https://www.kcmo.gov/city-hall/departments/health/coronavirus

100. Kulldorff, M., Athas, W., Feurer, E., Miller, B. & Key, C. Evaluating cluster alarms: a space-time scan statistic and brain cancer in Los Alamos, New Mexico.. *American Journal Of Public Health*. **88**, 1377-1380 (1998,9), https://doi.org/10.2105/AJPH.88.9.1377

101. Hussain, S., Mubeen, M., Ahmad, A., Fahad, S., Nasim, W., Hammad, H., Shah, G., Murtaza, B., Tahir, M. & Parveen, S. Using space–time scan statistic for studying the effects of COVID-19 in Punjab, Pakistan: a guideline for policy measures in regional agriculture. *Environmental Science And Pollution Research*. pp. 1-14 (2021)

102. Hohl, A., Delmelle, E., Desjardins, M. & Lan, Y. Daily surveillance of COVID-19 using the prospective space-time scan statistic in the United States. *Spatial And Spatio-temporal Epidemiology*. **34** pp. 100354 (2020), http://www.sciencedirect.com/science/article/pii/S1877584520300320

103. Cereda, D., Tirani, M., Rovida, F., Demicheli, V., Ajelli, M., Poletti, P., Tren-

tini, F., Guzzetta, G., Marziano, V. & Barone, A. The early phase of the COVID-19 outbreak in Lombardy, Italy. *ArXiv Preprint ArXiv:2003.09320*. (2020)

104. Purwanto, P., Utaya, S., Handoyo, B., Bachri, S., Astuti, I., Utomo, K. & Aldianto, Y. Spatiotemporal analysis of COVID-19 spread with emerging hotspot analysis and space–time cube models in East Java, Indonesia. *ISPRS International Journal Of Geo-Information*. **10**, 133 (2021)
105. Ahasan, R., Alam, M., Chakraborty, T. & Hossain, M. Applications of GIS and geospatial analyses in COVID-19 research: A systematic review [version 1; peer review: 1 approved]. *F1000Research*. **9** (2020), https://f1000research.com/articles/9-1379/v1
106. Andrade, L., Gomes, D., Góes, M., Souza, M., Teixeira, D., Ribeiro, C., Alves, J., Araújo, K. & Santos, A. Surveillance of the first cases of COVID-19 in Sergipe using a prospective spatiotemporal analysis: the spatial dispersion and its public health implications. *Revista Da Sociedade Brasileira De Medicina Tropical*. **53** pp. e20200287-e20200287 (2020), https://pubmed.ncbi.nlm.nih.gov/32491098
107. Bhosale, S. & Shinde, N. Outbreak of COVID-19 in India and high risk of cluster containment: A case study. *Journal Of Applied Pharmaceutical Research*. **8**, 1-7 (2020)
108. Saran, S., Singh, P., Kumar, V. & Chauhan, P. Review of Geospatial Technology for Infectious Disease Surveillance: Use Case on COVID-19. *Journal Of The Indian Society Of Remote Sensing*. **48**, 1121-1138 (2020), https://doi.org/10.1007/s12524-020-01140-5
109. Danis, K., Epaulard, O., Bénet, T., Gaymard, A., Campoy, S., Botelho-Nevers,

E., Bouscambert-Duchamp, M., Spaccaferri, G., Ader, F., Mailles, A., Boudalaa, Z., Tolsma, V., Berra, J., Vaux, S., Forestier, E., Landelle, C., Fougere, E., Thabuis, A., Berthelot, P., Veil, R., Levy-Bruhl, D., Chidiac, C., Lina, B., Coignard, B., Saura, C. & Team, I. Cluster of Coronavirus Disease 2019 (COVID-19) in the French Alps, February 2020. *Clinical Infectious Diseases : An Official Publication Of The Infectious Diseases Society Of America*. **71**, 825-832 (2020,7), https://pubmed.ncbi.nlm.nih.gov/32277759

110. Franch-Pardo, I., Desjardins, M., Barea-Navarro, I. & Cerdà, A. A review of GIS methodologies to analyze the dynamics of COVID-19 in the second half of 2020. *Transactions In GIS*. **25**, 2191-2239 (2021,10), https://doi.org/10.1111/tgis.12792
111. Owusu, C., Desjardins, M., Baker, K. & Delmelle, E. Residential mobility impacts relative risk estimates of space-time clusters of chlamydia in Kalamazoo County, Michigan. *Geospatial Health*. **14** (2019,11), https://geospatialhealth.net/index.php/gh/article/view/812
112. Martines, M., Ferreira, R., Toppa, R., Assunção, L., Desjardins, M. & Delmelle, E. Detecting space–time clusters of COVID-19 in Brazil: mortality, inequality, socioeconomic vulnerability, and the relative risk of the disease in Brazilian municipalities. *Journal Of Geographical Systems*. **23**, 7-36 (2021)
113. Pfefferle, S., Kobbe, R., Guenther, T., Noerz, D., Santer, R., Oh, J., Kluge, S., Oestereich, L., Peldschus, K. & Indenbirken, D. Infection control and virological assessment of the first cluster of COVID-19 in northern Germany. *SSRN Electronic Journal*. (2020)

114. Ferreira, R., Martines, M., Toppa, R., Assuncao, L., Desjardins, M. & Delmelle, E. Applying a prospective space-time scan statistic to examine the evolution of COVID-19 clusters in the state of Sao Paulo, Brazil. *MedRxiv*. (2020)

115. Shim, E., Tariq, A., Choi, W., Lee, Y. & Chowell, G. Transmission potential and severity of COVID-19 in South Korea. *International Journal Of Infectious Diseases : IJID : Official Publication Of The International Society For Infectious Diseases*. **93** pp. 339-344 (2020,4), https://pubmed.ncbi.nlm.nih.gov/32198088

116. Franch-Pardo, I., Napoletano, B., Rosete-Verges, F. & Billa, L. Spatial analysis and GIS in the study of COVID-19. A review. *Science Of The Total Environment*. **739** pp. 140033 (2020), https://www.sciencedirect.com/science/article/pii/S0048969720335531

117. Araújo, M., Nunes, V., Costa, L., Souza, T., Torres, G. & Nobre, T. Health conditions of potential risk for severe Covid-19 in institutionalized elderly people. *PLOS ONE*. **16**, e0245432 (2021,1), https://doi.org/10.1371/journal.pone.0245432

118. Billings, S., Englin, E., Hall, J. & Smith, A. Adaptation of delivery of SCCP clinical pharmacist roundtable event using a virtual platform due to COVID. *JACCP Journal Of The American College Of Clinical Pharmacy*. pp. 1658-1659 (2020)

119. Burton, M., Satterwhite, L., Shi, X., Allen, A. & Castro, M. Hospital Collaboration in Response to the COVID-19 Pandemic in Kansas City Metropolitan Region. *Kansas Journal Of Medicine*. **14** pp. 108 (2021)

120. Coleman, M., Coleman, M., Mabuza, A., Kok, G., Coetzee, M. & Dur-

rheim, D. Using the SaTScan method to detect local malaria clusters for guiding malaria control programmes. *Malaria Journal*. **8**, 68 (2009), https://doi.org/10.1186/1475-2875-8-68

121. Centers for Disease Control and Prevention Introduction to COVID-19 Racial and Ethnic Health Disparities. (2020), https://www.cdc.gov/coronavirus/2019-ncov/community/health-equity/racial-ethnic-disparities/index.html
122. Centers for Disease Control and Prevention Disparities in COVID-19-Associated Hospitalizations. (2021), https://www.cdc.gov/coronavirus/2019-ncov/community/health-equity/racial-ethnic-disparities/disparities-hospitalization.html
123. Chen, J., Qiu, Y., Yang, R., Li, L., Hou, J., Lu, K. & Xu, L. The characteristics of spatial-temporal distribution and cluster of tuberculosis in Yunnan Province, China, 2005–2018. *BMC Public Health*. **19**, 1715 (2019), https://doi.org/10.1186/s12889-019-7993-5
124. Dalla, S., Bacon, B., Ayres, J., Holmstead, S. & Ahlberg Elliot, A. 3D-printed N95 equivalent for personal protective equipment shortages: the Kansas City Mask. *Journal Of 3D Printing In Medicine*. **4**, 211-217 (2020)
125. Dalla, S., Shinde, R., Ayres, J., Waller, S. & Nachtigal, J. 3D-printed snorkel mask adapter for failed N95 fit tests and personal protective equipment shortages. *Journal Of 3D Printing In Medicine*. **4**, 203-209 (2020,11), https://doi.org/10.2217/3dp-2020-0018
126. Shi, Y., Wang, G., Cai, X., Deng, J., Zheng, L., Zhu, H., Zheng, M., Yang, B. & Chen, Z. An overview of COVID-19. *Journal Of Zhejiang University-SCIENCE*

*B.* **21**, 343-360 (2020), https://doi.org/10.1631/jzus.B2000083

127. Dokken, D. & Ahmann, E. Mental Health Needs during COVID-19: Responses in Pediatric Health Care.. *Pediatric Nursing.* **46** (2020)

128. Feng, T. Spatial and Temporal Patterns of Primary Syphilis and Secondary Syphilis in Shenzhen, China. (IntechOpen,2011), https://doi.org/10.5772/22406

129. Framme, C., Gottschling, J., Buley, P., Rohwer-Mensching, K., Junker, B., Dittberner, M. & Volkmann, I. Einfluss des COVID-19-Shutdowns auf die Arbeitsleistung einer Universitäts-Augenpoliklinik. *Der Ophthalmologe.* **118**, 659-669 (2021), https://doi.org/10.1007/s00347-021-01374-9

130. Ginther, D. & Zambrana, C. Association of Mask Mandates and COVID-19 Case Rates, Hospitalizations, and Deaths in Kansas. *JAMA Network Open.* **4**, e2114514-e2114514 (2021,6), https://doi.org/10.1001/jamanetworkopen.2021.14514

131. James, E. Kansas City, Missouri, makes list of cities named possible COVID-19 hot spots. (2020), https://www.kshb.com/news/coronavirus/kansas-city-

132. Mody, A., Pfeifauf, K., Bradley, C., Fox, B., Hlatshwayo, M., Ross, W., Sanders-Thompson, V., Joynt Maddox, K., Reidhead, M., Schootman, M., Powderly, W. & Geng, E. Understanding Drivers of Coronavirus Disease 2019 (COVID-19) Racial Disparities: A Population-Level Analysis of COVID-19 Testing Among Black and White Populations. *Clinical Infectious Diseases.* (2020,12), https://doi.org/10.1093/cid/ciaa1848

133. Mueller, A., McNamara, M. & Sinclair, D. Why does COVID-19 disproportionately affect older people?. *Aging.* **12**, 9959-9981 (2020,5),

https://pubmed.ncbi.nlm.nih.gov/32470948

134. Ramprasad, A., Qureshi, F. & Jones, B. Contributions to Health Disparities Observed in the COVID19 Pandemic. *Journal Of The National Medical Association*. **112**, S13-S14 (2020), https://www.sciencedirect.com/science/article/pii/S0027968420302121

135. Sandall, S. EpiTrax User Guide. (2019), https://clphs.health.mo.gov/lphs/diseaseprevention/epitrax/pdf/user-guide.pdf.

136. Tai, D., Shah, A., Doubeni, C., Sia, I. & Wieland, M. The Disproportionate Impact of COVID-19 on Racial and Ethnic Minorities in the United States. *Clinical Infectious Diseases : An Official Publication Of The Infectious Diseases Society Of America*. **72**, 703-706 (2021), http://europepmc.org/abstract/MED/32562416

137. Talbot, T., Kumar, S. & Kulldorff, M. The Bernoulli Spatial Scan Statistic for Birth Defect Data. (2015), https://www.satscan.org/tutorials/SaTScanTutorialNYSBirthDefect.pdf.

138. U.S. Census Bureau U.S. Census Bureau, Kansas City. (2020), https://www.census.gov/quickfacts/kansascitycitymissouri

139. US Zip code Organization United States Zip code. (2020), https://www.unitedstateszipcodes.org/

140. Vasquez Reyes, M. The Disproportional Impact of COVID-19 on African Americans. *Health And Human Rights*. **22**, 299-307 (2020,12), https://pubmed.ncbi.nlm.nih.gov/33390715

141. Xia, J., Cai, S., Zhang, H., Lin, W., Fan, Y., Qiu, J., Sun, L., Chang, B., Zhang, Z. & Nie, S. Spatial, temporal, and spatiotemporal analysis of malaria in Hubei Province, China from 2004-2011. *Malaria Journal*. **14** pp. 145 (2015,4), https://pubmed.ncbi.nlm.nih.gov/25879447

142. Chakraborty, T. & Ghosh, I. Real-time forecasts and risk assessment of novel coronavirus (COVID-19) cases: A data-driven analysis. *Chaos, Solitons & Fractals*. **135** pp. 109850 (2020)

143. Bukhari, Q., Jameel, Y., Massaro, J., D'Agostino, R. & Khan, S. Periodic oscillations in daily reported infections and deaths for coronavirus disease 2019. *JAMA Network Open*. **3**, e2017521-e2017521 (2020)

144. Pavlicek, T., Rehak, P. & Kral, P. Oscillatory dynamics in infectivity and death rates of COVID-19. *Msystems*. **5**, e00700-20 (2020)

145. Li, H., Xu, X., Dai, D., Huang, Z., Ma, Z. & Guan, Y. Air pollution and temperature are associated with increased COVID-19 incidence: a time series study. *International Journal Of Infectious Diseases*. **97** pp. 278-282 (2020)

146. Zhang, M., Wang, S., Hu, T., Fu, X., Wang, X., Hu, Y., Halloran, B., Cui, Y., Liu, H., Liu, Z. & Others Human mobility and COVID-19 transmission: a systematic review and future directions. *MedRxiv*. (2021)

147. Lawrence, P. *Differential equations and dynamical systems*. (Springer-Verlag, New York,1991)

148. Berman, A. & Plemmons, R. *Nonnegative matrices in the mathematical sciences*. (Society for Industrial and Applied Mathematics, Philadelphia,1994)

149. Driessche, P. & Watmough, J. Reproduction numbers and sub-threshold endemic

equilibria for compartmental models of disease transmission. *Mathematical Biosciences*. **180**, 29-48 (2002)

150. Motta, M., Sylvester, S., Callaghan, T. & Lunz-Trujillo, K. Encouraging COVID-19 vaccine uptake through effective health communication. *Frontiers In Political Science*. **3** pp. 1 (2021)
151. Kherabi, Y., Fiolet, T., Rozencwajg, S., Salaün, J. & Peiffer-Smadja, N. COVID-19 vaccine boosters: What do we know so far?. *Anaesthesia, Critical Care & Pain Medicine*. (2021)
152. Rzymski, P., Camargo, C., Fal, A., Flisiak, R., Gwenzi, W., Kelishadi, R., Leemans, A., Nieto, J., Ozen, A., Perc, M. & Others COVID-19 Vaccine Boosters: The good, the bad, and the ugly. *Vaccines*. **9**, 1299 (2021)
153. Ekström, A., Tomson, G., Wanyenze, R., Bhutta, Z., Kyobutungi, C., Binagwaho, A. & Ottersen, O. Addressing production gaps for vaccines in African countries. *Bulletin Of The World Health Organization*. **99**, 910 (2021)
154. Liu, K., Ai, S., Song, S., Zhu, G., Tian, F., Li, H., Gao, Y., Wu, Y., Zhang, S., Shao, Z. & Others Population movement, city closure in Wuhan, and geographical expansion of the COVID-19 infection in China in January 2020. *Clinical Infectious Diseases*. **71**, 2045-2051 (2020)
155. Ballesteros, P., Salazar, E., Sánchez, D. & Bolaños, C. Spatial and spatiotemporal clustering of the COVID-19 pandemic in Ecuador. *Revista De La Facultad De Medicina*. **69** (2021)
156. Ullah, S., Nor, N., Daud, H., Zainuddin, N., Gandapur, M., Ali, I. & Khalil, A. Spatial cluster analysis of COVID-19 in Malaysia (Mar-Sep, 2020). *Geospatial*

*Health*. **16** (2021)

157. Petrovskii, S., Morozov, A. & Venturino, E. Allee effect makes possible patchy invasion in a predator-prey system. *Ecology Letters*. **5**, 345-352 (2002).

158. Guckenheimer, J. & Holmes, P. Nonlinear oscillations, dynamical systems and bifurcations of vector fields. *J. Appl. Mech*. **51**, 947 (1984).

159. Poincaré, H. Mémoire sur les courbes définies par une équation différentielle (I). *Journal De Mathématiques Pures Et Appliquées*. **7** pp. 375-422 (1881)

160. Hsieh, Y., Driessche, P. & Wang, L. Impact of travel between patches for spatial spread of disease. *Bulletin Of Mathematical Biology*. **69**, 1355-1375 (2007)

161. Organization, W. & Others Update on omicron. *World Health Organization. Https://www. Who. Int/news/item/28-11-2021-update-on-omicron*. (2021)

# VITA

Hadeel AlQadi was born in Jeddah, Saudi Arabia. She received her B.S. degree in Statistics and Computer Science from King Abdulaziz University, Saudi Arabia, in 2009. She obtained her M.S. degree in Statistics from the University of Missouri- Kansas City (UMKC), USA, in 2014. She has been a lecturer in the Department of Mathematics and Statistics at Jazan University in Saudi Arabia since 2014. She taught the Mathematical Statistics and the Applied Statistics courses before receiving a Jazan University scholarship to complete her studies. During her Ph.D., Ms. AlQadi worked for two years as a Graduate Teaching Assistant (GTA) and taught the Precalculus Algebra Fundamentals course, the Precalculus Algebra course, and the Elementary Statistics course.

Her main research interest is in the statistical and mathematical modeling of infectious diseases. She has three publications which were published in the *International Journal of Environmental Research and Public Health* in 2021, in the *Epidemiology and Infection Journal*, and in the *PLOS One Journal* in 2022. She has also given presentations about her research. She presented two presentations at the 7th Annual UMKC Mathematics and Statistics Research Day, and she has given a presentation at the annual UMKC Interdisciplinary Symposium, in 2021. Also, she presented a poster at the Southern Regional Council on Statistics (SRCOS) in Jekyll Island, Georgia, in 2021.

Moreover, Hadeel received several awards, including the Graduate Assistance

Fund with Merit Award (GAF) for 2022 and 2021, the SRCOS Travel Award for 2021, and the Grace Hopper Celebration Student Scholarship in 2020.

In terms of professional development, in 2021, Hadeel AlQadi received a professional certificate from the Preparing Future Faculty program, a graduate certificate in college teaching and career preparation that prepares a graduate student to become an excellent professor at diverse higher education institutions.